

Development of a Prototype Photoacoustic Microscope and Spectroscope and Advanced Semiconductor Material Characterization

By

Lu Xu *B.Sc*

Dublin City University



School of Electronic Engineering

Research Supervisor

Prof. Patrick J. McNally

Thesis submitted for the degree of Doctor of Philosophy

2012

I hereby certify that this material, which I now submit for assessment on the programme of study leading to the award ofPhD..... (insert title of degree for which registered) is entirely my own work, and that I have exercised reasonable care to ensure that the work is original, and does not to the best of my knowledge breach any law of copyright, and has not been taken from the work of others save and to the extent that such work has been cited and acknowledged within the text of my work.

Signed:  ¹⁹⁻⁰⁷⁻²⁰¹² (Candidate) ID No.: 53130120 Date: 19-07-2012

ACKNOWLEDGEMENTS

It was not about the outcome of obtaining a PhD, but instead it was about the process of getting there.

My thanks are due first to my supervisor, Prof Patrick J McNally, of the School of Electronic Engineering, Dublin City University, for his guidance, support, encouragement and endless patience.

Thanks to my wife, QingMei Wang, for all the inspiration motivation and support through the years. The university campus was the place where we met for the first time. The beginning of my PhD research was also the time when we started to go through many life changing events hand by hand.

Thanks to Dr. Donnacha Lowney. As the post-doctoral researcher, his day-to-day guidance and support at the early stage of research project was very critical.

ABSTRACT

The thesis can be divided into two parts.

In the first part of my thesis, I present the design, construction and test results of a prototype gas-cell Photoacoustic (PA) Spectrometer and Microscope. It is a low cost, non-contact technique, which can be used to characterize semiconductor band-gap structures and subsurface defects. It requires no liquid coupling and no sample surface preparation in advance

The instrument development includes the optical system design, mechanical design of the PA cell using AutoCAD®, pre-amplifier circuit design, system noise analysis, hardware control, data acquisition system and graphical user interface (GUI) development using LabView®. A multiple-microphone detection scheme, helium gas coupling, acoustic resonance and a high power laser light source are used to enhance the PA signal and to increase the data acquisition speed. The PA system is calibrated to remove the acoustic resonance effect and the background fingerprint of light source intensity spectrum. The linear relationship between the PA signal and the source intensity is verified. The impacts of the lock-in amplifier performance, the focus offset and the coupling gas within the cell on the PA signal are discussed.

Various samples are used to verify performance of the developed PA system. These include Silicon wafers, GaAs wafers, multi-layered structures on silicon substrates, carbon-black powder, laser-machined air trenches, bonded silicon wafers and a packaged IC chip. For spectroscopy applications, the PA spectra of two types of GaAs wafers are characterized successfully. For microscopy applications, the PA system is proven to have a vertical resolution of ~ 20 nm and a lateral resolution of \sim sub-100 μm . Its probe depth could be as deep as 450

μm below the silicon surface. The data acquisition speed of the PA system is improved for industrial applications. Two high-resolution (10,000 pixels) thermal images (one in phase and another in amplitude) of semiconductor devices can be obtained in less than 50 seconds across an area of approx. 9 mm x 9 mm.

In the second part of my thesis, other related non-destructive characterization work on advanced semiconductor materials is presented. In chapter six, Synchrotron X-ray Topography (SXRT) and Micro-Raman Spectroscopy (uRS) are used to study two sets of the femto-second and nano-second laser machined grooves on InP substrates. In chapter seven, other characterization work is presented to study the H₂ preconditioning effect on self-assembled Ge-islands on Silicon. Both cases demonstrate the commercialised metrology tools' capabilities to analyse the distribution profile of the strain and the chemical composition on the top surface.

The PA system prototype presented in this thesis can be used as a complementary tool. It provides ultra-deep probe depth for the subsurface defects, when compared to the SXRT and the uRS methods.

TABLE OF CONTENTS

LIST OF SYMBOLS	3
LIST OF ABBREVIATIONS	5
1 INTRODUCTION	6
1.1 OBJECTIVES OF THE PROJECT.....	6
1.2 BACKGROUND OF THE PHOTOACOUSTIC TECHNIQUES	7
1.3 OVERVIEW OF THE THESIS	19
2 THE PHOTOACOUSTIC THEORY	22
2.1 ROSENCWAIG-GERSHO THEORY	22
2.2 SIMPLIFIED ROSENCWAIG-GERSHO THEORY: SPECIAL CASES	36
2.3 PHOTOACOUSTIC THEORY FOR SEMICONDUCTOR MATERIALS	40
3. PHOTOACOUSTIC SYSTEM DESIGN AND NOISE ANALYSIS	42
3.1 INTRODUCTION	42
3.2 PHOTOACOUSTIC SPECTROMETER (PAS) AND MICROSCOPY (PAM)	
SPECIFICATIONS	44
3.3 OVERVIEW OF THE PHOTOACOUSTIC SPECTROMETER AND	
MICROSCOPE.....	47
3.4 HARDWARE DESCRIPTION.....	51
4. PHOTOACOUSTIC SYSTEM CALIBRATION AND	85
VERIFICATION.....	85
4.1. LIGHT SOURCE INTENSITY LINEARITY CALIBRATION	85
4.2. SR850 LOCK-IN AMPLIFIER CALIBRATION.....	91
4.3. ARC LAMP LIGHT SOURCE SPECTRUM CALIBRATION	95
4.4. IMPACT OF FOCUS OFFSET BETWEEN THE PA SAMPLE POSITION AND	
THE FOCAL POINT	97
4.5. IMPACT OF THE COUPLING GAS WITHIN THE CELL: AIR VS. HELIUM	
GAS 100	
4.6. IMPACT OF THE ACOUSTIC RESONANCE OF THE PA CELL	106
5. APPLICATIONS OF THE PA SYSTEM	114
5.1. PA SIGNAL MODELING OF MULTI-LAYERED SEMICONDUCTOR	
STRUCTURES.....	114

5.2.	APPLICATION 1: PA IMAGING OF SUBSURFACE AIR TRENCHES IN SILICON.....	123
5.3.	APPLICATION 2: PA IMAGING OF WAFER BONDING DEFECTS	130
5.4.	APPLICATION 3: PHOTOACOUSTIC IMAGING ON PACKAGED IC	143
5.5.	APPLICATION 4: PHOTOACOUSTIC SPECTROSCOPY FOR BANDGAP DEFECT CHARACTERIZATION IN SEMICONDUCTOR MATERIALS.....	151
6	SYNCHROTRON X-RAY TOPOGRAPHY AND MICRO RAMAN STUDY ON LASER MICRO- MACHINING	156
6.1	INTRODUCTION	156
6.2	EXPERIMENTAL DETAILS	159
6.3	RESULTS AND DISCUSSION.....	161
6.4	CONCLUSION	177
7	RAMAN STUDY OF THE STRAIN AND H₂ PRECONDITIONING EFFECT ON SELF-ASSEMBLED GE ISLANDS ON SI SUBSTRATES	179
8	CONCLUSION	190
9	REFERENCES.....	192
	APPENDIX A: SAMPLE MATLAB® CODE TO SIMULATE PA SIGNAL FREQUENCY RESPONSE.....	201
	APPENDIX B: RELATED PUBLICATIONS	204
	APPENDIX C: COPYRIGHT PERMISSIONS	208

LIST OF SYMBOLS

a	Thermal diffusion coefficient
b	Thermal mismatch between sample and backing material, $= \frac{k_b \delta_b}{k_s \delta_s}$
C	Specific Heat
c	Speed of light
D	Diffusion constant of the photo-excited carriers
E_g	Bandgap energy
f	Modulation frequency
g	Thermal mismatch between the coupling gas and sample, $= \frac{k_g \delta_g}{k_s \delta_s}$
G	Density of photo-excited carriers generated by light absorption
H	Heat density
h	Planck constant
I	Light intensity
I_0	Light source intensity
k	Thermal conductivity
l	Length
L	Length of Photoacoustic cell
n	Density of the photo-excited carriers
P	Pressure
P_0	Ambient pressure
Q	Complex envelope of the sinusoidal pressure variation
r	$= \frac{\beta}{\delta_s}$
T	Temperature
T_0	Ambient temperature
u	Surface recombination velocity of free carriers
V	Volume
W	Time dependent component of the temperature relative to the ambient temperature at the interface between the

	sample and backing material
W_0	Time independent component of the temperature relative to the ambient temperature at the sample-backing interface
α	Thermal diffusivity
β	Optical absorption coefficient
β_T	Thermal cubic expansion coefficient of the adiabatic gas
γ	Ratio of the molar specific heats at the constant pressure
δ	Dirac delta function
η	Heat conversion efficiency by non-radiative recombination process
η_B	Percentage of the energy produced in the bulk by non-radiative processes
η_s	Percentage of the energy produced at the surface by non-radiative processes
λ	Wavelength
μ	Thermal diffusion length
μ_β	Optical absorption length
μ_b	Thermal diffusion length in the backing material
μ_s	Thermal diffusion length in the sample material
μ_g	Thermal diffusion length in the gas
θ	Time dependent component of the sample temperature on the top surface relative to the ambient temperature
θ_0	Time independent component of the sample temperature on the top surface relative to the ambient temperature
ρ	Density
σ	Adapted thermal diffusion coefficient (complex number)
τ	Recombination time constant of the photo-excited carriers
τ_{BB}	Surface recombination time constant
τ_{IB}	Inter-band transition time constant
ω	Angular modulation frequency

LIST OF ABBREVIATIONS

<i>Abbreviations</i>	<i>Descriptions</i>
AFM	Atomic Force Microscope
CCD	Charge-Coupled Device
CMP	Chemical Mechanical Polishing
DoF	Depth of Focus
FIB	Focused Ion Beam
IC	Integrated Circuit
ITRS	International Technology Roadmap for Semiconductors
MEMS	Micro-Electro-Mechanical Systems
OM	Optical Metrology
PA	Photoacoustic
PAM	Photoacoustic Microscope
PAS	Photoacoustic Spectroscopy
RC Delay	Resistive-Capacitive Delay
SEM	Scanning Electron Microscope
SXRT	Synchrotron X-Ray Topography
TEM	Transmission Electron Microscope
μ RS	Micro Raman Spectroscopy

Chapter 1

INTRODUCTION

1

Introduction

In this chapter, the rationale of the project is discussed. The fundamental aim of this research is outlined. An introduction to gas cell photoacoustic techniques and a brief summary of previous research is included.

1.1

Objectives of the project

Photoacoustic (PA) Spectroscopy and Microscopy for the semiconductor industry are essentially at the same level of development as micro-Raman spectroscopy ca. 20 years ago. The PA equipment is at research tool level and has not evolved into a system for routine analysis. No robust, commercial metrology product, which is coupled with automatic data acquisition, graphical user interface and data analysis tooling, is available on the market.

The aim of this research is to develop a novel, automatic photoacoustic system based on the gas-microphone concept and to characterize a selection of advanced semiconductor materials and devices. In addition, some selected semiconductor materials are analysed using complementary techniques, which is discussed later in Chapter 1.2.3.

The PA data is compared with the results from Raman Spectroscopy (uRS) and Synchrotron X-ray topography (SXRT). The work demonstrates the unique characterization capability of photoacoustic methods for subsurface-structure imaging, elucidation of thermoelastic properties (elasticity, specific heat, thermal

diffusivity), thin-film thickness metrology and the non-destructive identification of bandgap defects in semiconductors.

1.2

Background of the photoacoustic techniques

The photoacoustic (PA) effect in condensed matter was first discovered in the 1880s by Alexander Graham Bell [1.1, pp.7-14]. The scientific investigation of this phenomenon was largely ignored until the 1970s, when the necessary processing electronics, especially lock-in amplifiers, became readily available. Then it became possible to overcome the major technical bottleneck associated with the photoacoustic signal, i.e. the poor signal to noise ratio (SNR). [1.2]

Semiconductor metrology using the photoacoustic effect is implemented generically as follows: When a beam of light hits the sample surface, a fraction of its optical energy is absorbed and converted into heat rapidly. It is an intrinsically non-contact process and produces a very precisely defined region of modulated heating. The subsurface structures inside optically opaque materials, i.e. semiconductor materials or devices, can be characterized non-destructively through the thermal wave diffusion process. The spectroscopic information for semiconductors can be obtained, while monitoring that material's selective absorption properties.

Currently, there are various PA semiconductor metrology products available on the university research market. Depending on their detection schemes, they have different components, i.e. excitation light sources, modulators, detectors, signal processing modules and display units. In the next section, I present a brief overview of these metrology products.

1.2.1

Current status of semiconductor metrology products using the PA effect

In a PA system, there are two possible classes of excitation/probe light sources. One is an incoherent source for spectroscopy applications in order to provide a broad spectral range, e.g. a Xenon lamp with a spectral range from 0.2 to 2.0 μm and a typical power density of $0.2 \text{ W}\cdot\text{mm}^{-2}$. The other option is to use coherent lasers for thermal-wave imaging applications in order to give a well-defined localized region of heating. Examples of such lasers include Helium-Neon (gas) (633 nm, 0.1-50 mW), Argon ion (gas) (488 nm or 514 nm, 5 mW - 20W), Gallium Arsenide semiconductor diode (780-990 nm, 1 mW - 1 cW), and etc.

To impose a temporal variation on the optical energy, the excitation light source needs to be periodically modulated. This can be done using various methods, depending on the requirement of the modulation frequency range, the modulation depth and the output power. Typical modulation methods include mechanical chopping (1 Hz to 20 Hz), direct electrical modulation (up to MHz with a semiconductor laser diode), acousto-optic modulation (AOM), and electro-optic/beam deflection method (e.g. rotating a multi-face mirror and using a vibrating mirror). [1.3]

When a fraction of the optical energy is absorbed and converted into heat, three possible schemes can be used to detect the consequent temperature increase on the sample surface: The PA effect can be measured acoustically, optically or thermally.

The acoustic detection scheme employs either a condenser microphone to detect the pressure variation in a small airtight chamber (called a photoacoustic cell), or a piezoelectric transducer to detect the thermal elastic waves in a solid medium. [1.3] For the microphone detection method, the PA signal intensity is inversely

proportional to the air volume of the cell. It is often suggested in the literature that it is important to minimize the cell volume as much as possible [1.4]. Therefore, to date, virtually all of the PA characterization using the gas-microphone method is performed on small samples, whose diameter is only ~ 10 mm. For large samples, such as 300 mm silicon wafers used in CMOS manufacturing processes, a piezoelectric transducer is normally used instead. [1.3, 1.5] This methodology is completely incompatible with industrial requirements, where non-invasive, non-destructive characterization techniques are desired. The reasons for this are twofold. Firstly, bonding the transducer to the sample is inherently invasive and potentially destructive. Secondly, user needs to separate the transducer response from the signal when interpreting the PA data. Given the fact that each piezoelectric transducer has its own unique response depending on the bonding conditions, it is very difficult to ensure the matching performance from tool to tool.

The optical sensing method uses the probe beam and photo-detector to measure the optical property variation on the sample surface or within the fluid medium adjacent to it. It is possible to detect the PA effect by monitoring the modulated thermal expansion using the probe beam displacement method (e.g. laser interferometer) or the cantilever probe approach (e.g. atomic force microscopy). Several pioneer experimental instruments are developed. [1.3] The first optical sensing method is called optical beam deflection (OBD). It is designed to monitor a deflected laser beam propagating through a gas medium. The refractive index of the gas medium varies periodically, while it is heated by the sample surface in contact. This method has been successfully used for photoacoustic gas sensors and can be applied to solid semiconductor samples with smooth and planarized surfaces. Therefore, curved surfaces, e.g. the wafer edges, will restrict the detectability and the sensitivity of this technique. The second technique is called modulated optical reflectance (MOR). It is used to monitor the reflectivity

of the sample surface, which changes while being heated by a modulated pump light source. This method needs very accurate alignment between the probe beams and the pump beams. It cannot be applied to a sample with an unpolished surface, as the reflected light intensity will decrease significantly due to the scattering effect. The third technique is called photothermal displacement (PTD) and uses interferometric methods to detect the sample volume expansion, which is synchronized with the modulated heating induced by the PA effect. The main parameters limiting its sensitivity are the intensity of the probe lasers, pointing noise and environmental vibration noise. Currently, the sensitivity for the displacement measurement can be as high as 4×10^{-4} nm Hz^{1/2} using interferometric scheme. However, similar to the MOR method, a thin layer of metal, which has a polished surface, needs to be deposited in order to prepare the samples for the PA characterization. The fourth technique is called the photothermal radiometry (PTR). It is based on the infrared detection of the temperature perturbation. This technique is non-contacting and compatible with many industry requirements. To increase the SNR, the infrared detection must be maximized and the direct incidence of the excitation radiation into the detector needs to be minimized. This method cannot be applied to certain samples with reflective top surface, such as copper interconnection layers on a silicon substrate. In such cases, most of the source radiation is reflected or scattered towards the detector, which increases the background noise. In addition, thin metal films block the infrared emission from the sub-layers and reduce the detectable signal simultaneously.

Finally, thermal detection methods can be used for PA characterization, but they involve the attachment of thermocouples, thermistors and pyroelectric transducers to the samples in order to measure the temperature variation directly. These thermal detection methods are intrinsically invasive, and thus are not as popular as the optical methods mentioned above. [1.3]

Compared to the photothermal detection schemes listed above, PA characterization using the gas-microphone concept is inherently non-contact and non-invasive. It does not require bonding of transducers directly to the sample itself. It does not need liquid coupling media or top surface reconditioning before the PA measurements. The microphone detection system is of relatively lower cost and does not need any complex optical alignment. Unlike photothermal radiometry (PTR), the background noise induced by direct light scattering can be completely eliminated, by passing the acoustic signal through a long acoustic tube. The small volume of condenser microphones also makes it possible to integrate tens of them into one PA system. This can easily improve the SNR performance by averaging the signals from these multiple sensors. This is especially important when high data acquisition speed is needed for industrial applications.

1.2.2

Potential PA applications for semiconductor industry

Non-destructive characterization of subsurface defects inside semiconductor materials and devices is of increasing importance for the microelectronics industry. Such defects are usually encountered in the four technically advanced applications outlined below.

1.2.2.1

Wafer level packaging and 3D interconnections

Fast, lower power IC devices can now be fabricated with multiple functionalities. A high level of device integration (e.g. IC-MEMS) can be fabricated by stacking modules or wafers on the top of each other. Stacking IC devices has been justified by many potential benefits, such as size reduction, increase in “silicon efficiency”, reduction of signal time delay, reduced parasitic effects, decrease of power consumption, increase in IC speed, increase in number of neighbouring devices and extension of the operational frequency bandwidth [1.5]. Such 3-

dimensional (3D) circuits require process steps, such as wafer/die bonding and thinning. Both power and signal are delivered through the silicon VIAs at the bonding interface, as shown in Figure 1.1 [1.7].

Since any un-bonded regions can cause catastrophic failure and yield losses, critical information needs to be obtained. An inspection is required to detect un-bonded bumps in flip-chip packages, to find the missing interconnections and to visualize the presence of delaminating layers. It is worth noting that the bonding interface is typically buried somewhere from a few to several hundred microns beneath the wafer surface, depending on the post-processing condition. The lack of fast semiconductor metrology tools, which have this ultra-deep probing capability, is becoming the major technical barrier. [1.8] This quality control difficulty can delay the complete acceptance of 3D wafer packaging by the industry.

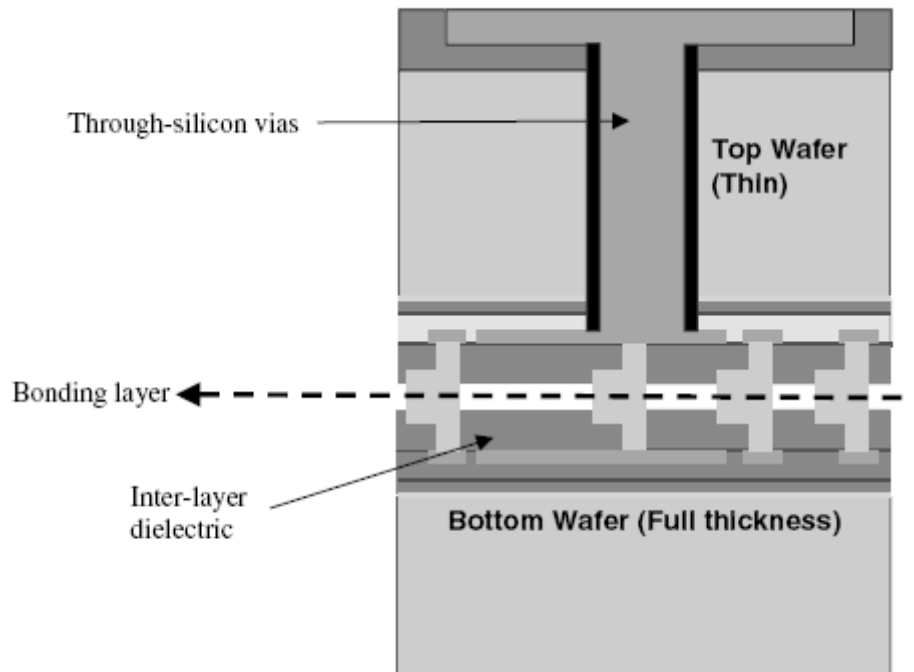


Figure 1.1: Schematic of a 3D integrated circuit. Two silicon wafers are bonded with high density of interconnections in between. The characterization of the bonding layer uniformity is critical to ensure the electrical connections between those two devices. [1.7]

1.2.2.2

Advanced inter-metal low- k dielectric materials

The most recent International Technology Roadmap for Semiconductors (ITRS) indicates that with the advancement of “multi-gate MOSFETs to below 10 nm gate length” and “memory chips approaching high densities of 512 Gb – 4 TB”, the integration of multi-billions of transistors per integrated circuit is required. [1.8] The interconnect system of this one billion transistor chip are required to deliver high frequency signals and power to various circuits. The parasitic effect becomes evident and cannot be ignored. Small parasitic capacitance (C) is

required to reduce crosstalk, power consumption, and RC delays. Therefore, interconnects with advanced low dielectric constant (k) materials are required.

However, these materials are known to have low elastic modulus, low fracture toughness and poor adhesion to the capping layers, because of their higher porosities. [1.9] Subsurface damage such as cohesive fracture, interface debonding and cracks inside low-k layers can easily occur during integration processes, such as chemical mechanical polishing (CMP) and packaging. The development of metrology equipments for sub-surface defects can insure the mechanical reliability of this advanced interconnection system and improve the yield for IC manufacturing industry.

1.2.2.3

Wafer edge inspection for 300 mm silicon wafer manufacturing

While developing advanced processes for 300 mm silicon wafers, edge defects become one of the main manufacturing issues. Some manufacturers even estimate that 30% or more of the killer defects originate from the wafer edges. [1.10] Typical defects include edge film delamination and vertical cracks. They normally occur after certain processes such as thermal cycling. The issue becomes more and more severe, especially when the thin films are deposited over the contaminations that are already present, e.g. CMP residuals or scratches left by wafer handlers at the edge surface.

Currently, the dominant approach for wafer edge inspection is based on high-resolution CCD imaging. It has the limitation of a small field of view, introduced by small depths of focus (DoF) of the CCD cameras. It is not applicable to curved surfaces. Other optical metrologies (OM), such as laser scanning scatterometry, reflectometry and ellipsometry, are only sensitive to defects within

the optical penetration depth. They have difficulty in characterizing cracks extending deep under the surface.

Scanning electron microscopy (SEM) and atomic force microscopy (AFM) are also limited for surface morphology visualization. To obtain microstructure information at depths of tens of microns below the surface the samples have to be destructively cleaved or prepared by special techniques e.g. focused ion beam (FIB). This can then allow the access to the cross-sectional facet using transmission electron microscopy (TEM). The destructive nature of TEM cannot be accepted for the industrial applications requiring in-line wafer inspection.

Micro Raman spectroscopy (μ RS) is very sensitive to the strain contrast within the semiconductor material, which can be related to the embedded defects. However, its probe depth is confined to the optical penetration depth of the excitation laser, e.g. ~ 400 nm in silicon when using an Ar^+ laser (488 nm). No Raman signal can be detected when there is a metallization layer on the top surface.

White beam synchrotron x-ray topography (SXRT) is one a useful technique to obtain transmission images of stacked wafers and devices. It can provide a comprehensive map of the strain distribution on different crystal planes simultaneously. By using a high-resolution film as a detector, its sensitivity to the strain magnitude is estimated to be at least in the order of 6×10^{-5} . A set of SXRT images with the spatial resolution of $\sim 5 \mu\text{m}$ can be easily captured in minutes. [1.11] However, the SXRT experiment requires a very expensive synchrotron radiation source. The X-ray beam needs to meet the strict requirements for intensity, divergence, continuous spectrum, polarization and time structure, which cannot be achieved without the synchrotron station, e.g. HASYLAB in Hamburg

Germany. Therefore, the SXRT method can only lie in the domain of laboratory research and cannot be easily commercialized.

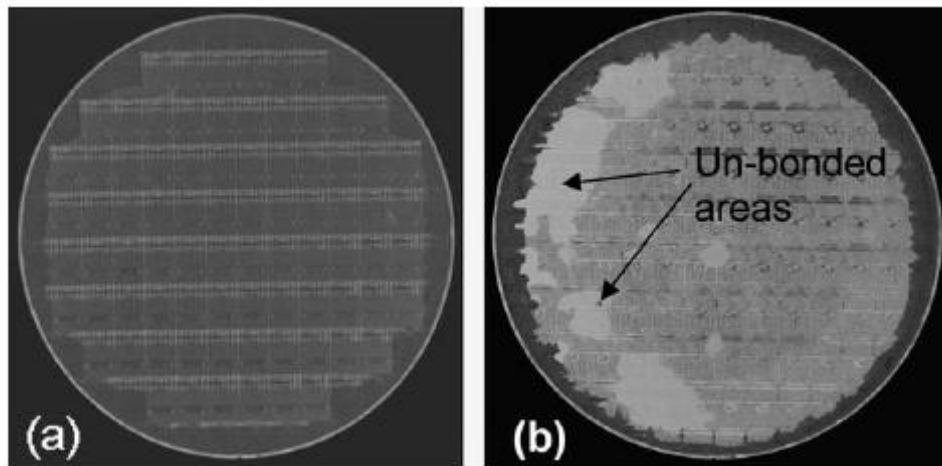


Figure 1.2: (a) The CSAM result for successfully bonded wafers. Uniform contrast indicates good bonding quality. The contrast is due to the circuit pattern in each die. (b) The CSAM result for a partially de-bonded wafer, which is processed under non-optimal conditions. The bright region corresponds to defects at the bonding interface. [1.7]

Currently, C-mode scanning acoustic microscopy (CSAM) is the principal successful commercial solution for the subsurface defect imaging. It can be used to image voids, whose size is in the order of 20–30 μm . As shown in Figure 1.2, a delaminated region, located 700 μm below the surface in silicon, can be clearly visualized [1.7]. CSAM typically uses the acoustic wave in the frequency range between 100 MHz to 200 MHz. However, at such high frequencies, the acoustic wave is heavily attenuated in air. Water is usually used as a convenient coupling medium between the sample and the receiver. Therefore, during the measurements, the semiconductor wafers have to be immersed in water. Therefore, the CSAM method cannot be applied to moisture-sensitive IC devices. It is also impossible to improve its resolution further by simply increasing the

ultrasound wave frequency. There is an effective upper frequency limit, when the acoustic wave is attenuated too much to form an output image successfully. [1.12]

The PA system described in this thesis provides an alternative metrology solution. The use of harmonic heat flow (named as thermal wave) is a good means of probing for subsurface microstructures. The thermal wave probe/diffusion length varies typically from tens of micron to several millimetres, depending on the thermal property of the material and the modulation frequency. The harmonic heat flow has wave-like features, including reflection, refraction, interference and scattering. It is possible to detect subsurface structures and thermal properties by measuring the consequent temperature variation on the surface.

1.2.2.4

Semiconductor bandgap defect characterization associated with non-radiative recombination channels

When light is incident onto a semiconductor thin film or bulk material, free carriers are excited optically. These carriers then recombine via radiative or non-radiative pathways. They decay to the ground state by dissipating the excess energy. The radiative recombination can be detected very efficiently by optical method, which is the well-known photoluminescence (PL) technique. On the other hand, there is no commercial semiconductor metrology equipment to monitor the non-radiative process, which only generates heat rather than emitting light during the recombination.

The PA system is a non-invasive photo-calorimetric solution for this application. It is a complementary spectroscopy technique, which is only sensitive to the non-radiative thermal de-excitation channels. A PA response will only be created when light is absorbed and converted into heat. Thus, elastically scattered light or

the transmitted optical energy does not influence this highly sensitive technique. By using different modulation frequencies, PA spectroscopy can be used to measure the non-radiative absorption spectrum, the lifetime of photo-excited species and the energies of electronic defects within the bandgap of semiconductor materials. [1.3]

1.2.3

Complementary semiconductor characterization techniques

1.2.3.1

Synchrotron X-ray Topography (SXRT)

Synchrotron x-ray topography is an X-ray imaging technique based on Bragg diffraction. The output images record a two-dimensional intensity profile of a beam of X-rays diffracted by a crystal. The result reflects the distribution of scattering power inside the crystal and therefore reveals the irregularities in a non-ideal crystal lattice. It can be used for monitoring crystal quality and visualizing the subsurface defects in many different crystalline materials. In many cases, topography can be applied without preparing or otherwise damaging the sample. It is therefore one variant of a non-destructive semiconductor metrology.

While imaging the subsurface structures and associated strain fields, two main contrast mechanisms can occur. One is called “extinction contrast”, which is caused by the difference in reflecting power between perfect and imperfect crystal regions. The second one is called “orientation contrast”, wherein one observes a non-uniform diffracted image of the distorted crystal, when the lattice disorientation exceeds the divergence of the synchrotron beam. [1.6] The probe depth of this technique is determined by x-ray penetration depth, which itself can be adjusted by selecting different diffraction images on the recording film. Thus a 3D knowledge of the distribution of subsurface structures in the sample from top to bottom can be built up.

1.2.3.2

Micro-Raman Spectroscopy

Raman spectroscopy is a spectroscopic technique used to study vibrational, rotational, and other low-frequency modes in a system. [1.13] It relies on inelastic scattering, or Raman scattering, of monochromatic light, usually from a laser in the visible, near infrared, or near ultraviolet range. The laser light interacts with molecular vibrations, phonons or other excitations in the material under test, resulting in the energy of incident laser photons being shifted up or down. The shift in energy gives information about the phonon modes in the system, which themselves are very sensitive to the strain status. Raman spectroscopy can also be used to characterize the subsurface defects non-destructively. It is worth noting here that, in semiconductor materials, rotational modes are not probed by Raman spectroscopy, as atoms are not free to rotate in solids.

1.3

Overview of the thesis

The thesis can be divided into two parts. In the first part of my thesis, I present the design, construction and test results of a prototype gas-cell Photoacoustic (PA) Spectrometer and Microscope. It is a low cost, non-contact technique, which can be used to characterize semiconductor band-gap structures and subsurface defects. It requires no liquid coupling and no sample surface preparation in advance

The instrument development includes the optical system design, mechanical design of the PA cell using AutoCAD®, pre-amplifier circuit design, system noise analysis, hardware control, data acquisition system and graphical user interface (GUI) development using LabView®. A multiple-microphones detection scheme, helium gas coupling, acoustic resonance and a high power laser light source are used to enhance the PA signal and to increase the data acquisition speed. The PA

system is calibrated to remove the acoustic resonance effect and the background fingerprint of light source intensity spectrum. The linear relationship between the PA signal and the source intensity is verified. The impacts of the lock-in amplifier performance, the focus offset and the coupling gas within the cell on the PA signal are discussed.

Various samples are used to verify performance of the developed PA system. These include Silicon wafers, GaAs wafers, multi-layered structures on silicon substrates, carbon-black powder, laser-machined air trenches, bonded silicon wafers and a packaged IC chip. For spectroscopy applications, the PA spectra of two types of GaAs wafers are characterized successfully. For microscopy applications, the PA system is proven to have a vertical resolution of ~ 20 nm and a lateral resolution of \sim sub-100 μm . Its probe depth could be as deep as 450 μm below the silicon surface. The data acquisition speed of the PA system is improved for industrial applications. Two high-resolution (10,000 pixels) thermal images (one in phase and another in amplitude) of semiconductor devices can be obtained in less than 50 seconds across an area of approx. 9 mm x 9 mm.

In the second part of my thesis, other related non-destructive characterization work on advanced semiconductor materials is presented. In chapter six, Synchrotron X-ray Topography (SXRT) and Micro-Raman Spectroscopy (μRS) are used to study two sets of the femto-second and nano-second laser machined grooves on InP substrates. In chapter seven, another characterization work is presented to study the H_2 preconditioning effect on self-assembled Ge-islands on Silicon. Both cases demonstrate the commercialised metrology tools' capability, to analyse the distribution profile of the strain and the chemical composition on the top surface.

The PA system prototype presented in this thesis can be used as a complementary tool. It provides ultra-deep probe depth for the subsurface defects, when comparing to the SXRT and the uRS methods.

The contents included in Chapter 6 and 7 were published in 2 journals during my PhD research period. The copyright permission has been granted by the publisher and attached in the appendix section of this thesis.

THE PHOTOACOUSTIC THEORY

2

The Photoacoustic Theory

2.1

Rosencwaig-Gersho Theory

Rosencwaig-Gersho theory (R-G Theory) is a relatively simple one-dimensional analysis, developed in the 1970s. [1.1] It was originally used to study the production of photoacoustic signals in a cylindrical photoacoustic cell. The authors obtained a series of analytical expressions of the PA signal by first modeling the heat flow within a 3-component system, including sample, gas and backing material, which was heated by the excitation light source. After applying the appropriate boundary conditions for the thermal diffusion equations, the temperature distribution inside the gas column, which was in contact with the sample, can be calculated. This air column acted as an “acoustic piston”. It underwent compression and expansion due to convective heating from the periodically irradiated sample surface. The acoustic piston induced the acoustic pressure variation within the cell, which can be detected by microphones. R-G theory is the first major mathematical model for the PA effect. The acoustic signal is dependent on the properties of the sample, gas and backing materials, including the thermal diffusion coefficient, specific heat, material density and etc. The R-G theory is now reformulated in detail in this chapter below, since many of the design criteria for the presented PA system are implicitly defined by this theory.

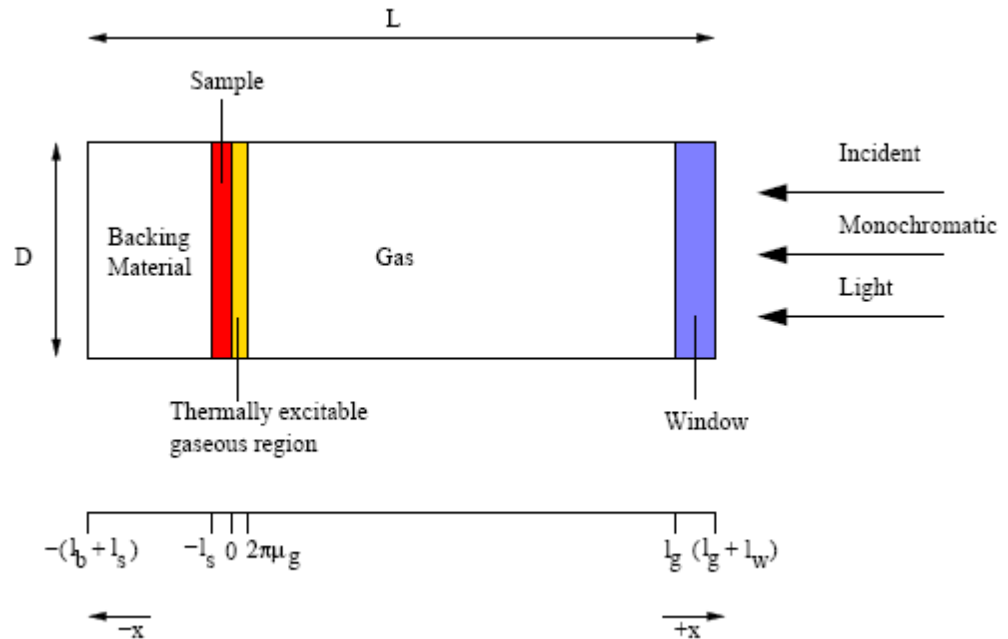


Figure 2.1: Schematic of one-dimensional photoacoustic cell, where the parameter for a given material is identified by the subscript. The label of s, g or b represents the sample, gas or backing material, respectively. The thickness of the thermally excitable region can be estimated as $2\pi\mu_g$, where μ_g is the thermal diffusion length in the gas column, as calculated in Figure 2.2. (Adapted from Ref. [1.1])

When the PA cell's dimensions in the y- and z-directions are much smaller than that in the x-direction, the photoacoustic effect can be described as shown in figure 2.1. In this case, the thermal diffusion process occurs only along one axis, x. Several assumptions have been made with regard to the PA system:

1. The length of the cell (l_g) is far greater than the acoustic wavelength.

2. The incident excitation light source is monochromatic and modulated.

$$I = \frac{I_0}{2}(1 + \cos(\omega t))$$
 , where $\omega = 2\pi f$ is the angular modulation frequency and I_0 is the incident light intensity.
3. The gas and backing material do not absorb light.
4. The backing material is thermally thick.
5. The system is adiabatic.
6. The PA cell window is optically and thermally transparent.

Neglecting semiconductor carrier diffusion and recombination effects, the heat density generated in the sample ($-l_s \leq x \leq 0$) due to the light absorption is given by

$$H(x,t) = \frac{\eta\beta I_0 e^{\beta x}}{2}(1 + \cos \omega t) = \frac{\beta I_0 e^{\beta x}}{2}(1 + \cos \omega t) \quad (2.1)$$

where β is the optical absorption coefficient and x is a negative number when the heated position is under the sample surface. We assume that the optical energy will be absorbed only within the sample and converted to heat by non-radiative de-excitation processes with efficiency η . In the R-G theory, the radiative de-excitation process is neglected, which will be discussed later for photoacoustic materials for semiconductors in section 2.3. Therefore, $\eta=1$ in equation 2.1 above.

Using one-dimensional heat equation, equation 2.2 incorporates the effect of the distributed heat source, due to the incident light, into the thermal diffusion

process within the sample. Similarly, the one dimensional thermal diffusion process within the gas column and backing material without heating sources is given by the equation 2.3 and 2.4.

$$\frac{\partial^2 T(x,t)}{\partial x^2} = \frac{1}{\alpha_s} \frac{\partial T(x,t)}{\partial t} - Ae^{\beta x} (1 + e^{j\alpha t}), \text{ when } -l_s \leq x \leq 0 \quad (2.2)$$

$$\frac{\partial^2 T(x,t)}{\partial x^2} = \frac{1}{\alpha_b} \frac{\partial T(x,t)}{\partial t}, \text{ when } -(l_b + l_s) \leq x \leq -l_s \quad (2.3)$$

$$\frac{\partial^2 T(x,t)}{\partial x^2} = \frac{1}{\alpha_g} \frac{\partial T(x,t)}{\partial t}, \text{ when } 0 \leq x \leq l_g \quad (2.4)$$

where $T(x,t)$ is the spatially and temporally dependent temperature and α is the thermal diffusivity, described in equation 2.9.

$$A = \frac{\beta I_0 \eta}{2k_s} \quad (2.5)$$

where k is the thermal conductivity and η is the heat converting efficiency via non-radiative de-excitation processes; $\eta=1$ as mentioned previously. I_0 is the light intensity impinging on the sample surface.

As for the solution of equation 2.2, 2.3 and 2.4, the temperature distribution inside the PA cell is given by the following expression:

$$T(x,t) = \frac{1}{l_b} (x + l + l_b) W_0 + We^{-\sigma_b(x+l)} e^{j\alpha t}, \text{ when } -(l_b + l_s) \leq x \leq -l_s \quad (2.6)$$

$$T(x,t) = e_1 + e_2 x + de^{\beta x} + (Ue^{\sigma_s x} + Ve^{-\sigma_s x} - Ee^{\beta x}) e^{j\alpha t}, \text{ when } -l_s \leq x \leq 0 \quad (2.7)$$

where U , V , e_1 and e_2 are constant, E is defined in equation 2.17, the other symbols are defined through Equation 2.9 to 2.16.

$$T(x,t) = \frac{l_g - x}{l_g} \theta_0 + \theta e^{-\sigma_s x} e^{j\omega t}, \text{ when } 0 \leq x \leq l_g \quad (2.8)$$

where $\sigma = (1 + j)a$, as described later in equation 2.12. W is the time dependent component of the temperature relative to the ambient temperature T_0 at the interface between the sample and backing material. W_0 is the time independent component of the temperature relative to the ambient temperature T_0 at the sample-backing interface ($x = -l_s$). θ is the time dependent component of the temperature relative to the ambient temperature T_0 at the interface between the sample and coupling gas. θ_0 is the time independent component of the temperature relative to the ambient temperature T_0 at the sample surface ($x = 0$).

$$\alpha = \frac{k}{\rho C} \quad (2.9)$$

where k is the thermal conductivity ($\text{Wm}^{-1}\text{K}^{-1}$), ρ is the density, C is the specific heat and α is the thermal diffusivity (m^2s^{-1}).

$$a = \sqrt{\frac{\omega}{2\alpha}} \quad (2.10)$$

where a (defined as the thermal diffusion coefficient in the R-G theory) is a frequency dependent thermal diffusion parameter with units of m^{-1} , analogous to the thermal absorption coefficient. As illustrated by equation 2.9, the thermal diffusivity α is one of the material properties, which is independent of the modulation frequency of the incident light. The thermal diffusion coefficient, a , is

frequency dependent and the higher the modulation frequency, the bigger is the thermal diffusivity and the shorter is the thermal diffusion length within the sample material.

μ is the thermal diffusion length

$$\mu = \frac{1}{a} \quad (2.11)$$

and

$$\sigma = (1 + j)a \quad (2.12)$$

where σ is the adapted thermal diffusion coefficient including an extra 45 degree phase shift. It is a complex number due to both spatial and time dependant variation of the thermal diffusion process. The equality of the real and imaginary components dictates that the thermal energy emerging at the sample surface experiences this 45° phase shift.

$$d = \frac{I_0}{2\beta k_s} \quad (2.13)$$

$$E = \frac{\beta I_0}{2k_s (\beta^2 - \sigma_s^2)} \quad (2.14)$$

where k_s is the thermal conductivity within the sample material and σ_s is the adapted thermal diffusion coefficient within the sample materials. To get the expression for the temperature variation at the sample surface θ , the following boundary conditions for temperature and heat flux continuity at the sample-gas and sample-backing interfaces are considered.

$$\begin{aligned}
T_g(0,t) &= T_s(0,t) \\
k_g \frac{\partial T_g(0,t)}{\partial x} &= k_s \frac{\partial T_s(0,t)}{\partial x} \\
T_b(-l_s,t) &= T_s(-l_s,t) \\
k_b \frac{\partial T_b(-l_s,t)}{\partial x} &= k_s \frac{\partial T_s(-l_s,t)}{\partial x}
\end{aligned} \tag{2.15 a}$$

where T_g , T_s and T_b is the temperature in the gas media, sample and backing materials; k_g , k_s and k_b is the thermal conductivity in the gas media, sample and backing materials; l_s is the sample thickness; t is time and x is location.

Applying the boundary conditions of 2.15a above to the equations 2.6, 2.7 and 2.8, it yields [1.1, pp. 98-100]:

$$\begin{aligned}
T &= U + V - E \\
W_0 &= e_1 - l_s e_2 + d e^{-l_s x} \\
T_0 &= e_1 + d \\
W &= U e^{-l_s \sigma_s} + V e^{l_s \sigma_s} - E e^{-l_s \beta} \\
\frac{-k_g \theta_0}{l_g} &= (e_2 + \beta d) k_s \\
\frac{k_b W_0}{l_b} &= (e_2 + \beta d e^{-l_s \beta}) k_s \\
-k_g \sigma_g \theta &= k_s (\sigma_s U - \sigma_s V - \beta E) \\
k_b \sigma_b W &= k_s (\sigma_s U e^{-l_s \sigma_s} - \sigma_s V e^{l_s \sigma_s} - \beta E e^{-l_s \beta})
\end{aligned} \tag{2.15 b}$$

Solving the equations of 2.15b above, the resulting time dependent temperature at the sample surface, θ , is [1.1, pp. 98-100]

$$\theta = \frac{\beta I_0}{2k_s(\beta^2 - \sigma_s^2)} \left[\frac{(r-1)(b+1)e^{l_s\sigma_s} - (r+1)(b-1)e^{-l_s\sigma_s} + 2(b-r)e^{-\beta l_s}}{(g+1)(b+1)e^{l_s\sigma_s} - (g-1)(b-1)e^{-l_s\sigma_s}} \right] \quad (2.15 \text{ c})$$

where

$$r = \frac{\beta}{\sigma_s} \quad (2.16)$$

$$b = \frac{k_b\sigma_b}{k_s\sigma_s} \quad (2.17)$$

$$g = \frac{k_g\sigma_g}{k_s\sigma_s} \quad (2.18)$$

It can be concluded that the time dependent temperature component within the gas column, θ , is represented by a complex valued function. It has a phase and amplitude relationship with the ac component of the incident excitation light intensity.

Investigation of the temperature distribution in the gas column in equation 2.8 shows that it is composed of temporally dependent and independent components. Since only the time varying component is responsible for the creation of the pressure fluctuations in the gas, the time independent component θ_0 may be neglected and the ac component of the temperature variation inside gas column can be expressed as:

$$T_{gAC}(x,t) = \theta e^{-\sigma_g x} e^{j\omega t} \quad (2.19)$$

Plotting equation 2.19 for various phases, Rosencwaig and Gersho found that the time dependent component would be fully damped out at a distance of approximately $2\pi\mu_g$ from the sample-gas interface.[1.1] Let us consider a simple PA system, where the sample is a silicon wafer of 500 μm thickness, the backing material is aluminium and the coupling gas is air. A 300 W arc lamp (modulation frequency = 100 Hz) is used as the excitation light source. As shown in Figure 2.2, the temperature variation in the gas column can be neglected when the temperature sensor is placed >1 mm away from the sample surface.

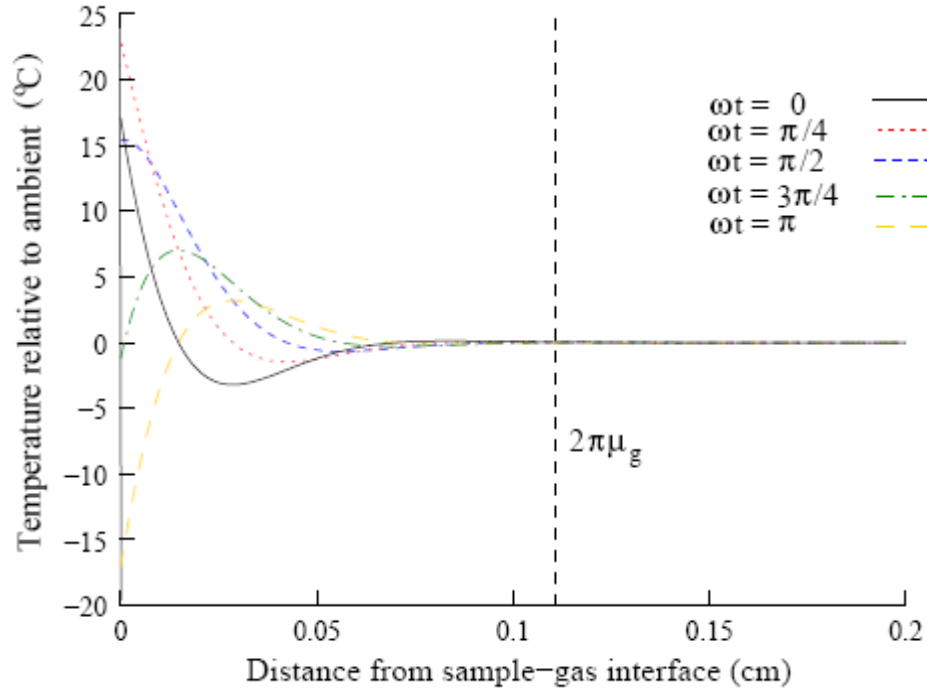


Figure 2.2: Spatial distribution of the time-dependent temperature within PA cell for a 500 μ m thick silicon sample. The backing material is aluminum, the coupling gas is air and a 300 W arc lamp is used as the light source, modulated at 100 Hz.

Therefore, one can define a boundary length in the gas that is thermally excitable by the sample. In this region, periodic expansion and contraction takes place, which acts as an “acoustic piston” with a volume velocity related to the modulated excitation light intensity. The piston compresses the rest of the gas column inside the PA cell and produces an acoustic wave that travels the entire length of the gas column. The acoustic piston length with air and helium coupling gas has been plotted as a function of modulation frequency. As shown in Figure 2.3, the acoustic piston thickness in helium is much greater than that in air at all frequencies. The consideration of acoustic piston length is important when designing a photoacoustic characterization instrument, as it defines the lower limit of the PA cell volume. Tam and Wong have reported that the highest PA

signal amplitude can be achieved when the gas column length l_g is roughly about $1.8 \mu_g \cdot [2.1, 2.2]$

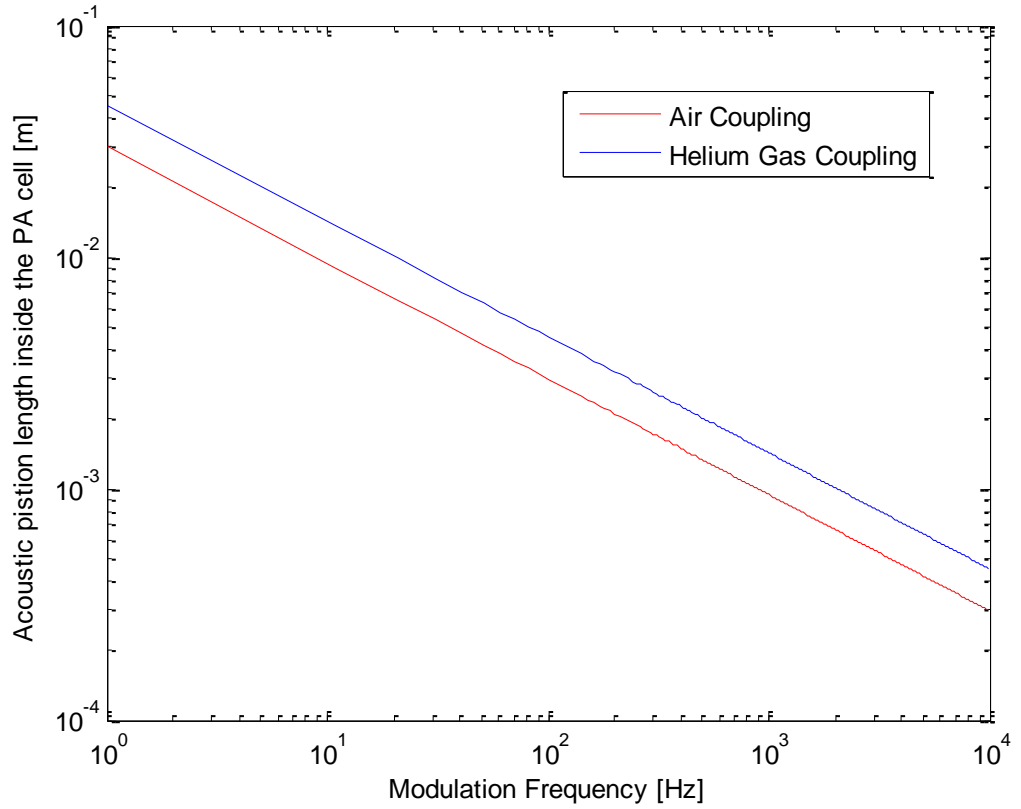


Figure 2.3: Acoustic piston length, $2\pi\mu_g$, as a function of modulation frequency for air and helium coupling gas inside the PA cell, calculated using $C_{\text{helium}} = 5.193 \text{ J/gK @ } 300\text{K}$, $\rho_{\text{helium}} = 178.7 \text{ g/m}^3$, $k_{\text{helium}} = 0.1513 \text{ W/mK}$, $C_{\text{air}} = 1.047 \text{ J/g} \cdot \text{K}$, $\rho_{\text{air}} = 616 \text{ g/m}^3$, $k_{\text{air}} = 0.0457 \text{ W/mK}$

For smaller values of l_g , the temperature variation in the gas column will be reduced due to direct heat diffusion losses through the optical window. The PA signal intensity decreases with decreasing air volume and follows roughly a linear

l_g and f^{-2} dependency. For a gas column length longer than $1.8\mu_g$, the PA signal decreases with increasing gas volume and exhibits l_g^{-1} and f^{-1} dependency [2.1, 2.2]. According to Figure 2.3, it is perfectly reasonable to choose 4 mm as the gas column length for the photoacoustic cell design, within the frequency probe range from 10^2 Hz to 10^4 Hz for both air and helium gas coupling.

The spatially averaged temperature of the gas within the acoustic piston length can be calculated by obtaining the spatial mean of equation (2.19) as follows:

$$\bar{T}_g(t) = \frac{1}{2\pi\mu_g} \int_0^{2\pi\mu_g} T_{gAC}(x,t) dx \quad (2.20)$$

Using the approximation $e^{-2\pi} \ll 1$, equation 2.20 yields:

$$\bar{T}_g(t) \approx \frac{1}{2\sqrt{2\pi}} \theta e^{j(\omega t - \pi/4)} \quad (2.21)$$

where θ is the time dependent temperature at the sample surface calculated in equation 2.15. The volume of the acoustic piston expands thermally as the mean temperature increases inside the cell and can be expressed by

$$\left(\frac{\partial V}{\partial T}\right)_P = \beta_T V \quad (2.22)$$

where β_T is the thermal cubic expansion coefficient of the adiabatic gas. Since β_T is a constant value for the coupling gas, using equation 2.22, the gas volume variation induced by the periodical heating can be calculated as

$$\partial V = V \frac{\partial T}{T_0} \quad (2.23)$$

where $V = \pi\left(\frac{D}{2}\right)^2 2\pi\mu_g$, is the acoustic piston volume and D is the diameter of the photoacoustic cell.

The remainder of the gas inside the PA cell is compressed by the acoustic piston and an increase in pressure in the PA cell can be detected by a microphone sensor. As the system is assumed to be adiabatic, the ideal gas law may be applied to the whole PA cell gas column assuming l_g is far bigger than $2\pi\mu_g$

$$PV^\gamma = C \quad (2.24)$$

$$\partial P(t) = -\gamma \frac{P_0}{V_0} \partial V(t) \quad (2.25)$$

where C is a constant value in equation 2.24. P_0 is the ambient pressure, V_0 is the PA cell volume and γ is the ratio of the molar specific heats at constant pressure.

The pressure variation within the cell is calculated through two steps. The first step is the volume variation induced by the temperature increment. Since $2\pi\mu_g$ is much smaller than the total length of the gas volume within the cell l_g , the total temperature change within the photoacoustic cell can be calculated as a weighted fraction of \bar{T}_{gAC} :

$$\partial T \approx \frac{2\pi\mu_g}{l_g} \bar{T}_{gAC}(t) \quad (2.26 \text{ a})$$

Combining equations 2.23 and 2.26a yields:

$$\partial V(t) = \frac{2\pi\mu_g}{l_g} \bar{T}_{gAC}(t) \frac{V_0}{T_0} \quad (2.26 \text{ b})$$

The second step for calculation is to estimate the pressure variation induced by the gas volume change. Combining equations 2.26b and 2.25, pressure variation inside the PA cell now can be mathematically described as:

$$\partial P(t) = \frac{2\pi\mu_g}{l_g} \gamma \frac{P_0}{T_0} \bar{T}_{gAC}(t) \quad (2.26 \text{ c})$$

The pressure variation, also called the photoacoustic signal, can be broken into two components, which comprises of both the amplitude and phase signals. By inserting equations 2.21 and 2.15c into equation 2.26c above, the acoustic signal can be calculated as

$$\partial P(t) = Q e^{j(\omega t - \pi/4)} \quad (2.26 \text{ d})$$

$$Q = \frac{\beta I_0 \gamma P_0}{2\sqrt{2} k_s l_g a_g T_0 (\beta^2 - \sigma_s^2)} \left[\frac{(r-1)(b+1)e^{l_s \sigma_s} - (r+1)(b-1)e^{-l_s \sigma_s} + 2(b-r)e^{-\beta l_s}}{(g+1)(b+1)e^{l_s \sigma_s} - (g-1)(b-1)e^{-l_s \sigma_s}} \right] \quad (2.27)$$

where Q is a complex number that specifies the complex envelope of the sinusoidal pressure variation. We define

$$Y = \frac{\gamma I_0 P_0}{2\sqrt{2} l_g T_0} \quad (2.28)$$

where Y is a constant independent of the material properties included in the PA system. Equation 2.27 can be simplified after inserting equation 2.28 as

$$Q = Y \frac{\beta}{k_s a_g (\beta^2 - \sigma_s^2)} \left[\frac{(r-1)(b+1)e^{l_s \sigma_s} - (r+1)(b-1)e^{-l_s \sigma_s} + 2(b-r)e^{-\beta l_s}}{(g+1)(b+1)e^{l_s \sigma_s} - (g-1)(b-1)e^{-l_s \sigma_s}} \right] \quad (2.29)$$

As shown in equations 2.26, 2.27 and 2.29, R-G theory presents a complete model for the photoacoustic effect of one homogeneous sample placed on a thermally thick backing material inside an airtight chamber. The photoacoustic signal is a complex function oscillating at the same frequency as the modulated excitation light source. The amplitude and phase of the PA signal are frequency dependent and can be used to characterise the optical and thermal properties of the sample. These conclusions can be applied to samples with various optical and thermal properties and can be directly used to interpret the experimental data from the PA system developed in subsequent chapters.

2.2

Simplified Rosencwaig-Gersho Theory: Special Cases

From the previous section, it is obvious that the mathematical expression for the PA signal is quite complicated, particularly due to the complex nature of Q in equations 2.27 and 2.29. To overcome this problem, Rosencwaig and Gersho developed a simplified theory using physical insight for the special cases. For example,

- When the sample thickness is greater than the thermal diffusion length, the sample is considered “thermally thick”. Otherwise, the sample is considered to be “thermally thin”.

- When the sample thickness is smaller than optical absorption length, the sample is considered “optically transparent”. Otherwise, the sample is considered to be “opaque”.

Therefore, by comparing the values of optical absorption length, thermal diffusion length in the sample and sample thickness, PA samples can be grouped into 6 simplified cases. In the equations below, as defined by R-G theory, μ_β is the optical absorption length, μ_s is thermal diffusion length in the sample, μ_b is the thermal diffusion length in the backing material and l_s is the sample thickness. As also defined in Figure 2.1, the subscripts g, s and b below refer to the material properties for gas, sample and backing material, respectively. For further elaboration the reader is referred to [1.1, pp. 104-107] and [4.7]

2.2.1

Case 1: Optically transparent and thermally thin samples ($\mu_s \gg l_s$, $\mu_s > \mu_\beta$ and $\mu_\beta > l_s$)

In this case, $e^{-\beta l_s} = 1 - \beta l_s$, $e^{\pm \delta_s l_s} = 1$ and $|r| > 1$. Equation 2.29 can be simplified as

$$Q = \frac{(1-j)\beta l_s}{2a_g} \left(\frac{\mu_b}{k_b}\right) Y \quad (2.30)$$

As can be seen in equation 2.30, the PA signal intensity is linearly proportional to βl_s . According to equation 2.10 and 2.11, $\frac{\mu_b}{k_b} \frac{1}{a_g}$ is proportional to ω^{-1} . Thus

the PA signal intensity has a ω^{-1} dependency on the modulation frequency of the excitation light source.

2.2.2

Case 2: Optically transparent and thermally thin ($\mu_s > l_s, \mu_s < \mu_\beta$)

In this case, $e^{-\beta l_s} = 1 - \beta l_s$, $e^{\pm \delta_s l_s} = 1 \pm \delta_s l_s$ and $|r| < 1$ Equation 2.29 can now be simplified as

$$Q = \frac{(1-j)\beta l_s}{2a_g} \left(\frac{\mu_b}{k_b}\right) Y \quad (2.31)$$

In fact, it is identical to equation 2.30. For both cases with the thermally thin samples, the backing material properties have to be taken into account for the PA signal estimation, via dependency on $\frac{\mu_b}{k_b}$.

2.2.3

Case 3: Optically transparent and thermally thick ($\mu_s < l_s, \mu_s \ll \mu_\beta$)

In this case, $e^{-\beta l_s} = 1 - \beta l_s$, $e^{\pm \delta_s l_s} = 0$ and $|r| \ll 1$. Equation 2.29 can be simplified as

$$Q = \frac{-j\beta\mu_s}{2a_g} \left(\frac{\mu_s}{k_s}\right) Y \quad (2.32)$$

In comparison with equation 2.31, the $\beta\mu_s$ term is used here instead of βl_s . Thus, only the light absorbed within the thermal diffusion length contributes to the PA signal.

2.2.4

Case 4: Optically opaque and thermally thin ($\mu_s \gg l_s$, $\mu_s \gg \mu_\beta$ and $\mu_\beta < l_s$)

In this case, $e^{-\beta l_s} = 0$, $e^{\pm \delta_s l_s} = 1$ and $|r| \gg 1$. For this situation, equation 2.29 can be simplified as

$$Q = \frac{(1-j)}{2a_g} \left(\frac{\mu_b}{k_b} \right) Y \quad (2.34)$$

Here, the PA signal is independent of the optical absorption coefficient. This conclusion is very important, particularly when studying the semiconductor bandgap structures using PA spectroscopy. When the photon energy of the excitation light source is greater than that of the semiconductor bandgap, the semiconductor sample is optically opaque. Thus the PA system is not sensitive to optical absorption processes above the bandgap.

In a fashion similar to equations 2.30 and 2.31, the PA signal intensity also depends on the properties of the backing material and is inversely proportional to the chopping frequency

2.2.5

Case 5: Optically opaque and thermally thick ($\mu_s < l_s$, $\mu_s > \mu_\beta$ and $\mu_\beta < l_s$)

In this case, $e^{-\beta l_s} = 0$, $e^{\pm \delta_s l_s} = 0$ and $|r| > 1$. Equation 2.29 can now be simplified as

$$Q = \frac{(1-j)}{2a_g} \left(\frac{\mu_s}{k_s} \right) Y \quad (2.35)$$

where the PA signal is independent of the backing material and the optical absorption coefficient.

2.2.6

Case 6: Optically opaque and thermally thick ($\mu_s \ll l_s$, $\mu_s < \mu_\beta$ and $\mu_\beta < l_s$)

In this case, $e^{-\beta l_s} = 0$, $e^{\pm \delta_s l_s} = 0$ and $|r| < 1$. Here, equation 2.29 can be simplified as

$$Q = \frac{-j\beta\mu_s}{2a_g} \left(\frac{\mu_s}{k_s}\right) Y \quad (2.36)$$

This case is very interesting. Although the sample is still optically opaque, the PA signal intensity is proportional to $\beta\mu_s$ and is sensitive to the optical absorption coefficient. However, this conclusion is only valid when the thermal diffusion length is smaller than the optical penetration depth. Considering the modulation frequency range used in the PA system described in this thesis, i.e. from 100 Hz to 10 kHz, the typical thermal diffusion length in silicon is of the order of hundreds of microns. This is far bigger than the typical optical penetration depth, which is of the order of hundreds of nanometres, when the incident photon energy is above the semiconductor bandgap energy. Therefore, it is still valid to conclude that the PA system developed here is not sensitive to optical absorption processes above the semiconductor bandgap.

2.3

Photoacoustic Theory For Semiconductor Materials

The R-G theory assumes that the heat is generated instantaneously at the point in the sample where the light is absorbed. Therefore the distribution of the heat source is governed by the light source intensity (e.g. Gaussian profile), which decreases away from the surface in an $e^{-\beta x}$ fashion. However, in reality, the light absorption process will create electron-hole pairs in the sample, which will exist

for a certain period of time and move around before converting their energy to other forms, such as heat, etc.

When the incident light energy is above the semiconductor material bandgap energy, the optical absorption coefficient is high and the generated excess carriers are very close to the illuminated semiconductor surface. Most of the heat will be created by the surface recombination of those excess carriers. The recombination process will be so fast that the transport properties of the carriers will not affect the photoacoustic response and the R-G theory is sufficient to describe this photoacoustic effect. On the other hand, when the incident light energy is below the semiconductor bandgap energy, the optical absorption coefficient is low and light penetrates deep into the bulk of the semiconductor material. In this case, there is a substantial number of photo-excited carriers, whose diffusion effect will play an important role in the generation of the photoacoustic signal.

Bandeira *et al.* and several other groups have developed the theory of the photoacoustic effect in semiconductor materials, which includes the excess carrier diffusion effect. [2.3, 2.4, 2.5, 2.6, 2.7, 2.8, 2.9, 2.10]

To summarize the aforementioned work, there are two major differences between the photoacoustic theory for semiconductor materials and non-semiconductor materials. For semiconductor samples, the light absorption can only introduce photoexcited carriers and there is no direct heating effect. The heat is generated in the subsequent interaction of these carriers with the sample. In addition, the heat flux at the gas and semiconductor material interface is no longer continuous. Extra heat is created by the surface recombination of excess carriers.

PHOTOACOUSTIC SYSTEM DESIGN AND NOISE ANALYSIS

3. Photoacoustic System Design and Noise Analysis

3.1 Introduction

In the previous chapter, the theory of photoacoustic effect in condensed matter is illustrated. In this chapter, this theory is used as a guideline to design and construct a photoacoustic cell.

For the “conventional” PA spectroscopy design, the operation of the system is as follows. The polychromatic light from a 300 W Xenon arc lamp is first modulated by the optical chopper and then focused onto the entrance slit of a monochromator. The intensity-modulated light undergoes diffraction in accordance with the diffraction equation:

$$g\lambda = a \sin \theta \tag{3.1}$$

where g is the order of the reflection, λ is the monochromatic diffracted light, a is the line spacing of the grating and θ is the diffraction angle. This is the special case for the grating equation, $g\lambda = a(\sin \theta + \sin \theta_i)$, when the light incidence angle, θ_i , equals to 0° . A band-pass color filter is placed at the output port of the monochromator to block the harmonic wavelength contributions. The spectroscopic resolution of the PAS system is determined by the open slit width at the output of the monochromator. The narrower the slit opening, the better the spectroscopic resolution and the lower the output light intensity. The PA system presented here provides a typical output light intensity of about 12 mW, when setting the monochromator output wavelength at 1,000 nm (blazing wavelength of the grating). The monochromatic light enters a focus sub-system

and is subsequently incident on the semiconductor sample. The optical energy is absorbed by the sample and converted to the periodical thermal expansion of the gas volume within the PA cell via the photoacoustic effects, which is subsequently detected using microphones. Due to the low incident light intensity and poor conversion efficiency of the absorbed light into a detectable gas expansion within the PA cell, the typical microphone signal suffers a low signal to noise ratio (SNR), even when a pre-amplifier and lock-in amplifier are used for the PA signal processing. Currently, photoacoustic spectrometers for gaseous substances are more commercially available [1.3], because of a more significant PA effect and the relatively simpler models for the data interpretation. The PA spectra for condensed matter, such as semiconductor wafers, is more difficult to obtain and relatively more complex to model.

Various in-house PA systems have been developed to maximize the performance for different and specific experimental conditions. [3.1-3.5] One of the most commercially successful systems is the PAS cell provided by *MTEC Photoacoustics Inc.* [3.5]. That system is constructed as a detector head, which can be easily integrated into the standard FTIR spectrometers. The SNR is boosted using the FTIR method. It can increase the incident light intensity and reduces the signal accumulation time significantly. The typical analysis time to produce one useful spectrum is about 5 seconds. But, the energy range of that spectrometer is way below typical semiconductor band gap energies and practically useless for the analysis of bandgap defects. In addition, like any other PAS system published so far, the volume of the PA cell needs to be minimized to sustain a sufficient signal level for detection. The maximum sample size allowed in the MTEC system is only 5 mm in radius and 8 mm in height. [3.5]

To extend the PAS wavelength spectral range down to UV-VIS range, the PA system presented here uses the monochromator scanning method for the light

excitation, which is similar to that developed by Zegadi *et. al* at the University of Salford ca.1994. The PA cell design is optimized to improve SNR performance for the modulation frequency range and thermal wave probe depths of interest. Multi-channel acoustic signal acquisition, acoustic resonance provided by the cell geometry, an optimized band-pass filter and pre-amplification are considered in the PA cell design. The graphical user interface (GUI) is shared by both the PA spectroscopy (PAS) and the PA microscopy (PAM) systems. The optical excitation trains for the PAS and PAM systems is designed separately. One provides a broadband light source with the photonic energy in the range from 0.5 eV to 6.2 eV for the spectroscopy applications, while the other produces a very high probe intensity using a well collimated single wavelength laser source for the microscopic scanning.

3.2 Photoacoustic Spectrometer (PAS) and Microscopy (PAM) Specifications

In this section, the wavelength and modulation frequency rang is presented to meet the application requirements. In order to implement sub-bandgap defect energy analysis, the wavelength range for PA spectroscopy should cover the typical semiconductor band gap energy in the photonic interval from 0.5eV to 6.2eV, as shown in Table 3.1.

Material	Symbol	Band gap (eV) @ 300K
Silicon	Si	1.11
Germanium	Ge	0.67
Silicon carbide	SiC	2.86
Aluminium phosphide	AlP	2.45
Aluminium arsenide	AlAs	2.16
Aluminium antimonide	AlSb	1.6
Aluminium nitride	AlN	6.3
Diamond	C	5.5
Gallium(III) phosphide	GaP	2.26
Gallium(III) arsenide	GaAs	1.43
Gallium(III) nitride	GaN	3.4
Gallium(II) sulphide	GaS	2.5 (@ 295 K)
Gallium antimonide	GaSb	0.7
Indium(III) nitride	InN	0.7
Indium(III) phosphide	InP	1.35
Indium(III) arsenide	InAs	0.36
Zinc oxide	ZnO	3.37
Zinc sulphide	ZnS	3.6
Zinc selenide	ZnSe	2.7
Zinc telluride	ZnTe	2.25
Cadmium sulphide	CdS	2.42
Cadmium selenide	CdSe	1.73
Cadmium telluride	CdTe	1.49
Lead(II) sulphide	PbS	0.37
Lead(II) selenide	PbSe	0.27
Lead(II) telluride	PbTe	0.29
Copper(II) oxide	Cu ₂ O	2.17

Table 3.1: List of lowest selection of semiconductor band gaps: lowest energy transitions in each case [3.6, 3.7, 3.8, 3.9]

For PA microscopy, the thermal diffusion length determines the lateral resolution and probe depth. Combining equations 2.9, 2.10 and 2.11, the thermal diffusion length μ can be calculated as follows:

$$\mu_i = \sqrt{\frac{\kappa_i}{\pi f C_i \rho_i}} \quad (3.2)$$

where f , κ_i , C_i and ρ_i are the frequency at which the incident light source is amplitude modulated with an optical chopper, the thermal conductivity, the specific heat and density of the material i , respectively. For copper, $\kappa_{Cu} = 390 \text{ W} \cdot \text{m}^{-1} \cdot \text{K}^{-1}$, $C_{Cu} = 385 \text{ J} \cdot \text{kg}^{-1} \cdot \text{K}^{-1}$ and $\rho_{Cu} = 8900 \text{ kg} \cdot \text{m}^{-3}$. For silicon, $\kappa_{Si} = 390 \text{ W} \cdot \text{m}^{-1} \cdot \text{K}^{-1}$, $C_{Si} = 710 \text{ J} \cdot \text{kg}^{-1} \cdot \text{K}^{-1}$ and $\rho_{Si} = 2329 \text{ kg} \cdot \text{m}^{-3}$. As shown in figure 3.1 above, the thermal diffusion length within the isotropic silicon bulk material decreases from 350 μm to 100 μm by changing the modulation frequency from 250 Hz to 2,500 Hz. Therefore, the PA microscopy requires the capability to scan across the wafer with a 20 μm step size and a focused laser spot size smaller than 100 μm in order to achieve a reasonably high spatial resolution.

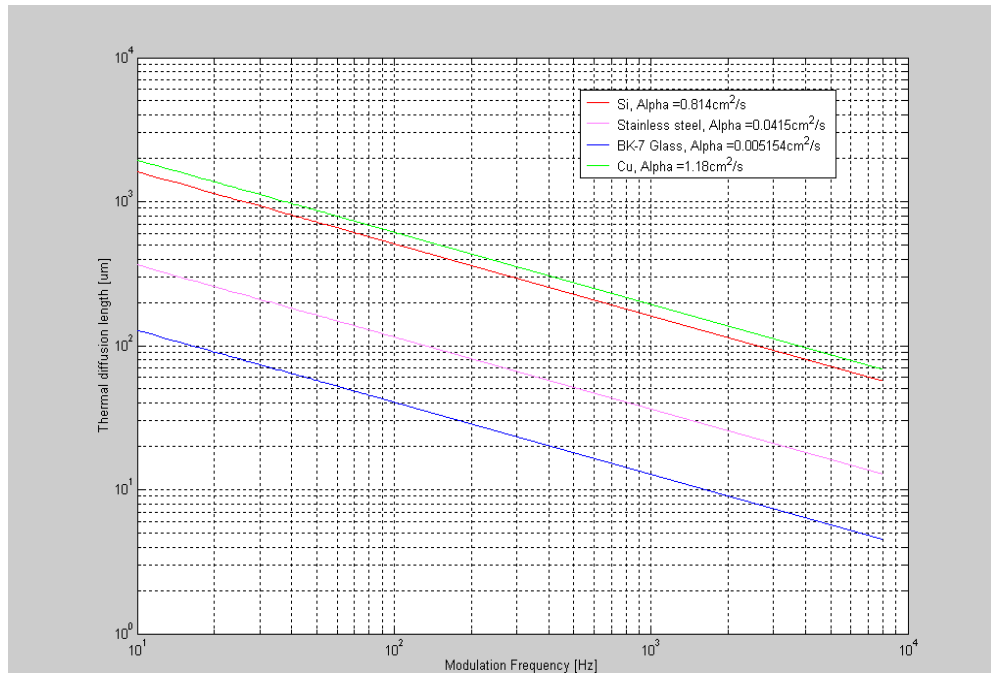


Figure 3.1: The thermal diffusion length decreases while increasing the modulation frequency

3.3 Overview of the Photoacoustic Spectrometer and Microscope

The PAS and PAM systems can be broken into several independent subsystems. As shown in Figure 3.2, for the spectroscopy system (PAS), the light source is a 300 W Xenon arc lamp (LOT Oriel model 6258), which provides a continuous light spectrum in the range of 0.5-6.2 eV. The light is modulated at a selected frequency by the optical chopper (LOT Oriel model 75170) mounted at the output port of the lamp housing (LOT Oriel model 66901). The modulated light is collimated and focused onto the entrance slit (LOT Oriel model 74001) of the ¼ m monochromator (Cornerstone 260 LOT Oriel model 74100). The resolution of the output monochromatic light (FWHM of the wavelength range of the output light) can be adjusted by the opening width of the monochromator output slit (LOT Oriel model 74001). A motorized filter wheel (LOT Oriel model

74010) is placed within the optical excitation path to cut off the diffraction of high order harmonics.

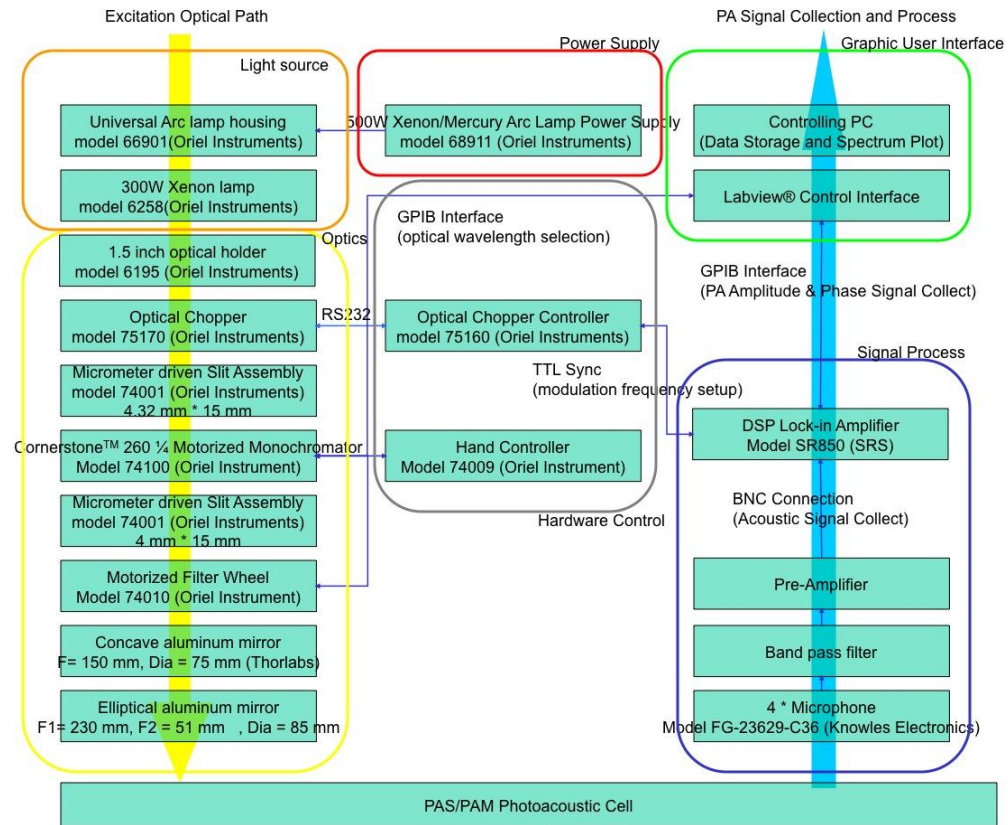


Figure 3.2: Schematics of the photoacoustic spectroscopy system (PAS)

The acoustic signal generated within the PA cell is collected by 4 microphones (Knowles model FG-23629-C36) and amplified before the signal detection using a DSP lock-in amplifier (Stanford Research Systems model SR830). A band pass filter is included in the pre-amp circuit to cut off the low frequency ambient noise. The photoacoustic signal measured in the PA cell is compared to the reference signal provided by the optical chopper controller. Both the amplitude and the phase of the PA signal are detected and sent to a PC via a GPIB interface. The monochromator and motorized filter wheel are also connected to the PC via a

GPIB interface and provide the hardware control functions to select the output wavelengths. The input of the optical chopper controller (LOT Oriel model 75160) is connected to the TTL sync-out port on the SR830 lock-in amplifier. It synchronizes the optical chopping frequency with the frequency generator within the lock-in amplifier. Using LabView® software, the PA signal and the information of the modulation frequency and the selected wavelength is collected by the PC. The results are shown within the GUI and saved on the local hard disk for further analysis.

The microscopy system (PAM) is presented in Figure 3.3. The laser light source is a ProLite® SF Series Fiber Coupled Single emitter (model SFB100-810-D2-01A) diode laser. The output wavelength is 808 nm with a typical spectral width of 3.5 nm. The maximum output power is 1.2 W. The laser diode is mounted on 762 series high-power laser diode mounts with a thermoelectric (TE) cooling module and sensor included. To provide a constant output power, a temperature controller (model 325B) is used to control the laser diode temperature with an accuracy of 0.2°C. The temperature is set to 22°C. The laser diode is powered by a Newport Laser diode drive (525B) with a typical operating current of 1.85A. The external input of the laser diode drive is connected to the TTL sync-out of the SR850 lock-in amplifier. The modulation frequency of the laser generated by the single emitter is synchronized with the frequency generator within the lock-in amplifier. The laser diode is pig-tailed and the emitted laser is coupled into an optical fibre with a core diameter of 100 µm. The light emitted at the end of the fibre is highly divergent. A confocal lens cage is used to collect the laser light, reshape the beam profile with a 200µm pinhole and focus the light into the PA cell with a working distance of 25.4 mm. The laser light source and the focusing lens are fixed in position during the laser scanning process.

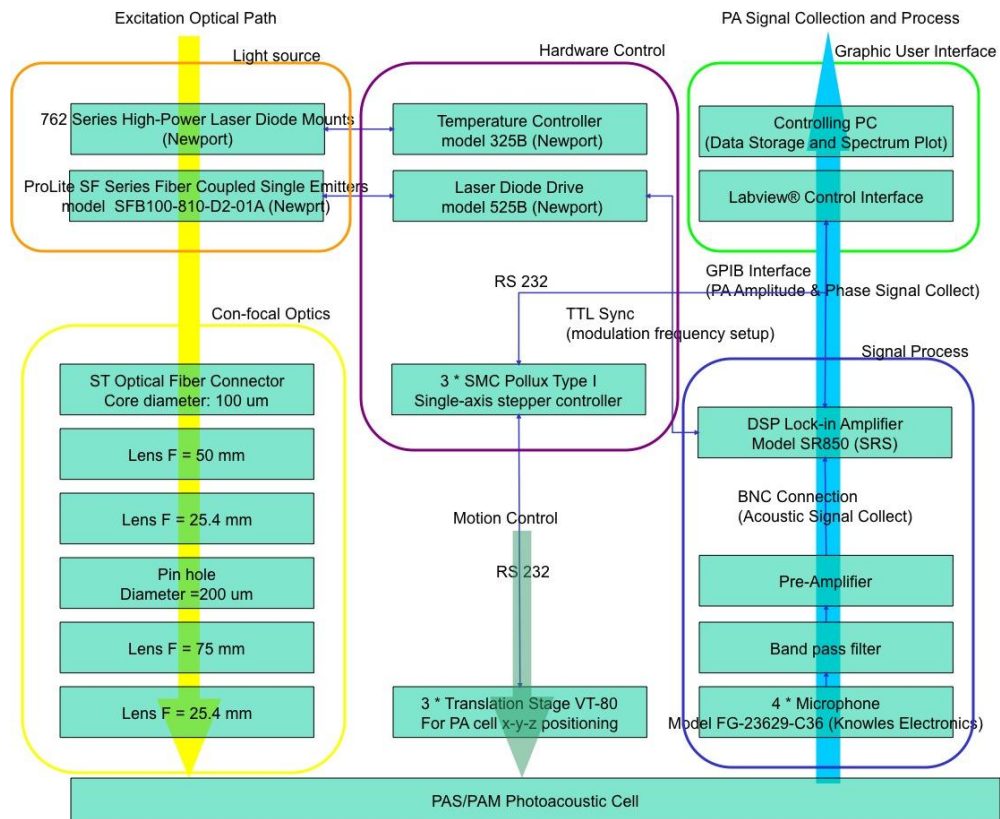


Figure 3.3: Schematics of the photoacoustic microscopy system (PAM)

The PA cell is mounted on two motorized stages (Micos® VT-80 Translation Stages) for X-Y positioning while scanning across the semiconductor samples with the laser beam. A single axis stepper controller (SMC Pollux Type I) is used to control each translation stage, through a D-sub connection. The motorized stage gives a bi-directional positioning repeatability of 15 μm . With the exception of the light source, optical excitation path and the motorized stage, the remainder of the subsystems, including the photoacoustic cell, the acoustic signal acquisition and processing, are the same for both microscopy (PAM) and spectroscopy (PAS) systems. Using LabView®, the information on the laser spot position, modulation frequency, PA amplitude and phase are collected by the controlling PC. In this way, wafer maps of the PA amplitude and phase can be plotted on the

screen. By changing the modulation frequency of the laser diode, the thermal diffusion length can be altered and the thermal imaging results with a variety of probe depths can be obtained.

3.4 Hardware description

3.4.1 Optical Hardware for Photoacoustic Spectroscopy

The primary purpose of the optical hardware is to create a high intensity, modulated, monochromatic light beam to induce the photoacoustic effect in the semiconductor samples.

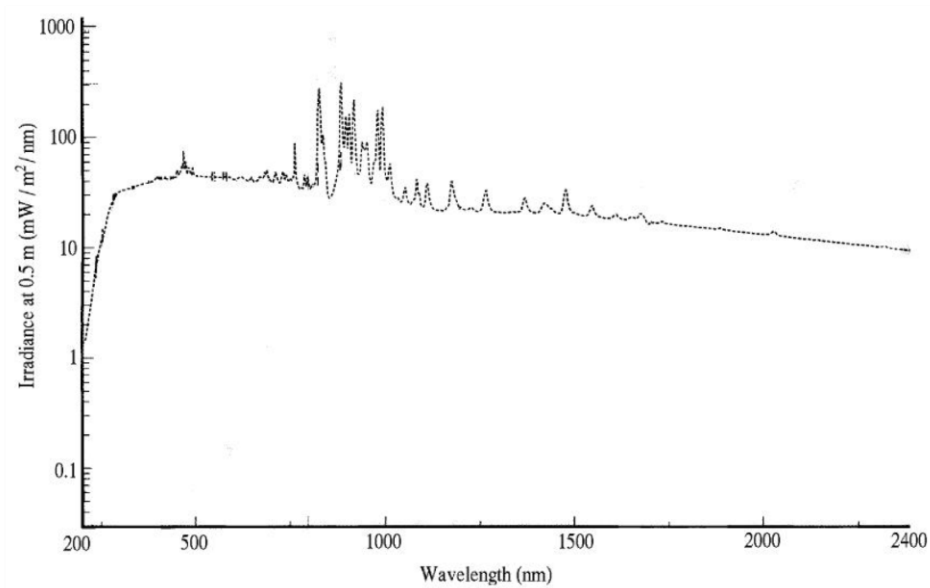


Figure 3.4: Spectral irradiance of 300 W ozone-free xenon arc lamp (LOT Oriel model 6258). Reproduced from [3.10]

To isolate the photoacoustic system from the ambient low frequency vibration, all of the optical hardware is mounted on a RP Reliance vibration damped optical table manufactured by Newport. The light source is a 300 W Short Arc Xenon lamp (model 6258), manufactured by LOT Oriel. The arc size is 0.7 mm * 2.4 mm. Within the arc lamp housing (model 66901), a parabolic reflector is situated behind the lamp to enhance the device efficiency. An f/1 primary condensing lens and an f/4.6 secondary coupling lens (f = 150 mm) is mounted at the output port of the lamp housing. The arc lamp is at the focal point of the primary condensing lens, which provides a collimated beam for the secondary lens. The secondary coupling lens is used to perform the f-number matching to maximize the light intensity throughput. The entrance slit of the monochromator is placed at its focal point, i.e. 150 mm away.

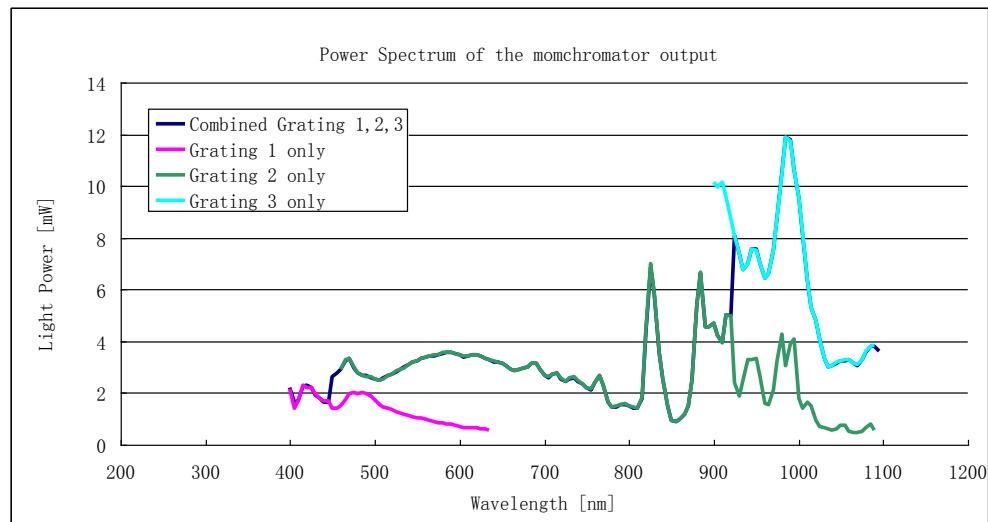


Figure 3.5: The output light power spectrum for the monochromator measured by a silicon photodiode (The exit slit width = 1.34 mm)

The lamp is ozone-free and can provide constant irradiance from 250 nm (Oxygen cut-off wavelength) to 2,400 nm. The spectral output of the lamp can be examined in Figure 3.4.

The optical chopper, LOT Oriel model 75170, is inserted in the path of the collimated beam between the primary and secondary condensing lenses. The optical chopper has been placed away from the photoacoustic cell to minimize the acoustic noise arising from the motor and the air being chopped. A controller (LOT Oriel model 75160) is used to control the chopping frequency. It varies from sub-Hz to 3kHz. For all the spectral results presented later, the modulation frequency is set at 70Hz to obtain relatively high PA amplitude. The reference signal for the optical chopper controller is provided by the TTL-sync-out signal from the lock-in amplifier. It insures zero frequency difference between the detection frequency and excitation frequency.

For the optical wavelength selection, a LOT Oriel Cornerstone 260 monochromator is used. It has entrance and exit focal lengths of 260mm, a relative aperture of f/3.9 and a potential operating range from 180 nm to 20 um depending on the diffraction grating used. The maximum wavelength-scanning rate is 175 nm/s. The monochromator has an accuracy of 0.35 nm and a wavelength repeatability of 0.08 nm.

Grating No	Type	No of the Grooves (l/mm)	λ range [nm]	Blaze λ [nm]
1	Holographic	1200	180 - 650	250
2	Ruled	1200	450 - 1400	750
3	Ruled	600	900 -2800	1600

Table 3.2: The gratings selected in the Cornerstone 650 monochromator

There are two types of the grating: holographic and ruled gratings. The holographic grating provides good spectral resolution at the expense of reduced intensity. The ruled grating offers increased light intensity with relatively poor spectral resolution. The resolution of the grating increases and the light throughput decreases as one increases the number of the grooves on the grating. The resolution of the Cornerstone 260 is 0.15 nm for a 1200 l/mm grating when

setting the entrance and exit slit size as 10 μm * 2 mm. As shown in Table 3.2, three gratings are selected here to enable the monochromator scan from 180 nm to 2400 nm. As shown in Figure 3.5, the monochromator output spectrum is measured using a silicon power meter. The result includes the combined effects of the monochromator throughput variation and the arc lamp power spectrum across the wavelength. Since this output spectrum is measured with a silicon photodiode, it has a limited detection range from 400 nm to 1,090 nm. The optical chopper was set open and the exit slit was closed slightly to a slit width of 1.34 mm to avoid signal saturation of the power meter.

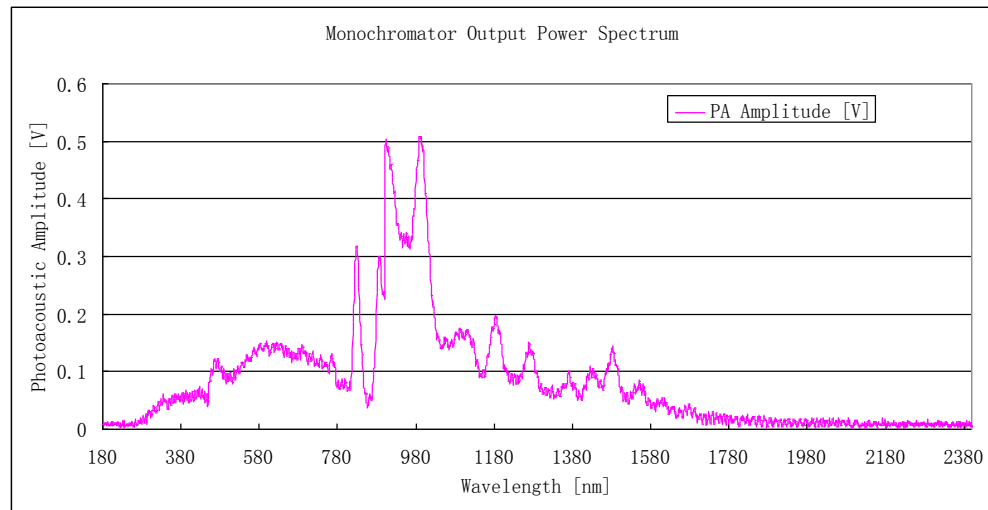


Figure 3.6: The monochromator output power spectrum measured using photoacoustic cell and carbon black powder. (Modulation frequency = 43 Hz, lock-in amplifier sensitivity = 500 mV, lock-in time constant = 30 ms, AC coupling, High reserve, negative edge triggering, scan range = 180 nm – 2400 nm)

It is worth noting that the spectrum, shown in Figure 3.5, does not represent a complete picture of the monochromator capability used in the PAS system, due to the limited spectral detectable range of the silicon photodiode. Using a combination of the PA cell and carbon black powder as the detector, the complete monochromator output spectral can be obtained with extended

wavelength range of 180-2400 nm. Carbon black powder, which has been widely used as a reference sample for the PA spectrum normalization, is considered to have a constant optical absorption coefficient across the wavelength. [1.3] Beyond ~1800 nm, the PA amplitude falls into the background noise level of about 12 mV. When comparing Figure 3.5 and 3.6, in the wavelength range from 400-1090 nm, the measured PA amplitude spectrum shows very similar features to those obtained using the silicon power meter.

The details of the PA cell and the processing electronics used in this measurement will be described later in this chapter.

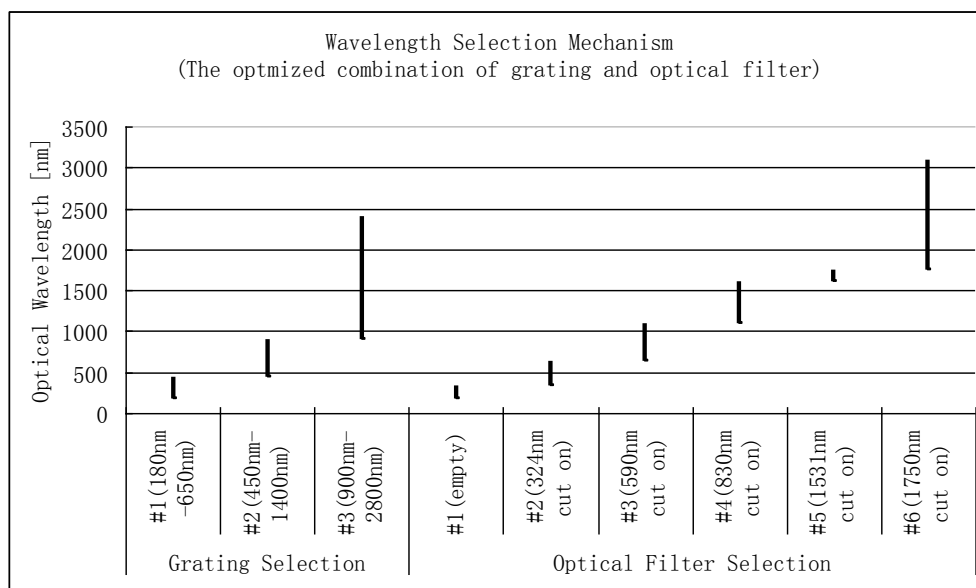


Figure 3.7: The wavelength selection mechanism (The output of the monochromator is determined by the combination of the selected grating and optical filter for each individual wavelength within the range of the PAS scanning spectrum.)

Coupled to the output slit of the Cornerstone 260 monochromator is the motorized filter wheel (Oriel Instruments model 74010). This optical filter is

necessary to remove the high order harmonic contamination in the output spectrum. Within the optical wavelength range of interest, the combination of the optical filter and grating has been optimized to achieve the highest throughput of the light power, as shown in Figure 3.7 and the Table 3.3. The filter change mechanism is controlled directly by the monochromator, which itself is controlled directly using a dedicated hand controller and the IEEE 488.2 GPIB communication protocols.

	Optical Filter Selection					
Filter no	#1	#2	#3	#4	#5	#6
Cut On λ [nm]	Empty	324	590	830	1531	1750
Max λ [nm]	339	633	1099	1614	1756	3099
Min λ [nm]	180	340	634	1100	1615	1757

	Grating Selection		
Grating no	#1	#2	#3
Designed λ range	(180nm-650nm)	(450nm-1400nm)	(900nm-2800nm)
Max λ [nm]	449	899	2400
Min λ [nm]	180	450	900

Table 3.3: The list of the gratings and the optical cut-on filters used in the PAS system. The wavelength limit of each color filter is determined by experiment to maximize the optical power throughput.

Since the photoacoustic effect is directly proportional to the intensity of the incident light source, we must maximize the power from the output port of the monochromator and focus it into an area as small as possible. Therefore, appropriate focusing optics is required, as shown in Figure 3.8.

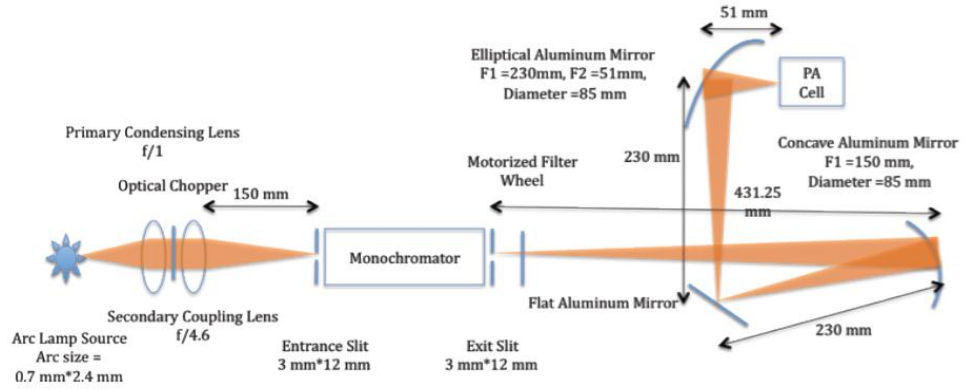


Figure 3.8: The optical setup for Photoacoustic Spectroscopy (PAS)

By way of example, suppose the monochromator is operated at 450 nm. The entrance and the exit slits are opened to 3 mm in width by 15 mm in height. Assume the power density provided by the arc lamp at 450 nm is 4.75 mW/nm and arc size is 0.7 mm * 2.4 mm. The magnification ratio of the condensing lens and the coupling lens can be calculated by the ratio of the f-number.

$$m = \frac{f / \#_{\text{secondary}}}{f / \#_{\text{condensor}}} = 4.6 \quad (3.3)$$

At the entrance of the monochromator, the image of the arc lamp source will be 3.2 mm in width and 11.0 mm in height. Assuming uniform image irradiance, the power entering the monochromator is proportional to the fraction of the image that passes through the entrance slit. Therefore, the light power P entering the monochromator is

$$P = 4.75 \text{ mW / nm} * \frac{3}{3.2} = 3.58 \text{ mW / nm} \quad (3.4)$$

At the exit slit of the monochromator, the bandwidth $\Delta\lambda$ can be calculated as

$$\Delta\lambda = \omega \frac{d\lambda}{dL} \quad (3.5)$$

where ω is the exit slit width and $\frac{d\lambda}{dL}$ is the reciprocal linear dispersion.

$$\begin{aligned} \therefore g\lambda &= a \sin \theta \\ \therefore \frac{d\theta}{d\lambda} &= \frac{g}{a \cos \theta} \\ \therefore \frac{dL}{d\lambda} &= f \frac{d\theta}{d\lambda} = \frac{fg}{a \cos \theta} \end{aligned} \quad (3.6)$$

where g is the order of the diffraction, a is the line space of the grating. At 450 nm, the reciprocal linear dispersion is calculated as 3.8 nm/mm. Consequently the power output at the exit slit of the monochromator is calculated as

$$P_{output} = P * \Delta\lambda * E_g R_m^4 * T_l^2 = P * \omega \frac{d\lambda}{dL} * E_g R_m^4 * T_l^2 = 10.49mW \quad (3.7)$$

where E_g (=50%) is the efficiency of the grating at 450 nm, R_m (=88%) is the reflectivity of the four aluminium mirrors integrated inside the monochromator, T_l (=90%) is the transparency of the primary condensing lens and secondary coupling lens across the wavelength of interest

The output beam size from the monochromator has been experimentally ascertained to be

$$w = 0.15u + 0.5 \quad \text{Horizontal beam size in mm} \quad (3.8)$$

$$h = 0.166u + 6.76 \quad \text{Vertical beam size in mm} \quad (3.9)$$

where u is the distance away from the output of the monochromator. A concave aluminium mirror with a focal length of 150 mm and a diameter of 75 mm has been used to collect the diffracted light and couple it into the acceptance angle of an off-axis elliptical mirror. The image distance of the concave mirror is set to be the same as the first focal length of the elliptical mirror to minimize the projected spot size within the photoacoustic cell.

Since the concave mirror is placed 431 mm away from the exit slit of the monochromator, the diffracted beam image expands to 65 mm in width and 78 mm in height. The diameter of the concave mirror has been selected as 75 mm to collect all the diffracted light to enhance the light throughput.

The projected spot size at the sample plane within the PA cell can be calculated as 0.6 mm in width and 2.6 mm in height.

$$\begin{aligned} w &= 3mm * \frac{230}{431} * \frac{51}{230} = 0.6mm \\ h &= 12mm * \frac{230}{431} * \frac{51}{230} = 2.6mm \end{aligned} \quad (3.10)$$

Assuming there is no significant energy loss due to imaging spot over-fill at the concave aluminium mirror, the light intensity measured at the sample plane can be calculated as

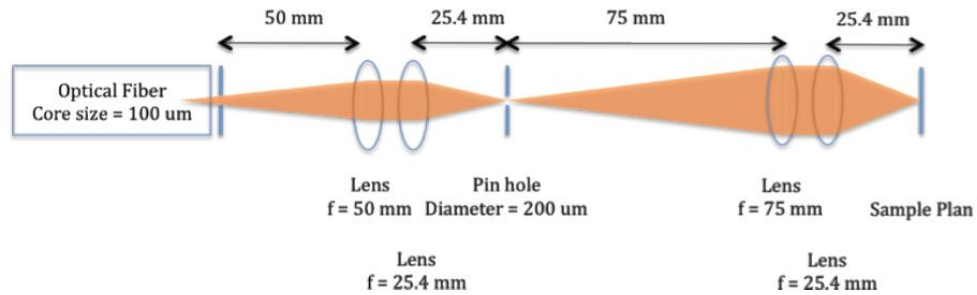
$$P_{incident} = P_{output} R_m^3 T_{filter} = 5.35mW \quad (3.11)$$

where T_{filter} (=70%) is the transparency of the cut-on color filter and R_m (=90%) is the aluminium reflectivity. This is of the same order as the measurement result shown in Figure 3.5.

3.4.2 Optical hardware for Photoacoustic Microscopy

The optics setup used for photoacoustic microscopy is much simpler compared to the PAS system. It has already been described in detail in section 3.3.

A confocal lens cage has been used to re-shape the beam profile emitted from the



pigtailed optical fibre, as shown in Figure 3.9.

Figure 3.9: The optics setup for Photoacoustic Microscopy (PAM)

The resulting beam diameter at the sample plane is calculated as:

$$D = 200\mu\text{m} * \frac{25.4\text{mm}}{75\text{mm}} = 67\mu\text{m} \quad (3.12)$$

The measured spot size is approx 100 μm within the photoacoustic cell, which is of the same order as the estimated laser spot size.

The laser diode light source is connected to the Newport Laser diode drive (525B). The diode drive current is set at 300 mA, when it is turned on. The TTL-sync signal generated by the lock-in amplifier is connected to the voltage input port of the laser diode drive. The averaged voltage supplied by the TTL-sync signal is 2.67 V, with an equivalent averaged current value of 667.5 mA (250 mA/V). The output current of laser diode drive is in the form of a square wave,

varying from 300mA to 1643mA. According to the laser diode spec sheet, the typical slope efficiency of the laser diode is 0.75W/A. The peak laser diode output power can thus be calculated to be 1.23mW.

3.4.3 Design of Photoacoustic Cell

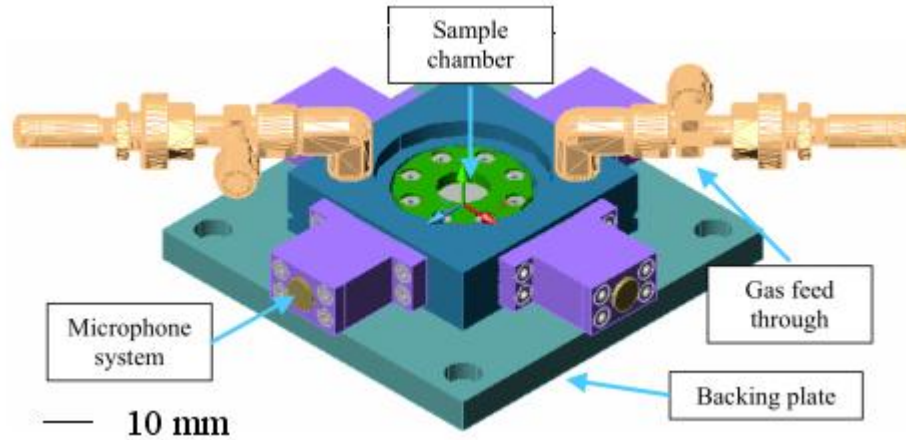


Figure 3.10: Schematic of the photoacoustic cell for PAS and PAM systems.

The schematic of the photoacoustic cell is illustrated in Figure 3.10. The size of the PA cell has been kept as small as possible to enhance the SNR of the PA signal. It is 16 mm in diameter and 9 mm in height. Several volume-reducing spacers have also been machined to fit at the bottom of the cell to further reduce the cell volume. Metering valves have been incorporated into the cell to facilitate the admittance of gas (helium) into the cell. The thermal conductivity of Helium gas is better than that of air, which can enhance the thermal diffusion process from the sample surface to the coupling gas volume. It can help to increase the PA signal level by a factor of 2. (The detailed calculation is given in Chapter 4.) The PA cell system contains four microphones (Knowles FG-23629-C36). Each microphone is contained in an individual housing to facilitate ease of replacement. Compared to the single microphone configuration, the SNR of n microphones can be reduced by a factor of \sqrt{n} due to the statistical averaging effect.

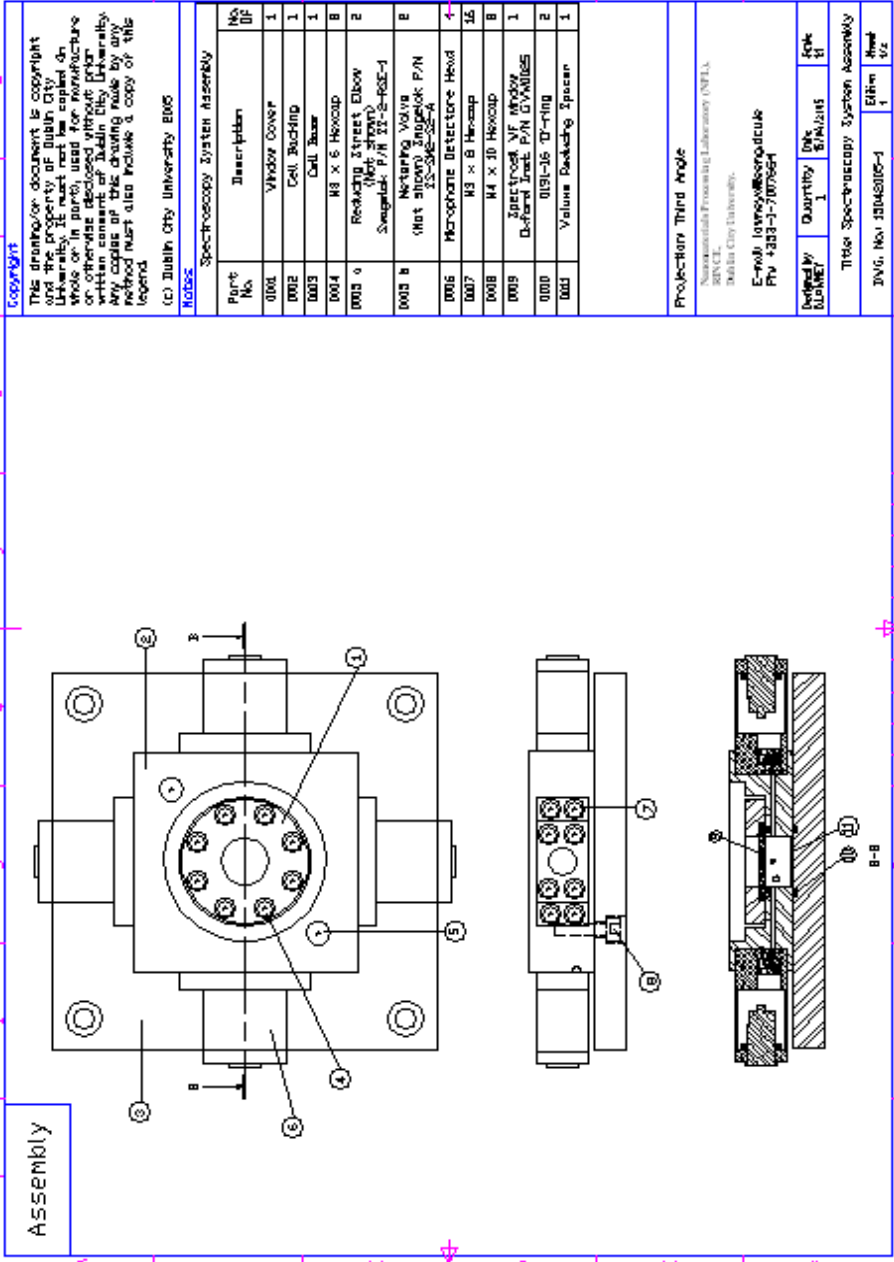


Figure 3.11: The assembly sheet of the photoacoustic cell (PA cell)

The cell can be bolted directly to an X-Y stage to facilitate spatially resolved photoacoustic measurements or can be used in a stand-alone configuration if desired. The X-Y stage consists of two VT-80 translation stages manufactured by Micos®, Germany. These stages have a 200 mm travel range, with bi-directional repeatability of ± 15 μm . The simple backing plate used to bolt the cell to the X-Y stage can also be replaced with a more sophisticated plate that incorporates a Peltier cooler for low-temperature PAS measurements or electrical feed-through for active device measurements. The assembly sheet for the individual components of the PA is illustrated in Figure 3.11.

3.4.4 Electronic system for photoacoustic signal processing and noise analysis

Noise is defined as any unwanted signal contribution, generated internally within or external to a signal processing system. Typical external noise sources include mains hum and RF interference; whilst internal noise signals arise from both discrete and passive devices. Respective examples include IC noise in transistors and Gaussian noise in resistors.

Noise is an inherent property of all physical systems. It can never be completely eliminated; it can only be reduced to an acceptable level. For systems where the signal level is inherently weak, as is typically the case in photoacoustic spectroscopy, one must strive to reduce all noise sources to their theoretical minimum. Contrary to popular belief, elimination of noise is not “black magic” and can be tackled methodically within the engineering paradigm [3.11].

In this section, the frequency response and self-noise of the microphone and pre-amplifier currently employed in the photoacoustic spectroscopy system are simulated. These models are used to determine the noise spectral density of the overall photoacoustic signal detector. The results of the model are compared with measurements of the system noise spectral density performed with the SR830 DSP lock-in amplifier.

3.4.4.1 System Frequency Response Microphone and Pre-amplifier

Consider the equivalent circuit for the microphone shown in Figure 3.12 [3.12]. The gain in the transformers is 1.63479 and the FET drain terminal (V2) is biased to 1.5 V. Figure 3.13 illustrates the frequency response of the device to a pressure variation of 1 Pa. The microphone has a flat response of 25 mV/Pa over the frequency range 100 Hz to 1 kHz. The phase is relatively constant over this frequency range also.

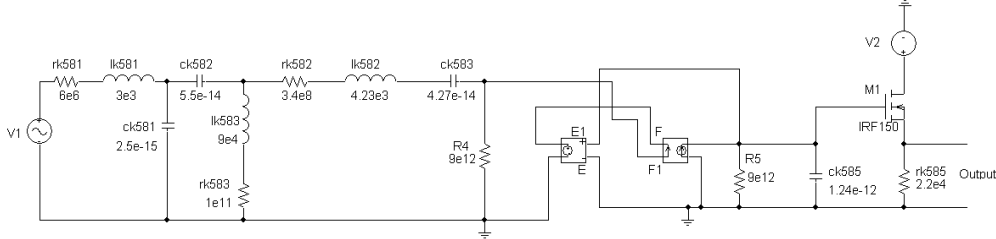


Figure 3.12: Equivalent Circuit for Knowles FG-3629 Microphone

The microphone signal was pre-amplified using the circuit shown in Figure 3.14. Low noise OP-27 operational amplifiers (Analog Devices) were employed. The frequency response of the system is illustrated in Figure 3.13. A constant gain of 200 V/V with a phase shift of -180° is observed in the frequency range 100 Hz to 1 kHz. As shown in 3.13 and 3.15, the frequency responses of the microphone and amplifier circuits are linear (constant) over most of the useful frequency

range for gas cell photoacoustic spectroscopy. This will make interpretation of the results easier as instrumentation effects will be easy to remove.

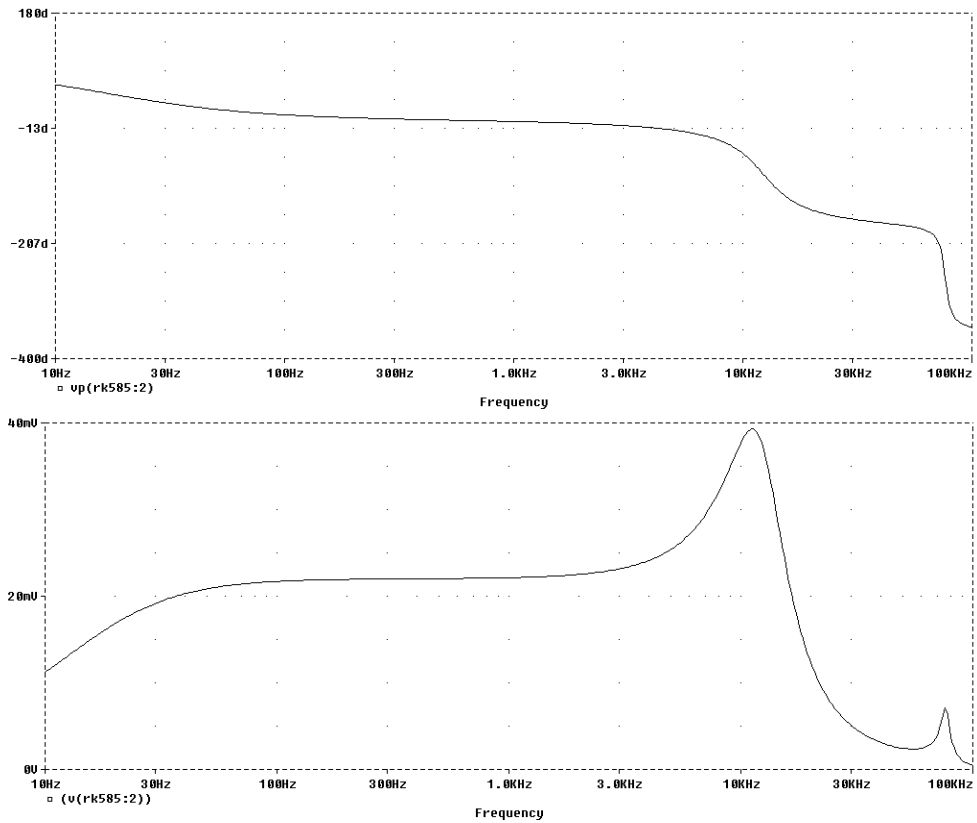


Figure 3.13: Frequency Response of the Knowles FG-3629 Microphone for signal with amplitude 1 Pa: (a) Amplitude vs. Frequency (top) (b) Phase vs. Frequency (bottom)

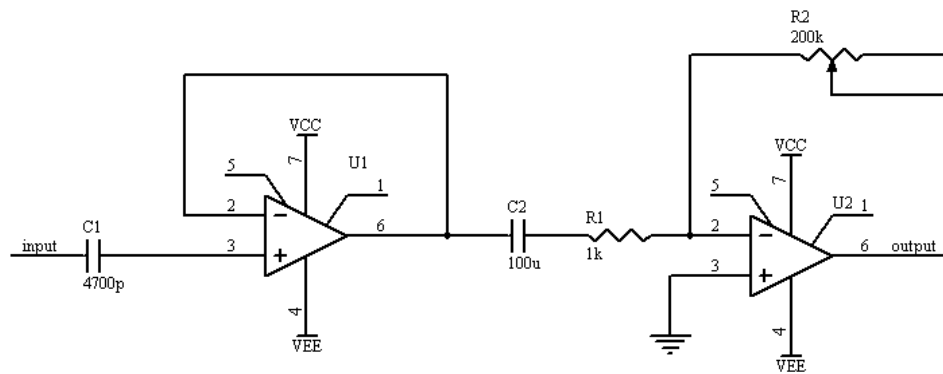


Figure 3.14: Circuit for Microphone Preamplifier.

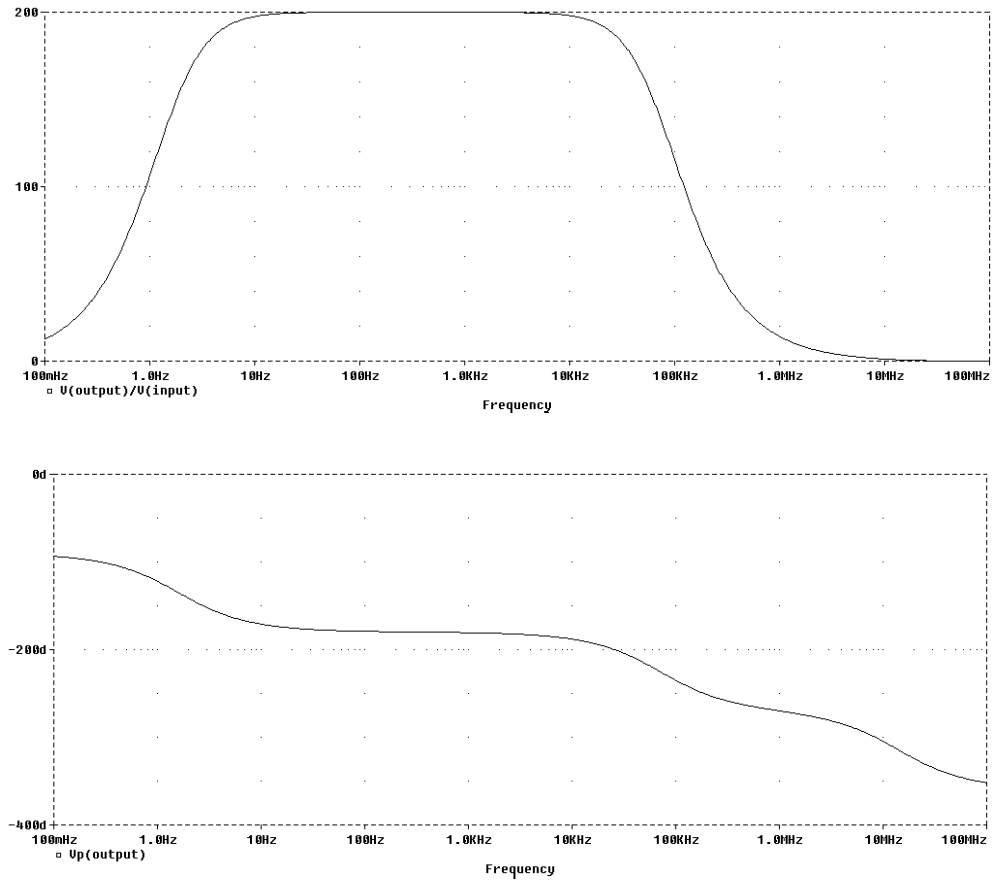


Figure 3.15: Frequency Response of Microphone Preamplifier. (a) Gain [V/V] vs. frequency (top); (b) Phase vs. frequency (bottom)

3.4.4.2 Noise Spectral Densities: Microphone and Pre-amplifier

Simulation of the noise spectral density for the microphone is straightforward in PSPICE. With the exception of the FET all components are passive and PSPICE readily generates the appropriate noise signals. The result is illustrated in Figure 3.16. A noise characteristic similar to IC noise is illustrated. One can determine the RMS noise output voltage from the noise spectral density as follows: [3.15]

$$E_n = \int_0^{\infty} e_n^2(f) df = 15mV_{RMS} \quad (3.13)$$

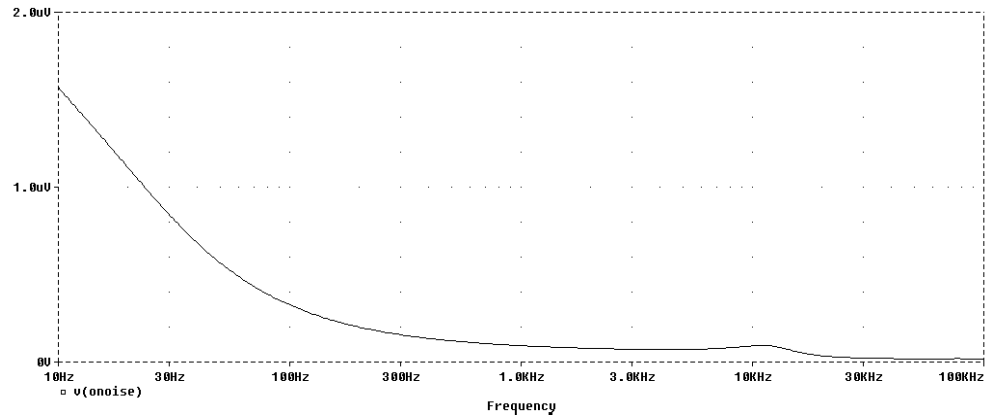


Figure 3.16: Noise Spectral Density e_n [V/Sqrt(Hz)] for Knowles FG-3629 microphone. The y axis label is noise voltage amplitude [mV].

This value is slightly greater than the manufacturer's quoted value of 10 uV or -102 dBV(A). The difference could be easily explained by the manufacturer setting the upper frequency limit in the integral to approximately 10 kHz, the upper end of the audio spectrum.

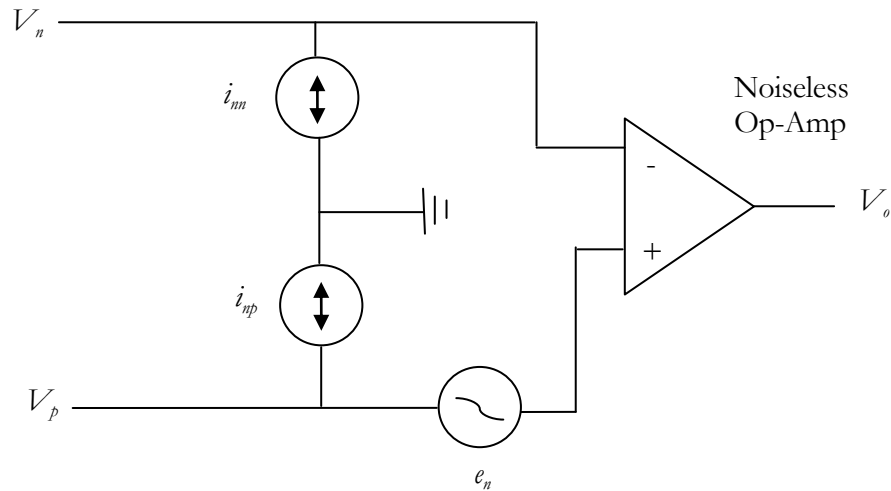


Figure 3.17 Noise model for operational amplifier

Simulation of the noise spectral density for the pre-amplifier and in particular its constituent operational amplifiers is complicated by the fact that PSPICE does not readily include a noise model for the operational amplifier. An equivalent circuit model for a noisy op-amp is used, as shown in Figure 3.17.

The current and voltage noise sources can be generated by appealing to the manner in which PSPICE models diode noise [3.15]:

$$i_d^2 = KF \frac{I_D^{AF}}{f} + 2qI_D = 2qI_D \left(KF \frac{I_D^{AF-1}}{2qf} + 1 \right)$$

where KF and AF are diode parameters, f is the frequency, q is the electric charge and I_D is the DC current flowing through the diode. This is a power density with

noise floor $i_w^2 = 2qI_D$ and corner frequency $f_c = KF \frac{I_D^{AF-1}}{2q}$. By letting $AF = 1$,

we obtain $KF = 2qf_c$ and $I_D = \frac{i_w^2}{2q}$. Thus, the corner frequency and noise floor

can be read from the manufacturer's data sheet and the diode model can be edited to set KF .

A circuit implementation for the noise source i_n can be seen in Figure 3.18. The instance model of the diode is edited to set AF and KF according to the noise corner frequency. The constant current source is set such that a $1pA/\sqrt{Hz}$ noise current is capacitively coupled through C1 into the current controlled current source (CCCS). By setting the gain of the CCCS one can arbitrarily adjust the noise current injected into the system without having to recalculate all the diode parameters. For each noise source present in the system, a separate noise generating circuit must be employed to ensure no correlation between sources. To generate a voltage noise source, the appropriate corner frequency is used and

the CCCS is simply replaced by a current controlled voltage source (CCVS) with the appropriate gain setting.

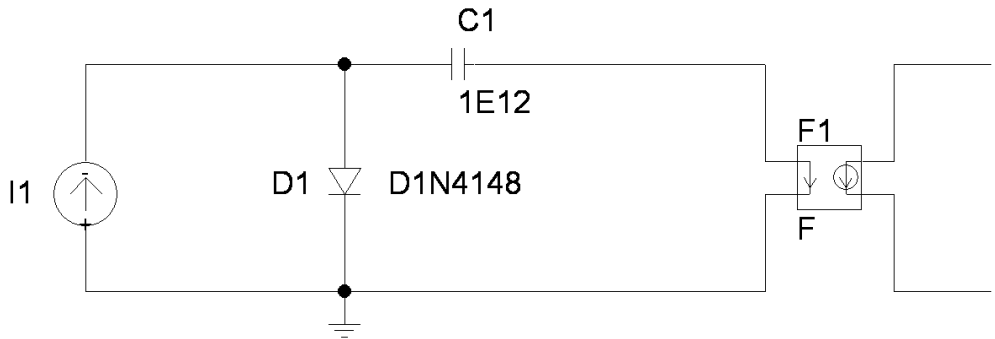


Figure 3.18: PSPICE model to produce op-amp current noise source

The response of an internally compensated noiseless op-amp is dominated, to first order, by one pole in the transfer function [3.15]:

$$T(s) = \frac{a_0}{1 + \frac{s}{2\pi f_a}} \tag{3.15}$$

Thus the noiseless op-amp may be replaced by the ELAPLACE function in PSPICE.

For the OP-27 low-noise op-amps used in the design:

$$e_{nv} = 3nV / \sqrt{Hz} \tag{3.16}$$

$$i_{nv} = 0.4pA / \sqrt{Hz} \tag{3.17}$$

$$f_{ce} = 9 \text{ Hz} \tag{3.18}$$

$$f_a = 250 \text{ Hz} \quad (3.19)$$

$$a_0 = 125 \text{ dB} \quad (3.20)$$

The simulated noise spectral density of the preamplifier circuit of Figure 3.14 is shown in Figure 3.19. Due to the high gain employed in the circuit ($= 200 \text{ V/V}$), the noise spectral density of the amplifier is slightly greater than the microphone. The amplitude of the noise spectral density increases with the circuit gain. One can see that a significant proportion of the noise density is present for $f < 10 \text{ Hz}$. In the future a more judicious amplifier design can be employed to decrease the relative contribution of this noise source by providing a high pass filter with a cut-on frequency of 10 Hz . The RMS output noise, with the input to the amplifier grounded, is [3.15]

$$E_n = \int_0^{\infty} e_n^2(f) df = 394 \mu\text{V}_{RMS} \quad (3.21)$$

For the overall system, the noise from the microphone combines in quadrature with the preamplifier noise and undergoes amplification within the amplifier. The resulting noise spectral density for the system is shown in Figure 3.20. It can be clearly seen that the major contribution to the noise lies in the frequency range for which $f < 10 \text{ Hz}$. This is due to significant contributions from the microphone and amplifier noise sources within this frequency range. The RMS output noise of the system is 3.21 mV . This is equivalent to a peak-to-peak noise voltage of 21.1 mV .

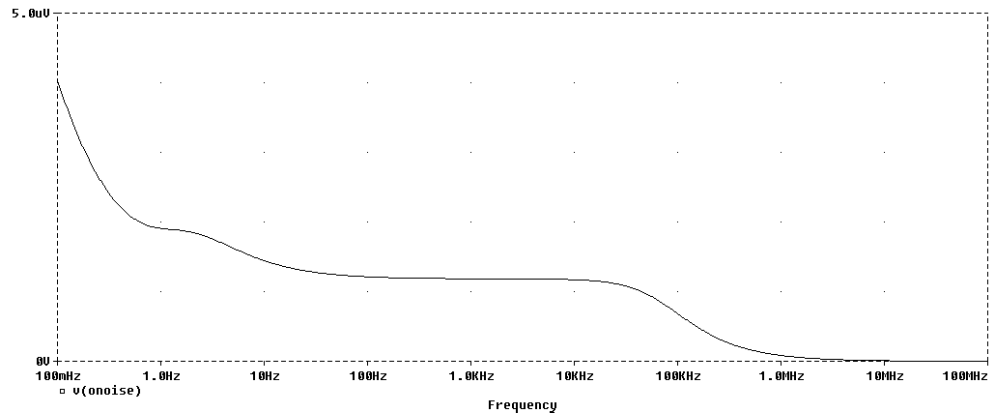


Figure 3.19: Noise spectral density $e_n [V / \sqrt{Hz}]$ of microphone preamplifier. The y axis label is noise amplitude [mV].

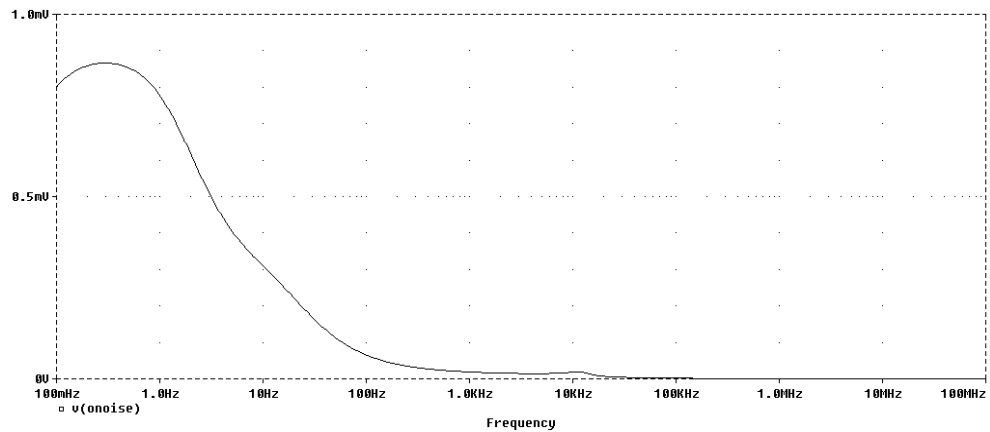


Figure 3.20: Noise spectral density $e_n [V / \sqrt{Hz}]$ of combined microphone preamplifier system. The y axis label is noise amplitude [mV].

3.4.4.3 Lock-in Amplifier Operational Overview

A lock-in amplifier employs phase sensitive detection to measure a signal at a specific frequency and phase. In brief, the experiment is designed so that the signal of interest occurs at a known constant frequency and the lock-in reference frequency is set to match this. The two signals are combined in a phase sensitive detector (multiplier). The output has a component at the sum and difference

frequencies. As the difference between the reference and experiment frequency is designed to be zero, the signal of interest is effectively shifted to 0 Hz or DC. This signal is then passed through a low pass filter. The filter strongly attenuates signals with frequency components outside its pass band. Such signals include the sum frequency generated by the multiplier and all noise signals occurring at frequencies other than the reference frequency. Thus a DC signal proportional to the product of the reference signal and the experimental signal of interest is produced.

The low-pass filter will have some pass band determined by the filter slope and the cut-off frequency. Input signals to the amplifier within the detection bandwidth appear at the output of the device. Therefore if one wishes to increase the signal to noise ratio, one must implement sharper filter slopes with lower cut-off frequencies. As we are dealing with presumably random noise sources (mains hum, for example, being a notable exception), it is more appropriate to discuss the noise equivalent bandwidth (NEB) of the filter rather than the pass band. The NEB and cut-off frequency are primarily determined by the filter time constant τ . When increasing the time constant, the NEB is narrowed at the expense of increasing the time for the filter to charge to its final value. Table 3.4 illustrates the relationship between the filter slope, NEB and the wait time [3.6].

Slope [3.dB/oct]	NEB [3.Hz]	Wait Time [3.s]
6	$1/(4\tau)$	5τ
12	$1/(8\tau)$	7τ
18	$3/(32\tau)$	9τ
24	$5/(64\tau)$	10τ

Table 3.4: Filter slope, NEB and Wait Time for SR830 Lock-in Amplifier

For example, using a time constant of 250 ms, one can easily achieve a NEB of 1 Hz using lock-in detection. To further illustrate this example, imagine that the

experiment was running at 1 kHz and one tried to measure the signal by passing it through a band pass filter centered at 1 kHz with $Q = 100$. A bandwidth of 10 Hz would be passed. Now assuming the noise spectral density is constant (as would be the case for Gaussian noise), the lock-in amplifier would pass ten times less noise compared to the conventional filter, thereby achieving a signal to noise ratio ten times greater than the traditional filter. Referring back to the simulated data in Figure 3.20, one can see from the previous discussion that the lock-in amplifier will only admit a small component of the noise density spectrum. Thus very weak electrical signals arising from the photoacoustic effect, which would be impossible to measure with conventional analogue processing techniques, may be detected with lock-in amplification.

One final aspect of lock-in detection requires explanation before the measurements can be discussed. This is the topic of dynamic reserve. The dynamic reserve defines the maximum permissible strength, which a signal outside the NEB of the lock-in amplifier can possess before it overloads the amplifier. Dynamic reserve is expressed in dB. This concept will be further illustrated by an example. Suppose the NEB of the amplifier is 1 Hz, centered at 120 Hz and the dynamic reserve is set to 60 dB. If a signal outside the NEB, say for example at 130 Hz, has strength greater than 60 dB then the amplifier will be overloaded by the noise source. Signals with strength less than 60 dB will be attenuated and hence will not interfere with the measurement. Please note that at the reference/experiment frequency the dynamic reserve is 0 dB – obviously we do not want to attenuate the signal of interest! The actual dynamic reserve is controlled by the sensitivity of the amplifier. The SR850 DSP lock-in amplifier offers three reserve modes: low noise, normal and high reserve. The relationship between amplifier sensitivity and each of these modes is illustrated in Table 3.5 [3.16]. One should strive to use the minimum amount of reserve possible at all times.

Sensitivity [3.mV]	Low Noise [3.dB]	Normal [3.dB]	High Reserve [3.dB]
1000	0	0	0
500	6	6	6
200	4	14	14
100	0	10	20
50	6	16	25
20	4	24	34
10	0	20	40
5	6	26	46
2	4	34	54
1	10	40	60
0.5	16	46	66
0.2	24	54	74
0.1	30	60	80
0.05	36	66	86
0.02	44	74	94
0.01	50	80	100
0.005	56	86	106
0.002	64	94	114
0.001	70	100	120
0.0005	76	106	126
0.0002	84	114	134
0.0001	90	120	140
0.00005	96	126	146
0.00002	104	134	154
0.00001	110	140	160
0.000005	116	146	166
0.000002	124	154	174

Table 3.5: Dynamic Reserve Settings for SR830 DSP Lock-in Amplifier

3.4.4.4 *Noise Measurement in the photoacoustic signal conditioning system*

The SR830 DSP lock-in amplifier can measure the noise spectral density associated with an input signal using a technique known as mean average deviation (MAD). The signal is decomposed into its orthogonal components on the Argand plane. Using an initial value of the mean computed from an initial data subset, a running average of the absolute value of the deviation of subsequent data elements from the mean is computed. This is the mean average deviation. If the noise is Gaussian in nature, the MAD result is related to the

RMS noise by a constant factor. To ensure good statistical convergence it is advisable to wait at least eighty time constants before reading the noise values.

The experimental setup used to measure the noise spectral density within the photoacoustic spectroscopy system is shown in 3.21. A voltage was sent from the lock-in amplifier auxiliary output to the voltage-controlled oscillator (VCO) in the chopper controller. This set the desired modulation frequency. The reference frequency output from the chopper controller was then fed back to the lock-in amplifier as its reference. This militated against any internal drift in the chopper controller. During the measurement, all photoacoustic system components were turned on. The laser light was blocked from entering the photoacoustic cell. In this manner, the measurement was susceptible to all noise sources present under normal user conditions without exciting the sample.

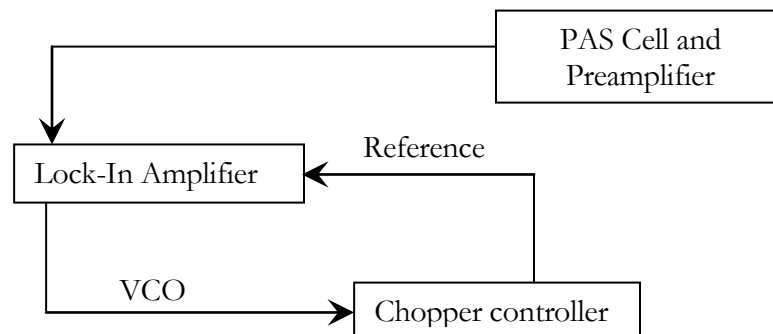


Figure 3.21: Experimental Set up used to measure noise spectral density.

The result of the measurement is shown in Figure 3.22. One can see that the measured result agrees quite closely with the simulated result shown in Figure 3.20. In this measurement the lock-in amplifier was configured with a time constant $t = 30$ ms, filter slope 24 dB/oct, sensitivity $s = 5$ mV and low noise dynamic reserve. The signal was AC coupled with the shield floating. The synchronous filter and line filters were turned off. According to Table 3.4, this

implied a NEB = 2.6 Hz and a wait time of 300 ms. According to Table 3.5, 6 dB of dynamic reserve is used. The simulated RMS output noise in the frequency interval $10 < f < 600$ Hz is 1.55 mV compared to the measured value of 2.45 mV. When the peak-to-peak noise voltage was measured on a standard analogue oscilloscope a value of ~ 20 mV was recorded. The oscilloscope was DC coupled and thus did not attenuate the signal over the frequency range of interest. This is in excellent agreement with the simulated value of 21.1 mV. Thus the noise in the signal conditioning system is close to the prediction. The entire noise component within the photoacoustic system has been taken into the consideration and been modeled properly.

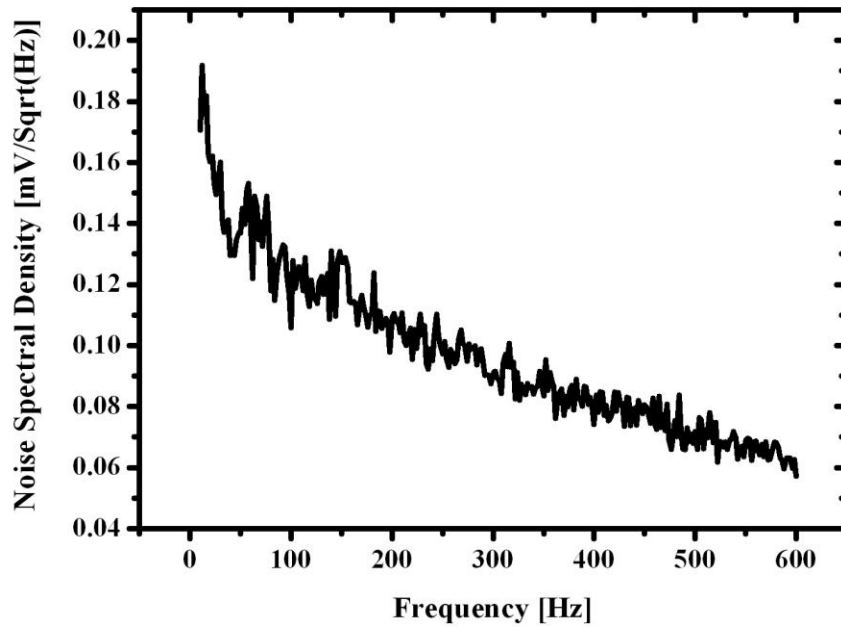


Figure 3.22: Noise Spectral Density of PAPAS system measured using SR830 DSP lock-in amplifier

In our exploration of the noise dynamics in the system, several other measurements were performed that will be briefly summarized here. The BNC cable connecting the preamplifier to the lock-in amplifier was disconnected at the preamplifier and the measurement was repeated. In this situation the cable acted as an antenna and the noise spectral density reflected this with large peaks at the odd harmonics of 50 Hz. A similar result was observed when the cable was connected to the preamplifier when powered off. Effectively, the cable behaved as if it were still floating and acted as an antenna. Similar data was recorded when the cable was disconnected.

Following this measurement, the preamplifier and the remaining constituent components were powered up in sequence with noise spectra recorded at each step. No significant deviation from the result shown in Figure 3.22 was observed at any stage. Thus, noise due to mains hum was removed once the BNC shield was properly grounded and the remaining potential noise sources did not couple into the system to any observable extent.

For the measurement in Figure 3.22, quite a low dynamic reserve of 6 dB was employed. This translates into a relative attenuation factor for signals far outside the NEB of the low pass filter of 2. The measurement was repeated with reserves of 16 dB and 25 dB. No difference was observed in the recorded noise spectra implying that the external noise sources were weak in amplitude. This further substantiates the observations made in the previous paragraph.

2.3.1

Controlling software design LabView®

The full potential of the optical and electrical equipment previously described can only be harnessed by placing the entire system under the control of a personal computer. All the equipment in the system is controlled directly or indirectly via

the IEEE 488.2 GPIB or RS-232 communication standards. Conventional GPIB provides a modular robust approach for interfacing up to fifteen devices on a single data bus. Unlike RS-232, where parameters such as baud rate, parity and the number of stop bits have to be known, any device adhering to the GPIB standard may be connected to the bus with little or no knowledge of its communication requirements. In conjunction, RS-232 does not readily permit simultaneous communication with several devices without the use of sophisticated hardware or software routines.

GPIB devices communicate with each other by sending device-dependent messages and interface messages through the interface system. Device-dependent messages, commonly known as data messages, contain device specific information such as programming instructions that control its operation. Interface messages are primarily concerned with bus management. Interface messages perform functions such as initializing the bus and addressing devices.

GPIB devices may be categorized as *talkers*, *listeners* and *controllers*. Listeners are devices that may receive data transmitted by a talker. For example, the lock-in amplifier acts as a talker (transmitting data to the computer), a listener (acquiring data from the microphone via the preamplifier) and also a controller (sending the commands to the optical chopper controller and the laser diode current drive to set the optical modulation frequency). A PCI card (GPIB card) installed in the control PC, which is employed as the controller in this application, manages the flow of information on the bus by sending commands to all the devices, including the monochromator, motorized filter wheel. The Ethernet card in the PC was also used to send the positioning commands to the motorized stages using the RS-232 interface as another controller.

List of the selected VI written in the PAS & PAM system	
Ref No	VI name
Function	
	Monochromator and Filter wheel control
M1	MonoSendMessage.vi
M2	MonoReceiveMessage.vi
M3	MonoGetLamda.vi
M4	MonoGetGrating.vi
M5	MonoGoLamda.vi
M6	MonoGoGrating.vi
M7	MonoGetFilter.vi
M8	MonoGoFilter.vi
M9	MonoFindGratingLamda.vi
M10	MonoFindFilterLamda.vi
M11	MonoShutter.vi
	Lock-in Amplifier Control
L1	LockInSendMessage.vi
L2	LockInReceiveMessage.vi
L3	LockInAmplifierSetUp.vi
L4	LockInReadDisplay.vi
L5	LockInReadAuxIn.vi
	X-Y Stage Control
S1	GetPosition.vi
S2	MoveAbsolute.vi
S3	MoveRelative.vi
	Photoacoustic Application
PAS1	EnergyScan_mult_lock_call_130106.vi
PAM1	ICPAM_160407.vi
Freq1	Laser_freq_scan_030305.vi
P1	PA_Power_250405.vi
	Function
	Send a command to monochromator
	Receive a string from the monochromator
	Finds the current wavelength
	Finds the current grating no
	Change to a specific wavelength
	Change to a specific grating
	Find the current filter no
	Change to a specific filter no
	Determine the grating no for a specific wavelength
	Determine the filter no for a specific wavelength
	Open and close the shutter
	Send a message to the lock-in amplifier
	Receive a string from the amplifier
	Configures the amplifier
	Reads a specified display (Amplitude & Phase, eg.)
	Read a speified analogue auxiliary input
	Receive the postion info of the motorized stage
	Move the stage to a absolute position
	Move the stage by a relative position
	Photoacoustic Spectrometer with fixed frequency
	Photoacoustic Microscopy with fixed frequency
	Frequency dependence measurement of PA siagnal
	Light source power spectrum measurement with power meter

Table 3.6: List of the selected VI written for the PAS and PAM systems.

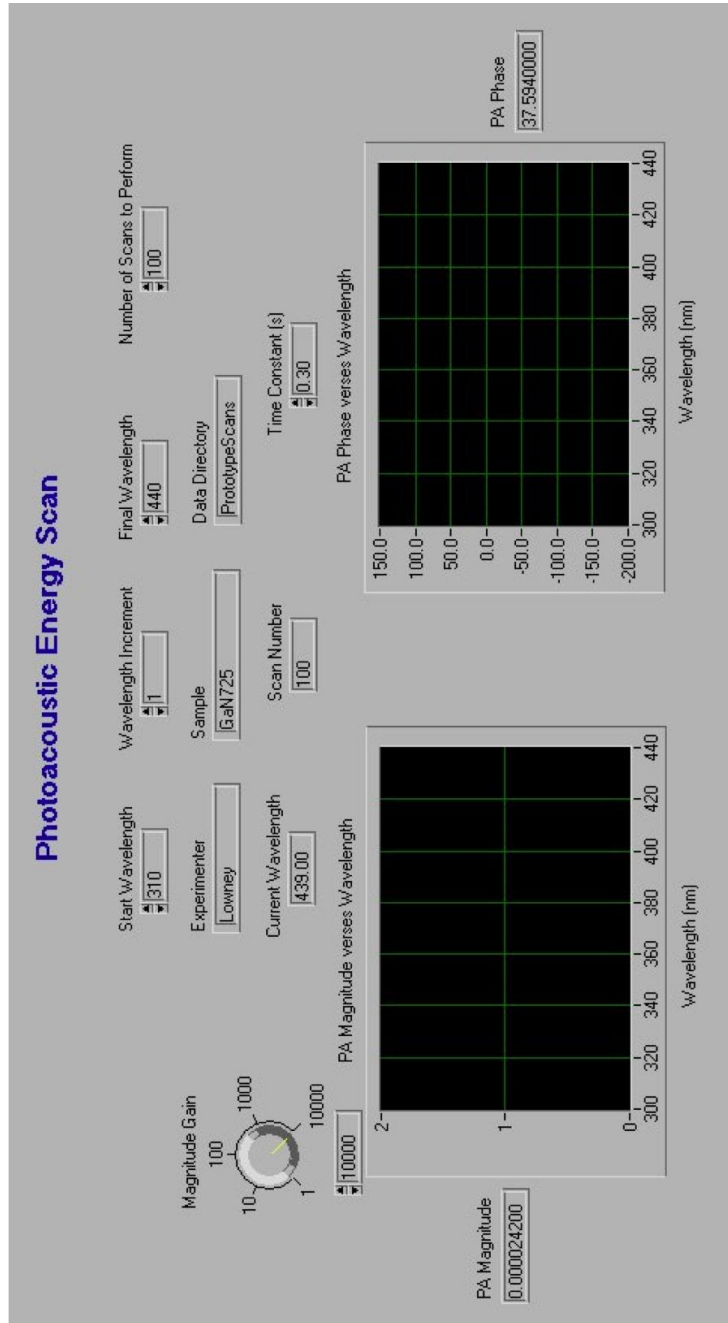


Figure 3.23: The Graphical User Interface for the Photoacoustic Spectroscopie

Devices are usually connected via a shielded 24-conductor cable with both a plug and receptacle connector at each end. The bus uses negative logic with standard TTL levels. In order to achieve the high data transmission rates, nominally 1.5 Mbytes/s when using a PCI controller, the physical distance between devices is limited as follows: The maximum separation between any two devices should be less than 4 m and the average device separation must not be greater than 2 m over the entire bus. The total cable length must not exceed 20 m. This will clearly not be a problem for the photoacoustic spectrometer and microscope implemented in this thesis.

One of the ancillary benefits of using the IEEE 488.2 GPIB standard is that the hardware companies have developed sophisticated high-level application development tools, which provide application specific user interfaces to enable engineers to build their own GPIB systems. LabView®, a product of National Instrument Inc, is such graphical program development environment. The LabView® programs, known as VIs (virtual instruments), can mimic the actual device operation with which they are communicating. It consists of interactive user interfaces, data flow diagrams and icon connections that allow the VIs to be called from higher level VIs.

The VIs designed for the photoacoustic systems fall into three functional categories: hardware control, data acquisition and graphic user interface (GUI). Groups of VIs have been written to control individual hardware components within the photoacoustic system, as shown in Table 3.6.

In this work, LabView® VIs are implemented for the two major photoacoustic applications. One is for the Photoacoustic Spectrometer, whose user interface is shown in Figure 3.23 and the VI operational flow chart is shown in Figure 3.24. Prior to starting the VI, the user enters the start wavelength, end wavelength and

wavelength increment for the scan. The user specifies the number of scans that are to be performed and also provides the details of where the data is to be stored. The VI is then started and proceeds according to the flowchart.

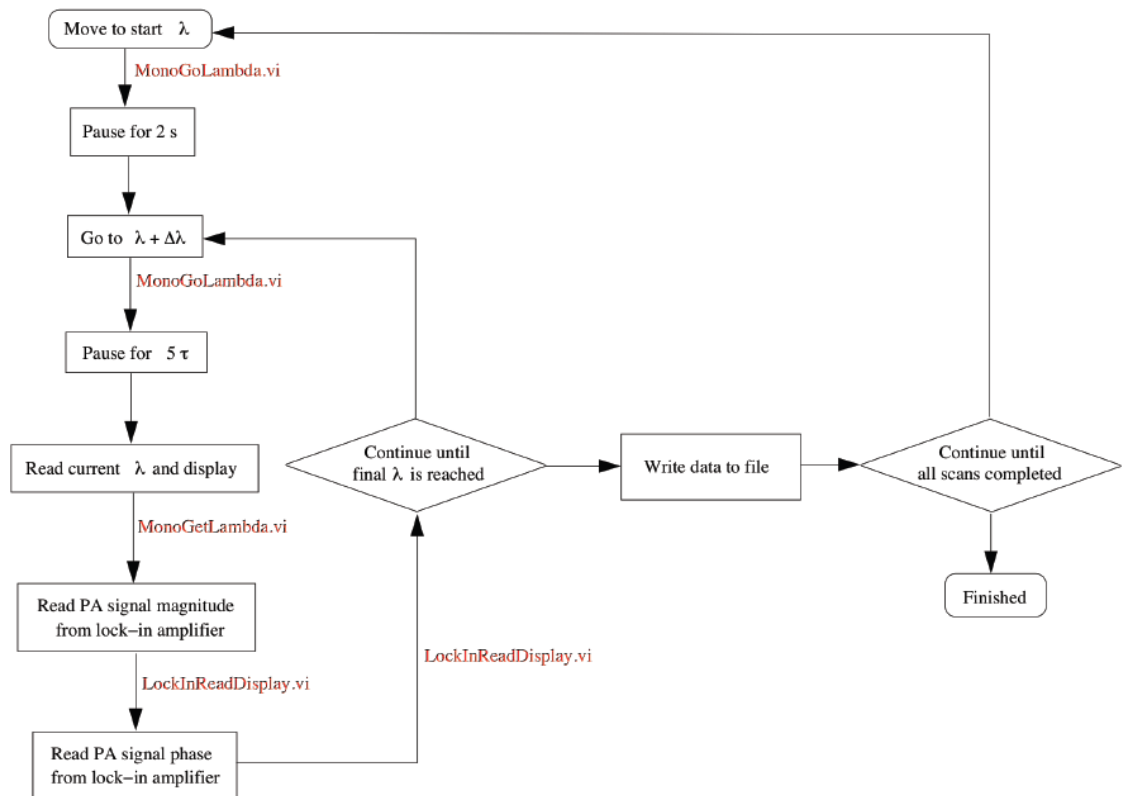


Figure 3.24: Flowchart of the operation of the Photoacoustic Spectroscopy VI as listed in Table 8 (Energy_muti_lock_call_130106)

The other major application VI is for the Photoacoustic Microscopy, whose user interface is shown in Figure 3.25. With this VI, using the stage control knobs on the GUI and featuring webcam video data from the sample surface, the user can navigate across the sample and find the area of interest for photoacoustic mapping. Once the user enters the start and end positions for the X-Y motorized stage and the spatial resolution, the laser scan will start automatically. The measured PA amplitude and phase will be displayed in real-time on-screen for each horizontal scan and the 3D mapping results will be plotted when the

measurements are completed. The zoom functionality can be activated during the measurement; the resolution of the image can be adjusted and becomes effective immediately.

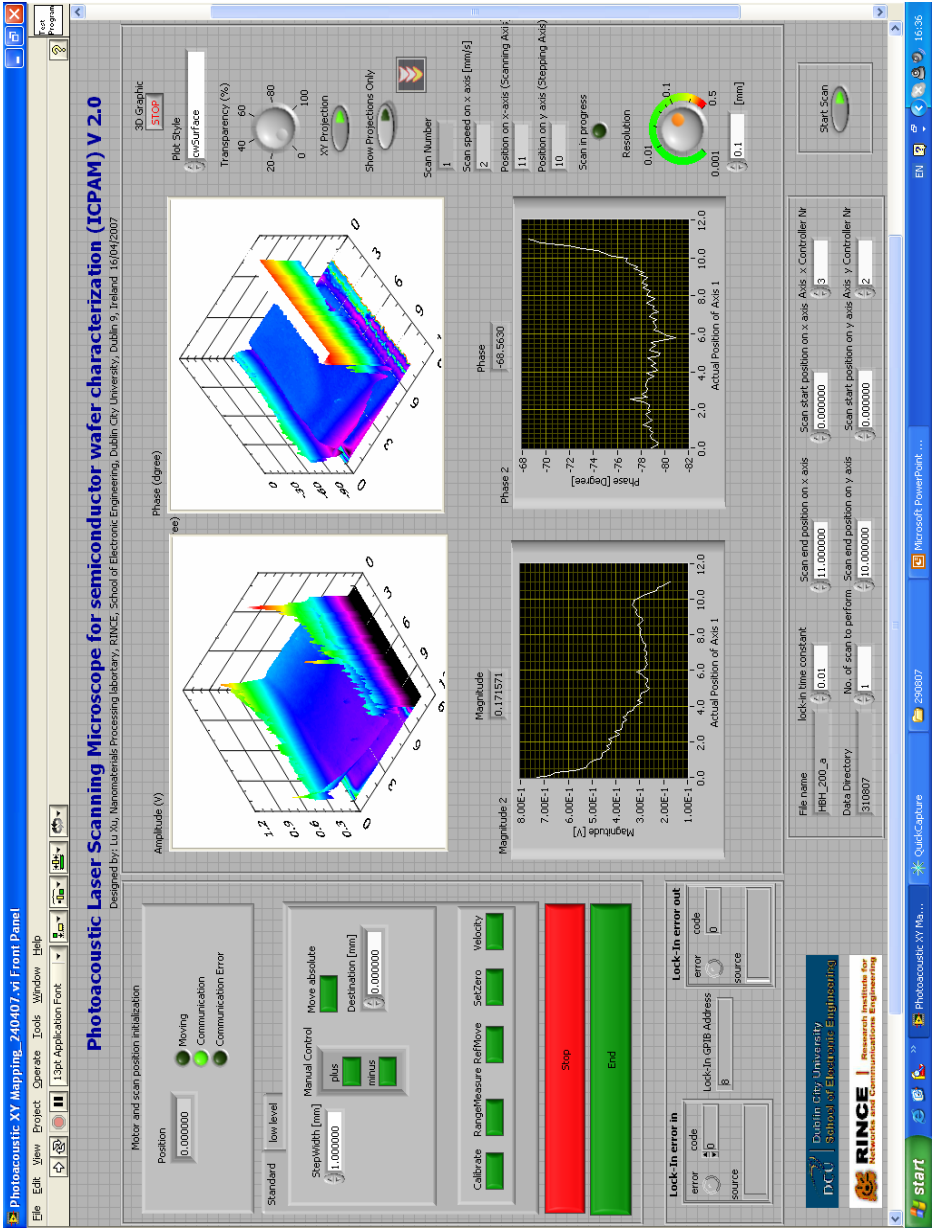


Figure 3.25: The User interface for Photoacoustic Microscope

Chapter 4

PHOTOACOUSTIC SYSTEM CALIBRATION AND VERIFICATION

4. Photoacoustic System Calibration and Verification

In the previous chapter, the design criteria for a high resolution and fully computerized photoacoustic spectrometer and microscope are outlined. The mechanical drawing of the PA cell, the layout of the electronic sensing components, and the LabView® software control system are described. In this chapter, the calibration results are presented to demonstrate the effectiveness of the PA system. Carbon black powder, which is widely used as a PA reference sample, will be analyzed intensively.

With a gas-microphone photoacoustic configuration, the amplitude and the phase of the detected acoustic signal are dependent on numerous system parameters. These include the light source intensity, the PA cell geometry, the coupling gas in the cell, the backing material below the sample and the microphone sensitivity. Therefore, it is necessary to calibrate the photoacoustic system before starting the real measurements.

4.1. Light source intensity linearity calibration

For this calibration, a He-Ne gas laser (632.8 nm) is used as a light source. The maximum power output from this laser is about 17 mW. A neutral density (ND) filter is placed in front of the laser output port to change the light source intensity. A glass slide is placed inside the optical beam path and 4% of the light power is redirected to an optical power meter to estimate the light source intensity after the ND filter. A mechanical optical chopper is used to modulate the light source at a specified frequency. The laser, which has a low divergence angle, is focused

through a lens tube, as shown in Figure 4.1, to periodically heat up the samples within the PA cell.

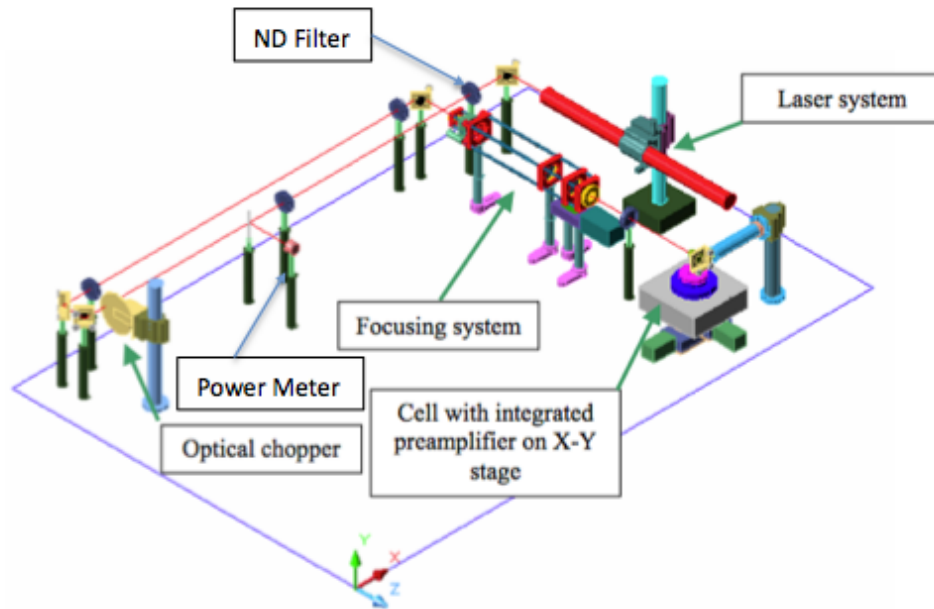


Figure 4.1: The experimental hardware layout for PA System with He-Ne laser light source. Not to scale.

The carbon black powder is placed into the PA cell as a reference sample in this test case. The typical thermal conductivity of this material can be found in the literature [4.1], where density $\rho = 836 \text{ kg/m}^3$, thermal conductivity $k = 60 \text{ mW/m}^2\text{K}$ and specific heat $C = 650 \text{ J/kg}^{\circ}\text{K}$. As seen in Figure 4.2, within the testing frequency range from 100 Hz to 500 Hz, the thermal diffusion length of this material varies from 18.5 μm to 8.5 μm . This is much smaller than the carbon black powder thickness within the PA cell, which is approx 500 μm .

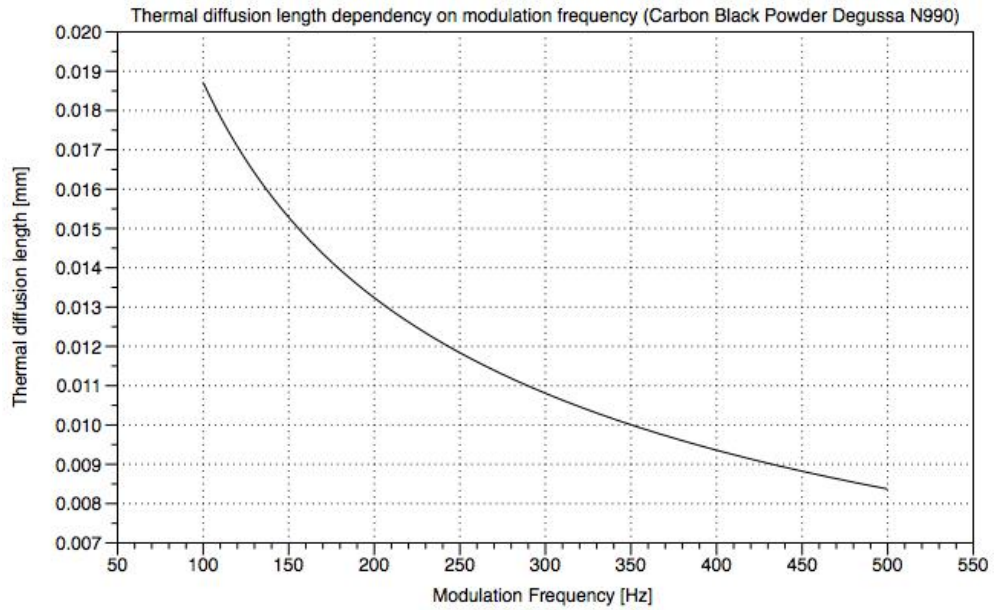


Figure 4.2: Thermal diffusion length dependence on the modulation frequency (Carbon Black powder, Degussa N990)

By changing the laser position on the ND filter, the light source intensity of the PA system can be reduced from 16.5 mW to 12.625 mW, 7.625 mW, 3.75 mW, 2.45 mW, 1.2425mW, 0.595 mW and 0.22 mW, respectively. As shown in Figure 4.3, the average PA amplitude is linearly proportional to the light source intensity. As shown in Figure 4.4, the PA signal intensity decreases as the modulation frequency increases. In contrast, the PA phase is independent of the light source intensity, presented in Figure 4.5. A linear fit of PA Phase vs. $\log(f)$, where f is the modulation frequency of the optical chopper, remains almost the same across the frequency range for different value of light source intensity.

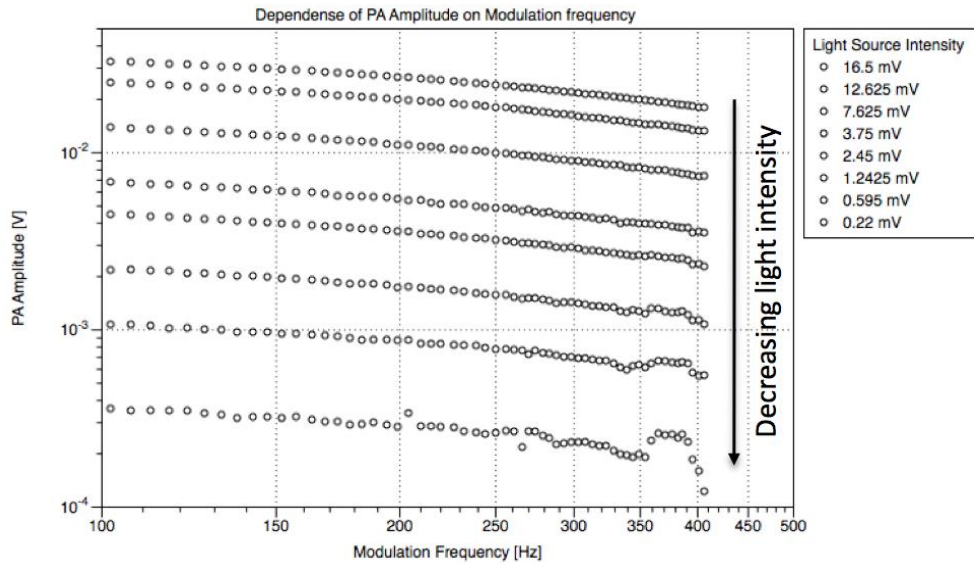


Figure 4.3: Dependence of PA Amplitude on Modulation Frequency for decreasing light source intensity. (Sample: Carbon Black Powder)

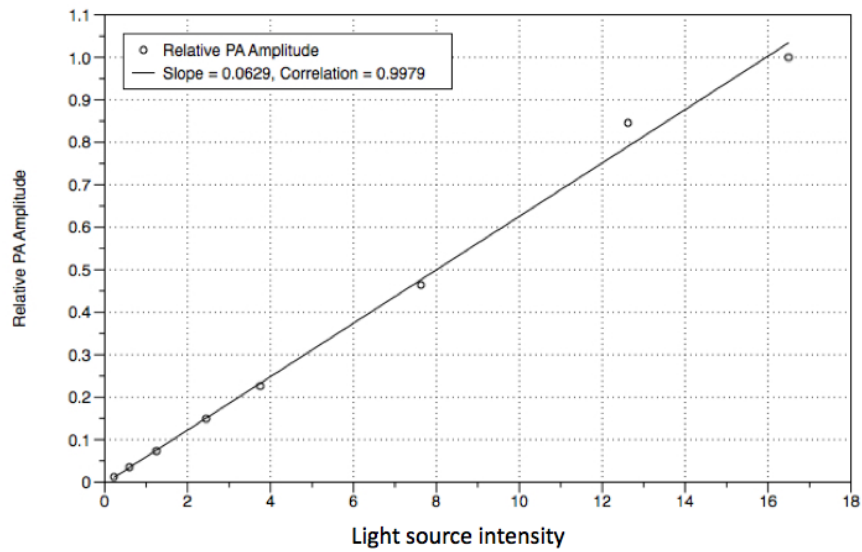


Figure 4.4: Dependence of PA Amplitude on Modulation Frequency for varying light source intensity. (Sample: Carbon Black Powder)

These results are consistent with the predictions of R-G theory, given in the previous chapter. According to equations 2.35 and 2.28, for an optically opaque and thermally thick sample, ($\mu_s < l_s, \mu_s > \mu_\beta$ and $\mu_\beta < l_s$), such as carbon black powder, the PA signal dependence on the modulation frequency can be described by the equation below:

$$Q = \frac{(1-j)}{2a_g} \left(\frac{\mu_s}{k_s} \right) \frac{\gamma P_0 I_0}{2\sqrt{2}T_0 l_g} \quad [4.1]$$

where Q is the complex envelope of the sinusoidal pressure variation, a_g is the thermal diffusion coefficient in the gas, and μ_s is the thermal diffusion length in the sample. As confirmed by Figure 4.4, the PA amplitude is linearly proportional to the light source intensity (I_0). As confirmed by Figure 4.3, the PA Amplitude decreases as the modulation frequency increases.

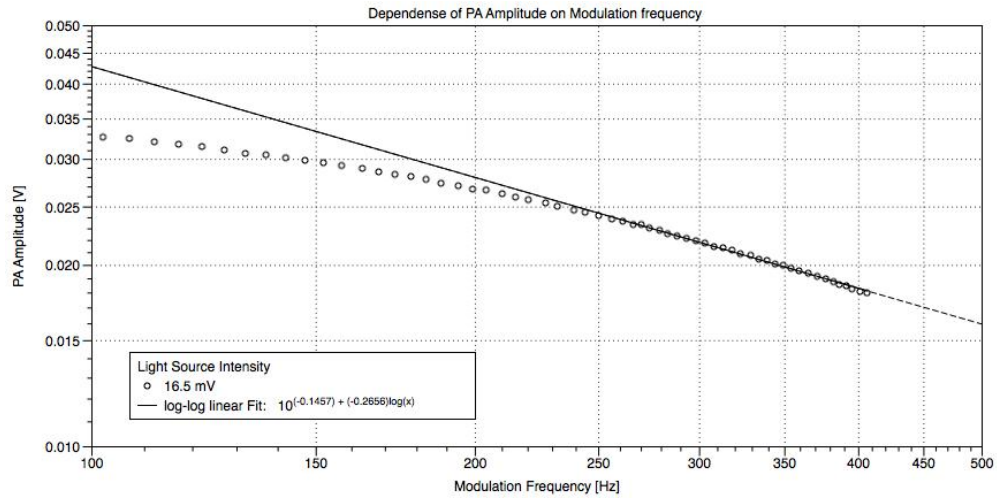


Figure 4.6: The linear function fit of the PA amplitude dependency on $\log(f)$ (Sample: Carbon Black Powder with light source power of 16.5 mW)

According to equation 4.1, for carbon black powder, the PA amplitude should be linearly proportional to ω^{-1} and the PA phase should remain constant at - 45 degrees across the modulation frequencies. However, this is not exactly the case here. As shown in Figure 4.6, the PA amplitude only starts to be linearly proportional to $\log(f)$ or ω^{-1} at frequencies above approx 200 Hz. The experimental data obtained at lower frequencies are not as predicted by the R-G theory.

This is due to the fact that the R-G theory is based on the assumption of a one-dimensional photoacoustic cell, where the thermal wave only diffuses along the vertical z-axis. This assumption is valid only when the laser spot radius, a , is much bigger than the thermal diffusion length μ_s , and the thermal diffusion along the x and y-axes can be neglected. In the test case here, a lens tube has been used to focus the low divergence He-Ne laser beam to a small spot size, which is about 10 μm in diameter. As shown in Figure 4.2, the higher the modulation frequency, the smaller the thermal diffusion length when compared to the laser spot size.

Therefore, the better will be the fit to the frequency dependency using the R-G theory.

Since it is difficult to measure exactly the thickness of the carbon black powder within the PA cell and also difficult to make an evenly distributed homogeneous testing sample from a powder material, the detailed frequency dependency characterization of the PA cell will be discussed later using standard semiconductor wafer samples.

4.2. SR850 lock-in amplifier calibration

The PA system developed here uses a Stanford Research SR850 lock-in amplifier to detect and measure very small PA signals. It uses a technique known as phase-sensitive detection (PSD) to single out the component of a signal at a specific reference frequency and phase.

As shown in Figure 4.7, the SR830 multiplies the incoming signal with two pure sine waves at the reference frequency simultaneously. These two sine waves have a fixed 90-degree phase shift with respect to each other. The product of these two yields a DC output signal, which is proportional to the components of the signal, whose frequency is exactly the same as the reference frequency. The multiplier result or the output of PSD can be described as:

$$\begin{aligned}
 V_{PSD,1} &= V_{sig} V_L \sin(\omega_r t + \theta_{sig}) \sin(\omega_L t + \theta_{ref}) \\
 &= 1/2 V_{sig} V_L \cos([\omega_r - \omega_L]t + \theta_{sig} - \theta_{ref}) - 1/2 V_{sig} V_L \cos([\omega_r + \omega_L]t + \theta_{sig} + \theta_{ref})
 \end{aligned}
 \tag{4.2}$$

where V_{sig} , θ_{sig} , V_L and θ_{ref} are the amplitudes and the phases for the input signal and the lock-in reference respectively. ω_L is the reference modulation frequency. $V_{PSD,1}$ is the output voltage of phase sensitive detector.

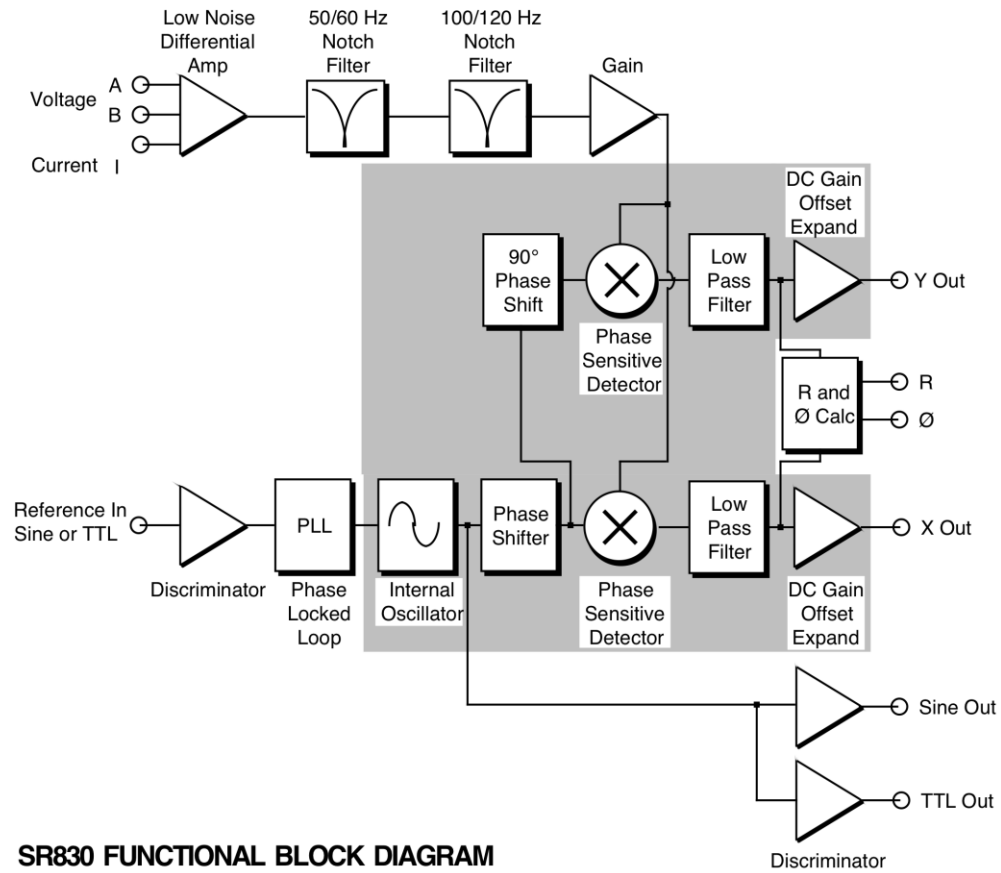


Figure 4.7: SR830 Lock-in Amplifier Functional Block Diagram [4.2]

As shown in Figure 4.7, there are 2 PSDs within the SR830 lock-in amplifier, denoted as $V_{PSD,1}$ and $V_{PSD,2}$. The low pass filter, which follows two multipliers, removes the signal components at all other frequencies except for $\omega_L = \omega_r$. This DC filter is what makes the lock-in such a narrow band detector.

The filtered PSD output will be

$$V_{PSD,1} = \frac{1}{2} V_{sig} V_L \cos(\theta_{sig} - \theta_{ref}) \quad (4.3)$$

This is a DC signal, which is proportional to the signal amplitude and the phase difference between the signal and the lock-in reference. This phase dependence can be eliminated by the 2nd PSD, using a lock-in reference whose phase is shifted by 90 degrees. The filtered PSD output is

$$\begin{aligned} V_{PSD,2} &= \frac{1}{2} V_{sig} V_L \cos(\theta_{sig} - (\theta_{ref} + \frac{\pi}{2})) \\ &= \frac{1}{2} V_{sig} V_L \sin(\theta_{sig} - \theta_{ref}) \end{aligned} \quad (4.4)$$

Combining these two PSD outputs, wherein one is proportional to $\cos(\theta_{sig} - \theta_{ref})$ and the other is proportional to $\sin(\theta_{sig} - \theta_{ref})$, the signal magnitude, R , can be calculated without the phase dependence:

$$R = \sqrt{V_{PSD,1}^2 + V_{PSD,2}^2} = \frac{1}{\sqrt{2}} V_{sig} V_L \quad (4.5)$$

In addition, the phase between the signal and lock in reference can be described as

$$\theta = \tan^{-1}\left(\frac{V_{PSD,2}}{V_{PSD,1}}\right) \quad (4.6)$$

Since a mechanical chopper or a TTL signal from the SR830 internal function generator has been used to modulate the light source intensity in the PA system, the PA signal is shown as a square wave in the oscilloscope. Similar to any other lock-in amplifier, the SR830 multiplies the input signal with pure sine waves and measures the individual Fourier components of the signal.

For example, if the PA signal generated in the cell is a 2V peak-to-peak square wave (PA amplitude = 1 V), it can be expressed as

$$S(t) = 1.273 \sin(\omega t) + 0.4244 \sin(3\omega t) + 0.2546 \sin(5\omega t) + \dots \quad (4.7)$$

where $\omega = 2\pi f$ and f is the frequency of the PA signal. The signal detected by the lock-in amplifier is the 1st Fourier component only and the output PA amplitude will 1.27V, which is slightly bigger than the real PA amplitude generated in the cell.

I	PA Amp.	t1	t2	NEB [Hz]
16.5	0.0296	0.03	0.15	8.333333333
12.625	0.0222	0.03	0.15	8.333333333
7.625	0.0124	0.1	0.5	2.5
3.75	0.00606	0.1	0.5	2.5
2.45	0.004	1	5	0.25
1.2425	0.00196	3	15	0.083333333
0.595	0.00095	10	50	0.025
0.22	0.000319	30	150	0.008333333

Notes:

I Light intensity [mW]
 PA Amplitude @ 152 Hz
PA Amp. [V]
t1 Time Constant [s]
t2 Wait time [s]

Table 4.1: The lock-in amplifier settings used to detect the PA signal generated by varied light source intensities. The SR830 has been configured to wait 5τ before collecting the signal.

The corresponding noise equivalent bandwidth (NEB) can be calculated as $\frac{1}{4\tau}$.

With the same input signal, the narrower the bandwidth, the higher is the signal to noise ratio (SNR). Traditionally, the lock-in amplifier sets the low pass filter

bandwidth by setting the time constant (τ). By increasing the time constant (τ) within the SR830 configuration, the output becomes steadier and reproducibility of the PA system is improved. However, the SR830 typically requires waiting for about 5τ for the low pass filter (a single RC filter) to settle to its final value. The time constant (τ) not only determines the repeatability performance of the tool but also reflects the speed of the output response. As shown in Table 4.1, while decreasing the light source intensity, the PA signal amplitude decreases linearly. To keep the same signal to noise ratio (SNR), the time constant has to be increased from 30 ms to 30 s to reduce the noise equivalent bandwidth (NEB). The throughput of the PA system decreases from 150 ms per data point to 150 s per data point. To get a reasonable throughput performance for a metrology tool, it is necessary to keep the calculation time less than 0.5 s per data point and the PA amplitude is required to be more than 6 mV as shown in Table 4.1.

4.3. Arc lamp light source spectrum calibration

Carbon black powder has a constant optical absorption coefficient across all wavelengths. [1.3] Therefore, the PA amplitude spectrum of the carbon black powder should follow exactly the same trend as the arc lamp power spectrum, which has been used as the light source in the PA spectroscopy system.

As shown in Figures 4.8 and 4.9, within the detection range of the silicon photodiode (200 nm – 1100 nm), the power spectrum detected by the optical power meter looks very similar comparing to the one collected by the PA system. The main differences between those two spectra are as following

- i. PA spectrum has much greater detection range, which extends up to 2400 nm. The power spectrum obtained by silicon diode can only extend to ~1000 nm, which is limited to the silicon bandgap energy.

- ii. The resolution of the power spectrum obtained by PA system is much smaller comparing to the one captured by silicon diode. This was due to the LabView® code setting used at the time for data collection in this experiment.

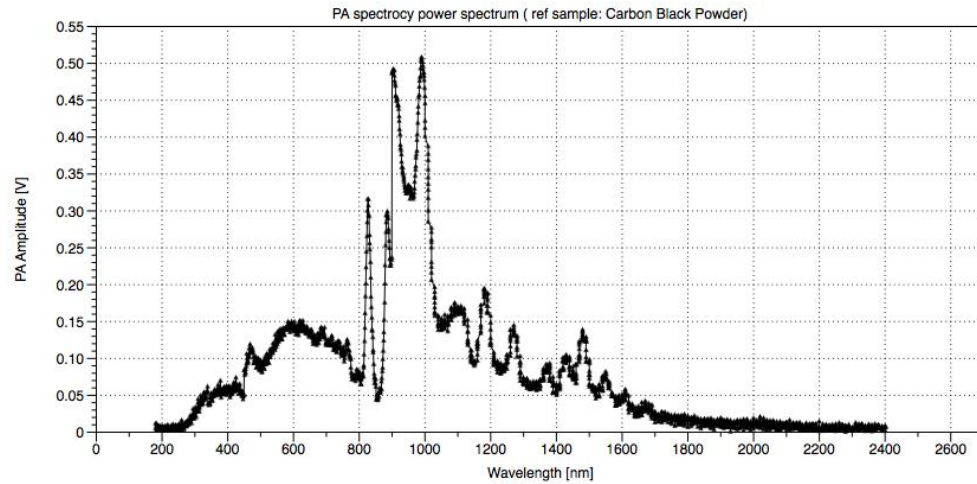


Figure 4.8. PA spectroscopy power spectrum measured using a PA cell filled with carbon back powder reference samples. The lock-in amplifier setting is time constant = 30 ms, AC coupling, sensitivity = 500 mV, modulation frequency = 43Hz, Ground, High reserve, Negative edge triggering.

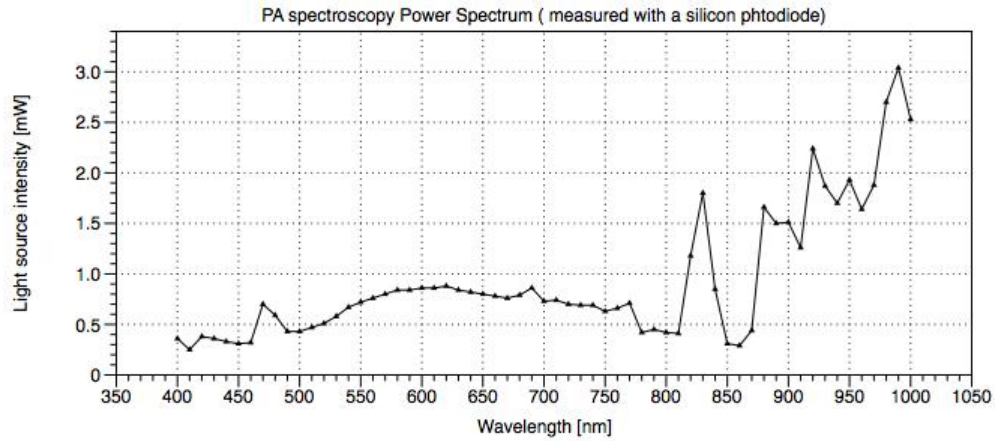


Figure 4.9: PA spectroscopy power spectrum measured using SM05PD2A Silicon photodiode.

The performance specification of the SM05PD2A photodiode can be found in the literature [4.3], where the spectral response is in the 200 -1100 nm wavelength range, active area is 0.8 mm^2 , rise time ($R_L = 50\Omega$) is 1ns (@20V bias), fall time ($R_L = 50\Omega$) is 1ns (@20V bias), NEB (@ 440 nm) is $5 \times 10^{-14} \text{ W}/\sqrt{\text{Hz}}$ (@ 20 V bias), dark current is 2.5 nA max. (@20V), damage threshold (CW) is $100 \text{ W}/\text{cm}^2$, maximum bias voltage is 25 V, damage threshold (10 ns pulse) is $500 \text{ mJ}/\text{cm}^2$.

4.4. Impact of focus offset between the PA sample position and the focal point

As discussed previously, it is necessary to maximize the total light source intensity to improve the signal to noise ratio of the PA system. However, with the same light source, the PA amplitude will not increase by focusing the same laser to a smaller spot size.

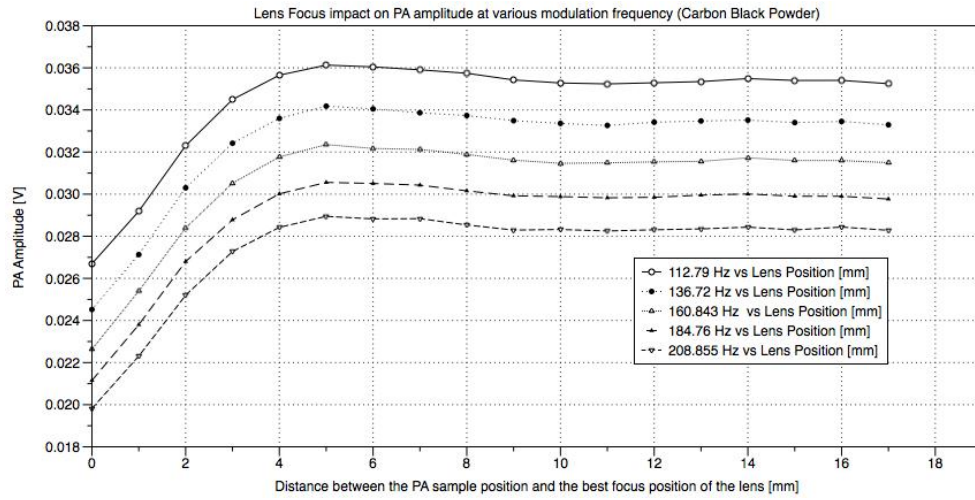


Figure 4.10: Impact of lens focal position (before focus) on the PA amplitude at various modulation frequencies (PA sample: Carbon Black Powder, PA light source: He-Ne laser. Experimental settings: time constant = 300 ms, sensitivity = 50 mV, AC Coupling, Float.

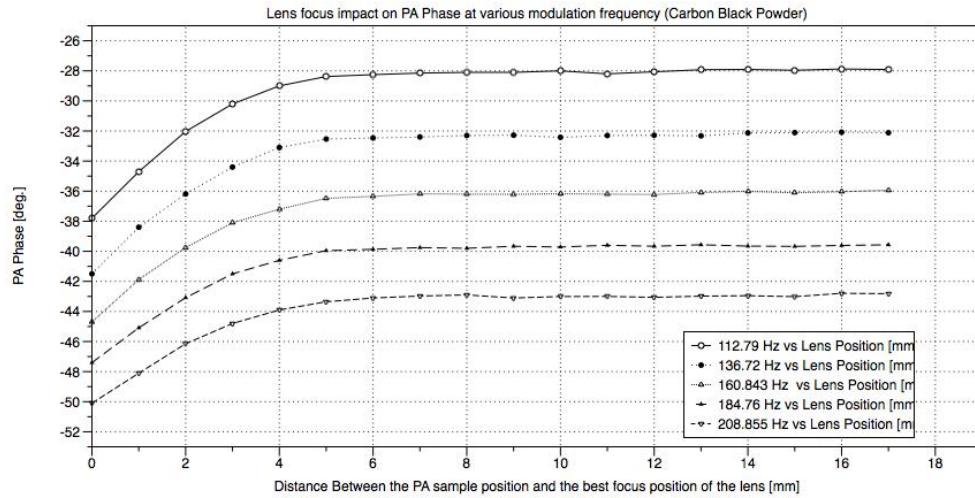


Figure 4.11: Impact of lens focal position (before focus) on the PA phase at various modulation frequencies (PA sample: Carbon Black Powder, PA light source: He-Ne laser. Experimental settings: time constant = 300 ms, sensitivity = 50 mV, AC Coupling, Float).

A He-Ne laser is used as the light source in this test. This low divergence laser has been collimated at first and then focused by a FL 152.4 mm lens into the PA cell. The minimum laser spot size, which can be measured at the focal point, is about 50 μm . By positioning the PA cell a certain distance away from the focal point, the laser beam spot size on the carbon black sample surface can be adjusted. The bigger the focus offset, the larger the laser spot size. The PA frequency dependence has been recorded with different focus offsets. The thermal diffusion length μ for the modulation frequencies used in this test varies from 13 μm to 20 μm , as calculated in Figure 4.2.

When the PA sample is placed at the focal plane of the lens, the laser spot size is of the same order as the thermal diffusion length. The thermal wave generated by the optical absorption at the sample surface diffuses not only in the z-axis but also along the x-y plane. In this case, the PA amplitude and phase depends not only on the modulation frequency ω , but also on the radius, a , of the laser spot

As shown in Figure 4.10, the PA Amplitude reaches its minimum value at the focal point and it increases as the laser spot size increases. When the focus offset is about 5 mm, the PA amplitude reaches its maximum value and becomes insensitive to the laser spot size.

In summary, to maximize the PA signal, it is necessary to increase the total light intensity, however it is not necessary to focus the laser beam as tight as possible. The possible reason for this phenomenon could be related to the thermoelastic deformation on the sample surface and three-dimensional thermal diffusion process, as was previously investigated by Opsal and Rosencwaig. [4.4] It is worthwhile to investigate this issue in future research to optimize the optical settings for the prototype photoacoustic system.

4.5. Impact of the coupling gas within the cell: Air vs. Helium Gas

As described in chapter 2, when the thermal diffusion length in the gas medium is smaller than the PA cell height, the PA signal is dependent on the coupling gas properties.

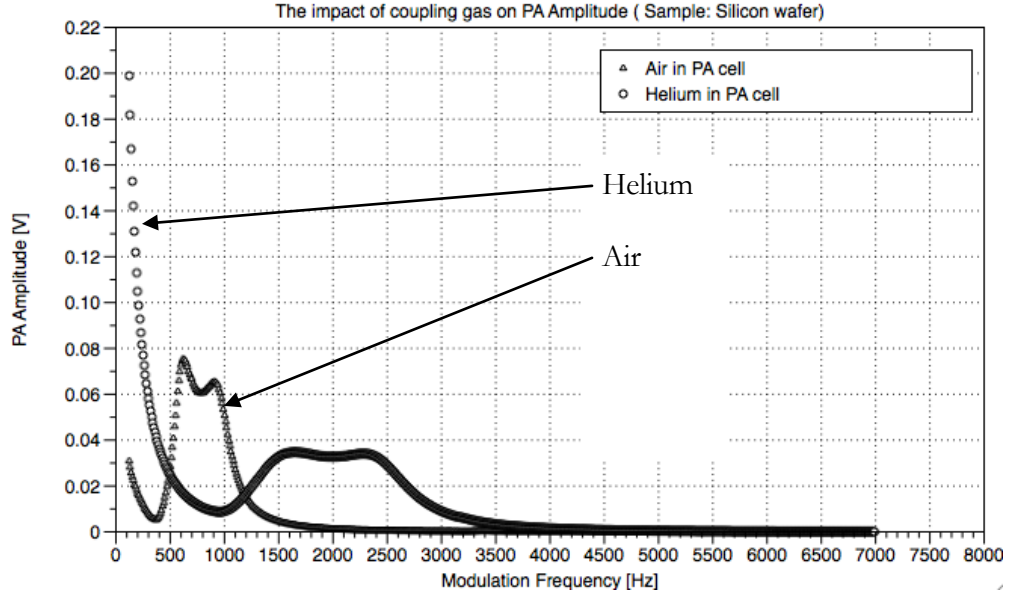


Figure 4.12: The impact of the coupling gas on PA Amplitude: Helium Gas vs. Air (sample: Silicon wafers with polished surface towards the laser beam, Lock-in Amplifier settings: time constant = 300 ms, Lock-in sensitivity = 200 mV, one active microphone only in the PA cell)

According to equation 2.26c, 2.9, 2.10 and 2.11, without considering the acoustic resonance effect within in the PA cell, the PA signal dependence on the coupling gas is described by:

$$\begin{aligned}
 \therefore \partial P(t) &= \frac{2\pi\mu_g}{l_g} \gamma \frac{P_0}{T_0} \\
 \therefore \mu &= \frac{1}{a} = \sqrt{\frac{2\alpha}{\omega}} \\
 \therefore \alpha &= \frac{k}{\rho C} \\
 \therefore \mu &= \sqrt{\frac{2k}{\omega\rho C}} \\
 \therefore \partial P(t) &= \frac{2\pi}{l_g} \gamma \frac{P_0}{T_0} \sqrt{\frac{2k_g}{\omega\rho_g C_g}} \propto \frac{2\pi}{l_g} \gamma \frac{P_0}{T_0} \sqrt{\frac{2k_g}{\rho_g C_g}}
 \end{aligned} \tag{4.8}$$

where l_g is the height of PA cell ($= 9\text{mm}$, as noted in chapter 3), P_0 is the ambient pressure and T_0 is the ambient temperature. γ , k_g , ρ_g and C_g are defined in chapter 2.

The material properties of air and helium gas are found as follows [4.13, 4.14]:

$$\begin{aligned}
 \gamma_{helium} &= 1.66 \\
 \gamma_{air} &= 1.4 \\
 k_{helium} &= 0.1513(W / mK) \\
 k_{air} &= 0.0257(W / mK) \\
 \rho_{helium} &= 178.6(g / m^3) \\
 \rho_{air} &= 1208(g / m^3) \\
 C_{helium} &= 5.1932(Ws / gK) \\
 C_{air} &= 1.012(Ws / gK)
 \end{aligned} \tag{4.9}$$

The PA signal intensity ratio given by the use of the two different coupling gases can be calculated as

$$\frac{\partial P(t)_{Helium}}{\partial P(t)_{Air}} = 3.3029 \tag{4.10}$$

Thus, theoretically, while using helium gas as the coupling gas in the PA cell, the PA Amplitude will increase by a factor of 3. The PA amplitude ratio is independent of the modulation frequency. Changing the coupling gas has no impact on the PA phase.

However, this conclusion can only be valid in the lower frequency range of the experimental data. As shown in Figure 4.12, when one uses air as the coupling gas in the PA cell, the signal amplitude shows a broad peak in the range from 600-900 Hz. This peak is related to acoustic resonance, whose frequency is

determined by the PA cell geometry and the coupling gas therein. For a cylindrical tube, which is closed at one end, the acoustic resonance frequency is given by [4.6]

$$f = \frac{n\nu}{4(L+0.4d)} \quad (4.11)$$

where n is an odd number (1, 3, 5,...), ν is the speed of sound (Helium Gas: 972 m/s, Air: 343 m/s), L is the length of the tube or the height of the PA cell (9 mm, given in chapter 3), d is the cross-sectional diameter of the tube or PA cell (16 mm, given in chapter 3). For an open PA cell without a window, the resonance frequency is estimated to be 4375Hz and 1239Hz for helium or air coupling gas, respectively.

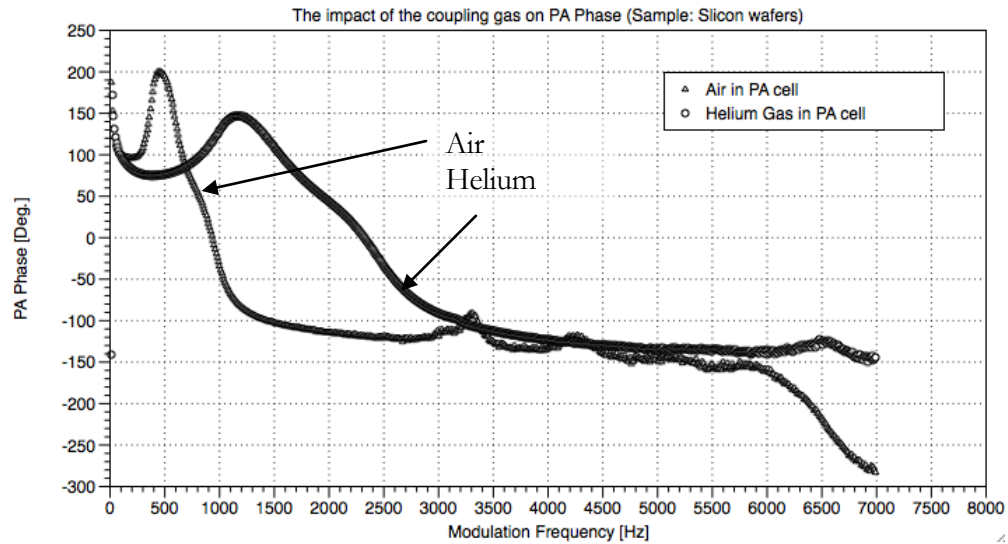


Figure 4.14: The impact of the coupling gas on PA Phase: Helium Gas vs. Air (sample: Silicon wafers with polished surface towards the laser beam, Lock-in Amplifier Settings: time constant = 300 ms, Lock-in sensitivity = 200 mV, one active microphone only in the PA cell)

The resonance frequency of the PA cell is proportional to the sound velocity within the coupling gas. This is consistent with the experimental data. The acoustic resonance peak within the PA cell, while using Helium coupling gas, is 700 Hz and 1980 Hz, as shown in Figure 4.12. The resonance frequency is increased by a factor of 2.83, compared to the situation with air coupling. This value is exactly the same as the ratio of the speed of sound in helium to that in air. Presented in Figure 4.14, the frequency dependence for PA phase also shows different peak positions depending on which coupling gas is used. One is located at ~ 500 Hz and another is at ~ 1200 Hz.

The difference between the calculated and measured resonance frequencies is due to the fact that the PA cell is actually closed at both ends during the measurements and the shape of the enclosed volume is more like a disk rather

than a tube. Therefore end corrections need to be applied to the acoustic model to obtain a more accurate estimation.

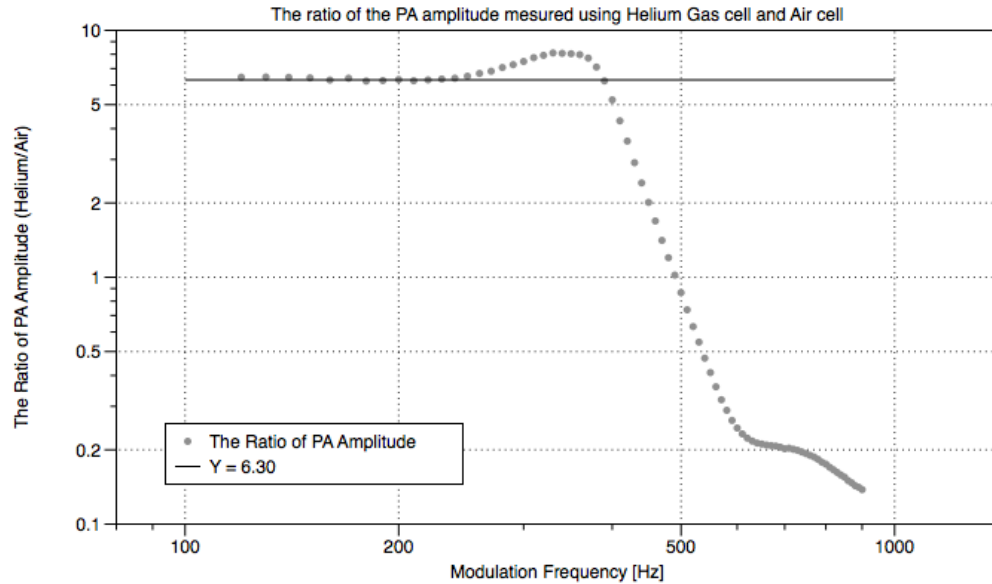


Figure 4.15: PA amplitude ratio for measurements taken using Helium Gas vs. air. (Sample: Silicon wafers with polished surface towards the laser beam, Lock-in Amplifier Settings: time constant = 300 ms, Lock-in sensitivity = 200 mV, one active microphone only in the PA cell)

For certain photoacoustic applications when the frequency response of the PA signal is analyzed, e.g. to estimate the thermal properties of semiconductor materials, it is essential to remove these acoustic resonance effects.

As shown in Figure 4.15, when the modulation frequency is below 220 Hz, the PA Amplitude ratio (i.e. He vs. air coupling) remains constant, as predicted by the photoacoustic theory. However, for higher modulation frequencies, the acoustic resonance effect cannot be neglected. It is worth noted here that the measured PA signal ratio between the PA cell with helium coupling and air is higher than the estimated value, given by equation 4.10. It needs further investigation for the future research.

As shown in Figure 4.12, the working frequency range without the resonance effect can reach up to 220 Hz for the air-filled PA cell and up to 900 Hz for the PA cell filled by Helium gas. To analyze the frequency response of the PA signal outside this range, an extra calibration needs to be performed. This analysis is presented in section 4.6.

For some PA applications, e.g. when the PA signal is collected at a fixed frequency, such as for PA spectroscopy and PA microscopy imaging, the acoustic resonance effect can be ignored. According to Figures 4.12, 4.13 and 4.14, when the modulation frequency is below 500 Hz or above 1200 Hz, it is preferable to use helium as the coupling gas, in order to provide larger PA amplitudes and better SNR performance.

4.6. Impact of the acoustic resonance of the PA cell

As shown in Figure 4.15, the ratio of PA amplitude measured by helium gas cell and air cell is not a constant in the higher frequency. This is not consistent with conclusion as predicted by equation 4.13. It indicates that, the acoustic resonance effect cannot be neglected, when analyzing the PA amplitude dependence on frequency. When using air as the coupling gas, the PA signal is dominated by the acoustic resonance effect in the frequency range from 300 Hz to 3000Hz. This applies equally to all sample types, including data taken in this study for bare silicon wafers or multi-layer structures, such as silicon substrate with thin copper capping layers and etc.

The PA cell geometry and the coupling gas therein determine the shape of this acoustic resonance peak. Two main types of acoustic resonance can occur in a PA cell. One originates from the cylindrical shape of the PA cell itself, which has been discussed previously. The other is the Helmholtz resonance effect, originated from both the PA cell and the closed air volume in front of each

microphone. The best treatment found in the literature on the theory of the Helmholtz resonator is by Rayleigh. [4.5] For the case of a resonator with no external openings to the atmosphere, Rayleigh arrived at a resonant frequency of

$$2\pi f = v \sqrt{\frac{(\frac{1}{V_1} + \frac{1}{V_2})\sigma}{L + \frac{1}{2}(\pi\sigma)^{1/2}}} \quad (4.12)$$

where v is the speed of the sound, σ is the cross-sectional area of tube connecting the PA cell and microphone, L is the length of said tube, V_1 is the volume of the PA cell and V_2 is the volume of the air space in front of the microphone. The schematic of a typical Helmholtz resonator is presented in Figure 4.16

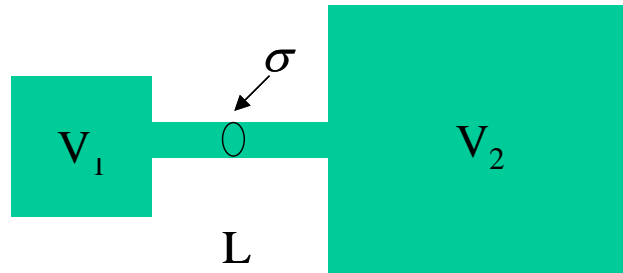


Figure 4.16: The schematic of a typical Helmholtz resonator

Trope gives a small modification to this Helmholtz resonance equation. [4.6] For higher modulation frequencies, an adiabatic sound velocity needs to be used, i.e.

$$v_a = \sqrt{\gamma P / \rho} \quad (4.13)$$

For lower modulation frequencies, an isothermal sound velocity needs to be used given by

$$v_i = \sqrt{P / \rho} \quad (4.14)$$

where P is the gas pressure, ρ is the gas density and γ is the adiabatic index of the gas.

An awareness of the existence of acoustic resonance can help experimenters to design a PA cell in which the resonance only occurs outside the frequency range of interest. By increasing the cross-sectional area of the connecting tube between the PA cell and microphone, the Helmholtz resonance can be placed at a higher frequency.

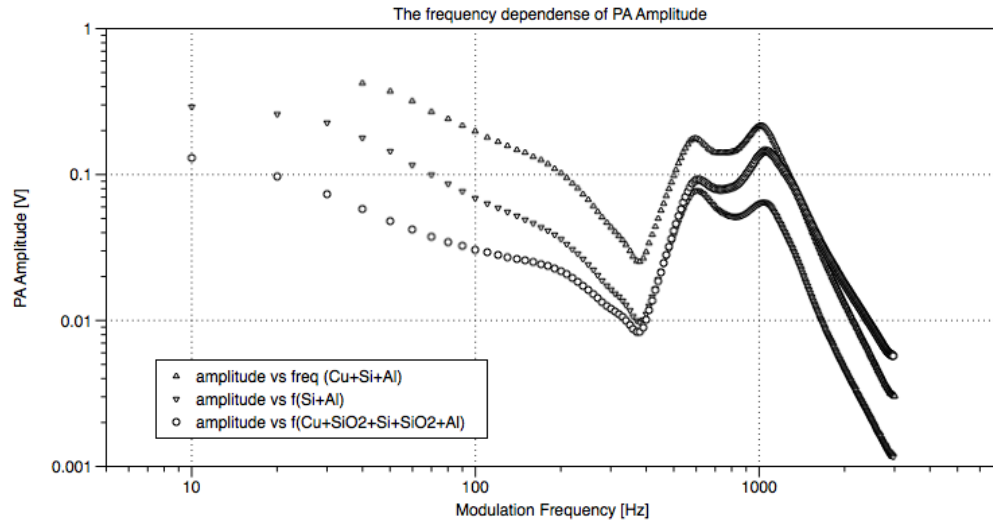


Figure 4.17: The frequency dependence of the PA amplitude. (Light source: NIR laser diode with 808 nm wavelength; Lock-in amplifier settings: time constant = 300 ms, sensitivity = 500 mV; Sample 1: bare silicon wafer with a thin copper layer coated on the top surface, Sample 2: bare silicon wafer, Sample 3: Bare silicon wafer with SiO₂ layers deposited on both side of the wafer and a thin copper layer coated on the top surface, all PA samples have been placed on the Aluminium backing material during the measurements)

The acoustic resonance effect can be a nuisance when analyzing the frequency dependence of the PA signal in order to estimate the thermal properties of a sample. However, this effect can be eliminated using a reference sample.

By way of example, we used a bare silicon wafer as the reference sample and the IR laser ($\lambda = 808 \text{ nm}$) as the PA light source. Under these conditions, the sample is optically opaque. According to equation 2.34, the observed PA signal (S) should exhibit a modulation frequency dependence of $S = Af^{-1}$ in the lower frequency range. [4.7-4.11] However, at higher frequencies, when the acoustic wavelength is comparable with the length of the gas column in the PA cell or when the cell is operating near its resonance frequency, the assumption of the adiabatic condition throughout the cell is no longer valid.

When using higher modulation frequencies, not only acoustic resonance but also sample surface vibration needs to be considered when analyzing the PA signal. McDonald and Wetsel provided a generalized theory to include the acoustic resonance in the PA modelling. In comparison to the R-G theory described in Chapter 2, the McDonald-Wetsel theory takes both thermal expansion and the thermal elastic pressure wave into consideration and replaces the acoustic piston with a composite piston. [4.12]

When amplitude modulated monochromatic light energy is absorbed, periodic heating is induced within the sample and a thermal wave is created in the sample. In addition, owing to the thermo-elasticity effect, pressure waves are formed and propagate towards the bottom and top sample surfaces. Superposition of these waves at the sample surface gives rise to a surface motion, which then serves as a boundary condition for the acoustic waves in the gas. The acoustic piston is now superimposed on the mechanical surface motion induced by the internal sample pressure variations. The resulting “composite piston” as defined by McDonald and Wetsel, produces the pressure variation in the gas detected by the microphone. This effect is much more significant at higher frequencies.

According to [4.12], at the lower modulation frequencies, when $\mu_s \gg l_p$, there is no difference between R-G theory and the McDonald-Wetsel theory. The photoacoustic signal $P_g(x)$ is linearly proportional to $\frac{1}{\omega}$ for both thermally thin and thermally thick samples. However, at the higher frequencies, the surface vibrations cannot be neglected.

For a silicon substrate, the optical absorption coefficient is $\sim 606\text{cm}^{-1}$ at $\lambda = 808$ nm, the optical penetration depth is 16.5 μm at that wavelength, the thermal conductivity is $1.3\text{Wcm}^{-1}\text{K}^{-1}$ and the thermal diffusivity is $0.8\text{cm}^2/\text{s}$. [4.15] The

thermal diffusion length will decrease from 713 μm to 92 μm , as one increase the modulation frequency from 50 Hz to 3000 Hz.

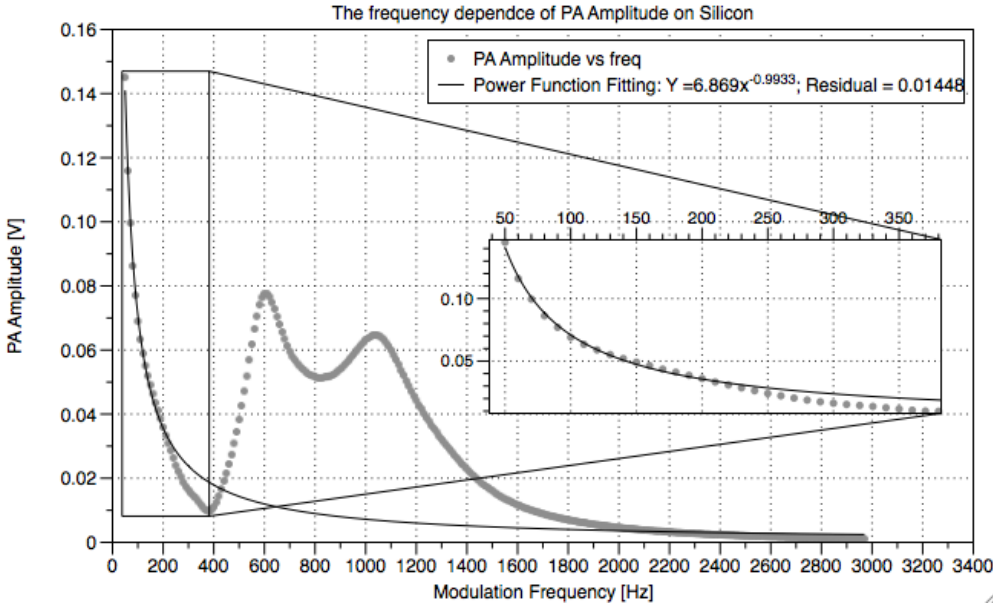


Figure 4.18: The frequency dependence of the PA amplitude measured for a bare silicon wafer. Inset: the power function fit at lower frequencies. (Light source: NIR laser diode with 808 nm wavelength; Lock-in amplifier settings: time constant = 300 ms, sensitivity = 500 mV)

As shown in Figure 4.18, a power function has been used to fit the PA amplitude data taken on a bare silicon wafer in the lower frequency range of 50-220 Hz. The fitting result shows that the frequency dependence of the PA amplitude varies as $S = Af^n$, where $n = -0.9933$. This result is consistent with the prediction given by the photoacoustic theory ($n = -1$). It is a direct confirmation that the design of PA system, illustrated in Chapter 3, is correct and is producing physically reasonable datasets.

Assuming that a fitted power function can be used to describe the PA Amplitude at higher frequencies, the PA amplitude enhancement factor can be calculated by

dividing the measured experimental curve by the fitted power function. As shown in Figure 4.17 and 4.18, the photoacoustic amplitude shows 2 resonance peaks, centered at 600 Hz and 1050 Hz.

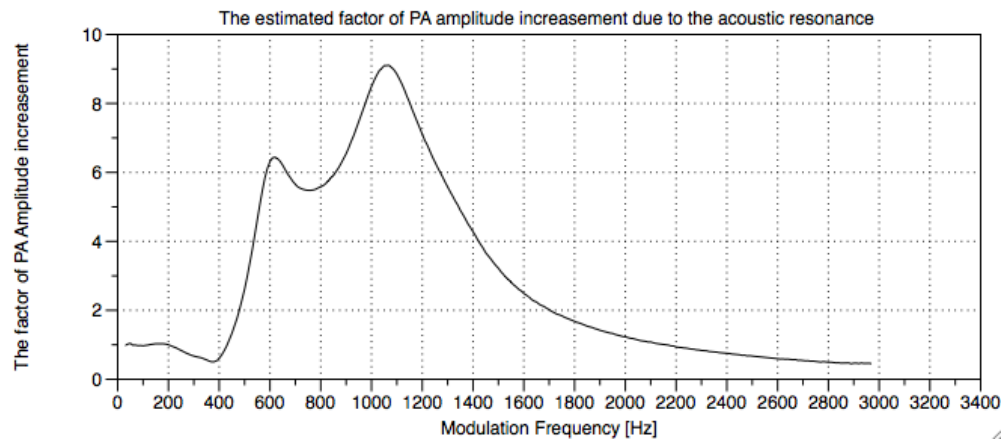


Figure 4.19: The PA amplitude enhancement factor due to the acoustic resonance effect of the cell.

As discussed previously, since the composite piston effect has not been taken into the consideration, the maximum error in this plot can be estimated to be occurring at the highest frequency of 3000 Hz. However, this error will not affect the shape of this PA amplitude enhancement curve given by the acoustic resonance.

This PA amplitude enhancement curve can be used to remove the acoustic resonance effect from the PA frequency spectrum, as shown in Figure 4.19. After normalization, this process is implemented for all the characterized thin-film structures under test (presented in Figure 4.17). The PA amplitude decreases with increasing the modulation frequency and it possesses a spectral “fingerprint” which is due to acoustic resonance. Now that these are well understood they can be removed, an example of which is shown in Figure 4.20. Using this type of

signal calibration and modeling, the PA system can be applied to thin-film characterization for semiconductor industrial applications.

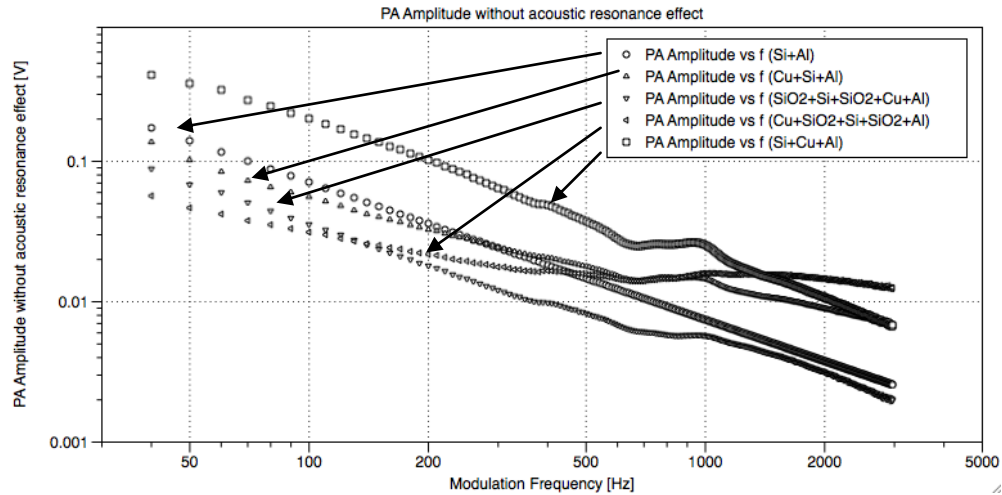


Figure 4.20: The normalized PA Amplitude Frequency Response for different thin film semiconductor material structures, wherein the acoustic resonance effect has been removed from Figure 4.17 using Figure 4.19. (Light source: NIR laser diode with 808 nm wavelength; Lock-in amplifier settings: time constant = 300 ms, sensitivity = 500 mV). Sample List: Sample 1: bare silicon; Sample 2: bare silicon wafer with a ~ 300 nm copper layer deposited on the top surface, Sample 3: Bare silicon wafer with ~ 300 nm SiO_2 layers deposited on both sides of the wafer and a ~ 300 nm copper layer deposited on the back surface of the wafer; Sample 4: Bare silicon wafer with ~ 300 nm SiO_2 layers deposited on both sides of the wafer and a ~ 300 nm copper layer deposited on the top surface of the wafer; Sample 5: bare silicon wafer with a ~ 300 nm copper layer deposited on the bottom surface of the wafer. All PA samples have been placed on the Aluminium backing material during the measurements.

APPLICATIONS OF THE PHOTOACOUSTIC SYSTEM

5. Applications of the PA system

5.1. PA signal modeling of multi-layered semiconductor structures

As discussed in chapter 4, neglecting the acoustic resonance effect, the photoacoustic signal is proportional to the temperature variation at the sample-gas interface. [5.1] The interpretation of PA signal contrast for layers embedded within semiconductor materials can be simplified, by modelling the thermal wave diffusion process only. Salazar *et al.* developed a simplified theory to discuss the thermal diffusion process within such multilayer structures. [5.2] The thermal diffusion interference of each layer and bonding interface can be calculated using an individual transfer matrix. By multiplying these matrices together, it becomes very easy to predict the PA signal (phase and amplitude) in any given multi-layered structure. In this section, from the theoretical point of view, a set of the sample structures have been used to demonstrate the sensitivity of the PA system developed in chapter 3, using the theory of Salazar et al.

For an isotropic, homogeneous, optically opaque and semi-infinite material, the internal temperature distribution, where $x \leq 0$ when the probe position is below the top surface, can be calculated as:

$$\begin{aligned}
 T(x,t) &= \frac{H_0}{2\sqrt{\rho ck\omega}} e^{-x\sqrt{\frac{\omega}{2\alpha}}} e^{j(\omega t - x\sqrt{\frac{\omega}{2\alpha}} - \frac{\pi}{4})} \\
 &= \frac{H_0}{2\sqrt{\rho ck\omega}} e^{-\frac{x}{\mu}} e^{j(\omega t - \frac{x}{\mu} - \frac{\pi}{4})} = \frac{H_0}{2k\sigma} e^{-\sigma x + j\omega t}
 \end{aligned}
 \tag{5.1}$$

where all parameters are previously defined in Chapter 2 and $j = \sqrt{-1}$. The modulated thermal wave below the surface will be heavily damped to $1/e$ of its initial amplitude and shifted by -115° or $360/\pi$ in phase, after it propagates one thermal diffusion length away from the heated spot. At the surface, the phase lag is -45° between the heat source and resulting surface temperature and the temperature is determined by the thermal effusivity, $\sqrt{\rho C k}$ ($\text{Ws}^{1/2}\text{m}^{-2}\text{K}^{-1}$). Lower values of thermal effusivity lead to higher surface temperature amplitudes.

When one modulated thermal wave penetrates perpendicularly through the interface between two isotropic homogeneous semi-infinite materials running from medium 1 to medium 2, both reflection and transmission occurs.

At the interface, where $x = 0$, where the initial heat flow, labelled as T_i , is given as

$$T_i = \frac{H_0}{2k\sigma} e^{-\sigma x + j\omega t} \quad (5.2)$$

The reflected heat flow, labelled as T_r , can be calculated as

$$T_r = R \frac{H_0}{2k\sigma} e^{\sigma x + j\omega t} \quad (5.3)$$

The transmitted heat flow, labelled as T_t , can be calculated as

$$T_t = T \frac{H_0}{2k\sigma} e^{-\sigma x + j\omega t} \quad (5.4)$$

where $R = \frac{1-b}{1+b}$ is the reflection coefficient, $T = \frac{2}{1+b}$ is the transmission

coefficient and $b = \frac{\sqrt{k_2 \rho_2 C_2}}{\sqrt{k_1 \rho_1 C_1}}$, and the positive x direction runs from medium 1

to medium 2. The values of R and T depend on the thermal mismatch between the two media, the ratio of thermal effusivity, which are independent of the modulation frequency. When applying the material properties to the equation 5.2, 5.3 and 5.4 above, the reflection coefficient R can be calculated. For the thermal wave travelling through the interface from copper to silicon or from silicon to air, R at the bonding interface is 0.407 or 0.999, respectively.

This approach to calculating the PA signal turns out to be particularly suitable for investigating the properties (thickness, thermal effusivity mismatch and interface defects) of coatings on a thermally thick substrate. When the coating thickness is far less than the thermal diffusion length, the amplitude signal is more sensitive than the phase data. The phase signal will give the best contrast when the film thickness is about 30% of its thermal diffusion length. [5.1]

When a distinct layer with limited thickness (l_2) has formed at the interface between two media, for example an air gap between the copper interconnection layer and the silicon substrate, the effective reflection coefficient Γ of the interface layer becomes a complex number. [5.1, pp. 106-108] It can be calculated as:

$$\begin{aligned}
\Gamma &= \frac{\Gamma_1 + \Gamma_2 e^{-2\sigma_2 l_2}}{1 + \Gamma_1 \Gamma_2 e^{-2\sigma_2 l_2}} \\
\Gamma_1 &= \frac{1 - b_{21}}{1 + b_{21}} \\
\Gamma_2 &= \frac{1 - b_{32}}{1 + b_{32}} \\
b_{i+1,i} &= \frac{\sqrt{k_{i+1} \rho_{i+1} C_{i+1}}}{\sqrt{k_i \rho_i C_i}}
\end{aligned} \tag{5.5}$$

where the subscripts 1, 2, 3 refer to the media 1, 2, 3 respectively. Γ_1 and Γ_2 are the reflection coefficients for thermal waves travelling from medium 1 to medium 2 and medium 2 to medium 3, respectively. Due to the presence of the σl term in equation 5.5, the effective reflection coefficient of a layer interface has both phase and amplitude values. It is dependent on the modulation frequency of the thermal wave.

By way of example, let us consider an air gap with finite thickness of 10 nm, 100 nm, 1 μ m and 10 μ m, respectively, between two thermally thick silicon wafers. Such structures are typically introduced by delamination generated during the wafer bonding process. Using equation 5.5, the effective reflection coefficient dependency on the modulation frequency of the thermal wave can be calculated, as shown in Figure 5.1.

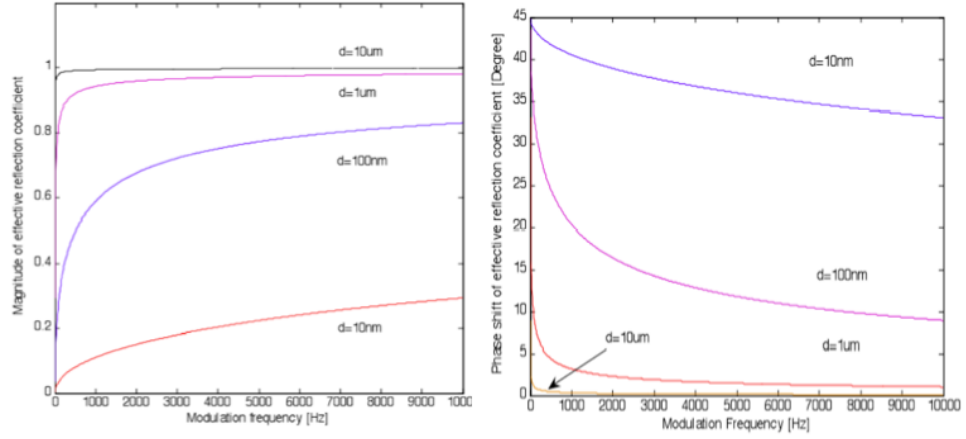


Figure 5.1: The effective reflection coefficient for an embedded air gap layer in silicon with finite thickness d (labelled as l_2 in equation 5.5) as a function of the modulation frequency. This coefficient is a complex number. It includes both amplitude (left) and phase components (right).

Having established the basic properties of thermal waves and their interactions at the interfaces, it is possible to calculate the surface temperature as a result of thermal wave interference in the top layer. Consider the propagation of a plane thermal wave in a thin layer of material of thickness L . We assume that the thermal properties of all the media concerned are homogeneous. The subscript c , b , g will be used to refer to the coating, substrate and gas media, respectively. The substrate layer is assumed to be thermally thick and the coating layer is exposed to the air. The thermal wave is generated on the top surface, which is valid for an absorbing coating or a metallization layer on the top surface.

The surface temperature can be expressed as:

$$T_{x=0} \propto T_g \frac{1 + R_b e^{-2\sigma_c L}}{1 - R_b R_g e^{-2\sigma_c L}} \quad (5.6a)$$

where R_g and T_g are the thermal wave reflection and transmission coefficients at the coating-air interface, respectively. R_b is the reflection coefficient of the interface between the coating and substrate. [5.1, pp. 106-108, eq (5.11) therein] Assuming there is a thin air layer of 100 nm thickness embedded at a varying depth L inside a semi-infinite silicon substrate, the normalized amplitude and phase shift of the top surface temperature can be calculated using equation 5.6. A plot of this is shown in Figure 5.2. Within the modulation frequency range of 10Hz to 10kHz, both the amplitude and phase signals are sensitive to the presence of such a thin air gap with an embedded depth running from 1 μm to 300 μm . The shallower the air gap layer is embedded, the better is the signal contrast introduced by the air gap.

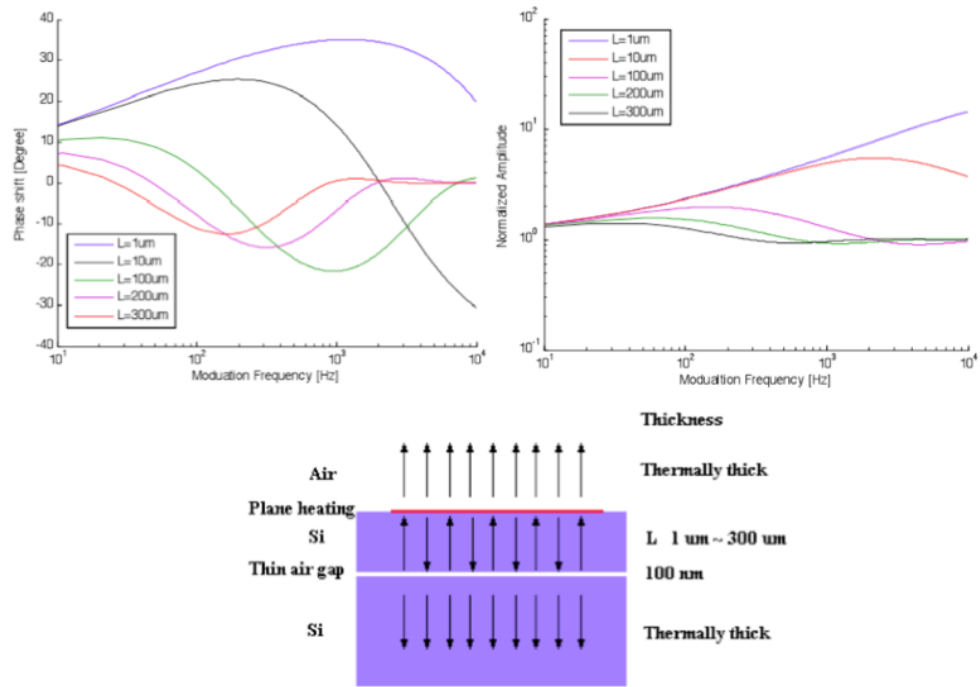


Figure 5.2: Normalized Amplitude and Phase Shift of the top surface temperature for a 100 nm thick air layer embedded in semi-infinite silicon substrate. The depth of the air layer below the top surface varies from 1 μm to 300 μm .

Thus the use of the thermal wave has been numerically proven to have the capability to detect non-destructively delamination defects at the bonding interface between two silicon wafers or embedded cracks parallel to the silicon wafer surface.

Using similar calculations, an air gap with varying thickness from 10 nm to 10 μm is also shown to be detectable through a 1 μm thick copper capping layer using this thermal wave method. The frequency response of the PA signal is illustrated in Figure 5.3.

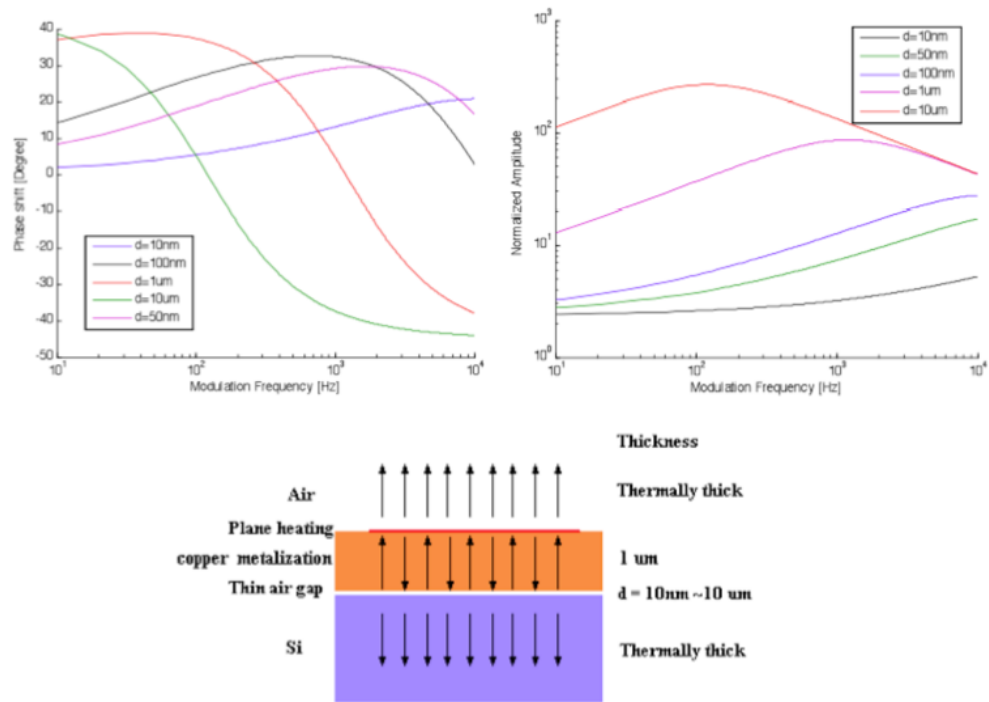


Figure 5.3: Normalized Amplitude and Phase Shift of the top surface temperature for a delamination layer (air) under a 1 μm -thick copper metallization layer on a semi-infinite silicon substrate. The air layer thickness varies from 10 nm to 10 μm .

For other multi-layered structures subjected to plane heating on the top surface, Salazar *et al.* have provided a general solution for the surface temperature calculation [5.2], which is described as follows: Consider an opaque and stratified material made of n parallel layers ($i=1, 2, 3, \dots, n$), the thickness of each layer is defined as l_i , its thermal diffusivity is D_i and its thermal effusivity is e_i . The light source intensity (I_0) of the PA system is modulated at a frequency f .

The temperature at the illuminated surface can be described by the transfer matrix method:

$$\begin{aligned}
T_0 &= \frac{I_0}{2} \frac{A}{C} \\
\begin{pmatrix} A & B \\ C & E \end{pmatrix} &= \prod_{j=1}^n \begin{pmatrix} A_j & B_j \\ C_j & E_j \end{pmatrix} \\
A_j &= E_j = \cosh(q_j l_j) \\
B_j &= \frac{\sinh(q_j l_j)}{E_j \sqrt{i\omega}} \\
C_j &= E_j = \sinh(q_j l_j) \\
q_j &= \sqrt{\frac{i\omega}{D_j}} \tag{5.6b}
\end{aligned}$$

where q_j is the thermal wave vector. The extra thermal resistance, R_{th} , at the layer interfaces can be accounted for by inserting the matrix $\begin{pmatrix} 1 & R_{th} \\ 0 & 1 \end{pmatrix}$ between the two adjacent matrices j and $j+1$ into equation 5.6a. [5.2]

Therefore, the surface temperature depends on the thermal diffusivity, thermal effusivity of each layer and the thermal resistance at the layer interfaces within a thermal diffusion length. It is possible to measure the variations of these properties for buried multi-layer structures, such as metallization interconnections, using thermal wave methods. As shown in Figure 5.4, both the phase and amplitude of the top surface temperature variation can be used to confirm the existence of a thin air gap (thickness = 100 nm) inside multilayer Cu/SiO₂ sandwich structures. It can therefore be concluded that the PA system has great potential to reveal subsurface defects in advanced semiconductor materials and devices.

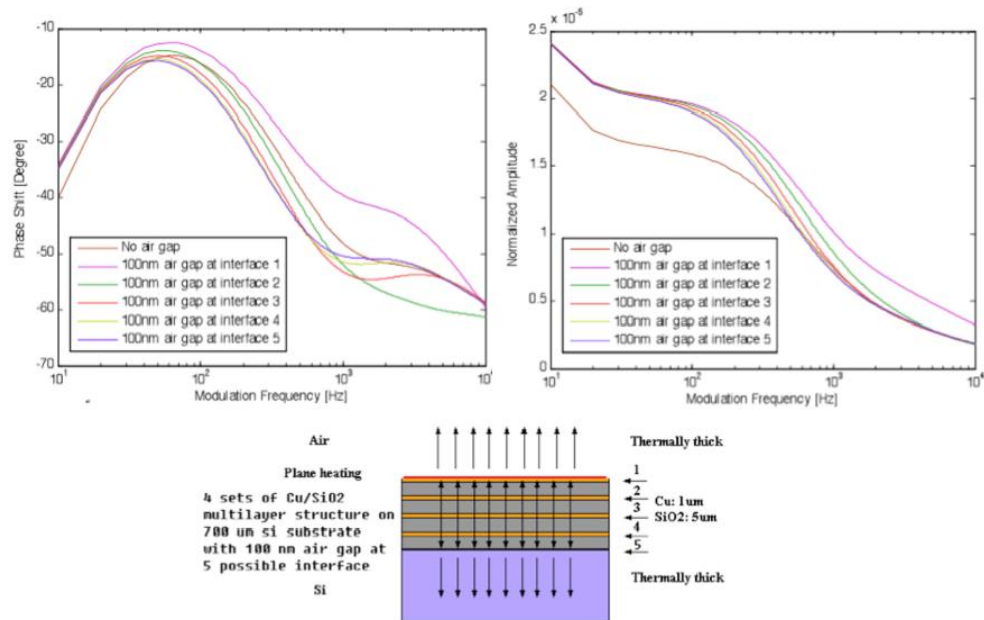


Figure 5.4: Normalized Amplitude and Phase Shift of the top surface temperature for a multilayer Cu (1 μ m)/SiO₂ (5 μ m) structure on a thermally thick silicon substrate.

5.2. Application 1: PA imaging of subsurface air trenches in silicon

In this section, the PA system is used to characterize via the wafer backside a set of two air trenches, which are laser machined in a silicon substrate. Both amplitude and phase images reveal the subsurface features. The frequency dependence of the photoacoustic signals with different laser spot sizes was compared and analyzed with a one-dimensional model developed by Salazar *et al.* The effect of lateral heat diffusion on subsurface defect characterization is investigated.

Identifying embedded air voids and metallization defects that affect the integrity of integrated circuits, in a rapid and nondestructive manner, can be of considerable use for metal interconnect processing. As stated earlier, the PA system is a relatively low-cost, non-contact, non-destructive analysis technique,

which has the capability to detect embedded structures as deep as several hundred microns without any material pre-processing. As discussed in section 5.1, both the phase and amplitude signals are sensitive to perturbations in thermal wave propagation, resulting from localized changes in the thermo elastic properties at a defect site. Some similar techniques have been used successfully to identify voids and micro-cracks in an aluminium metallization process [5.3].

Using the PA system described in chapter 3, the data acquisition time in this test is as short as 50 ms per point. The sample comprises of a 1 cm by 1 cm piece of silicon wafer (thickness = 680 μm) with 2 air trenches laser machined on the surface. The measured trench dimensions are 2 mm by 5 mm by 200 μm and 2 mm by 5 mm by 300 μm . They are labeled as position A and C respectively in Figure 5.5 and 5.6. The sample is mounted in the PA cell on a silicon substrate (thickness = 500 μm) with the machined side facing away from the probe laser. This eliminates the thermal wave interaction between the sample and cell backing material. As the machined trenches are ~ 500 μm below the top surface, which is far greater than the optical penetration depth for an 808 nm laser in silicon (~ 10 μm) [5.5], we are effectively probing these sample features with the thermal wave.

Figure 5.6 shows the photoacoustic microscopy images for a grid of 200 by 200 points recorded from an 8 mm by 8 mm area on the sample, investigated with 40 μm step size and 170 μm laser spot size. The modulation frequency and the peak output laser power are set to 917 Hz and 800 mW, respectively. The thermal wave generated during one period of the modulation cycle propagates a distance determined by thermal diffusion length (~ 160 μm at 917 Hz) and interacts with the subsurface defects. Both photoacoustic amplitude and phase images revealed the two 5 mm by 2 mm laser machined trenches, although the embedded depth of the structures is almost three times that of the calculated thermal diffusion length. With our current experimental set up, the phase image has better contrast

and more accurately reflects the actual subsurface structure size as shown in Figure 5.7. Both images confirmed that the right trench (position C) is slightly deeper than the left one (position A), which is consistent with the sample geometry.

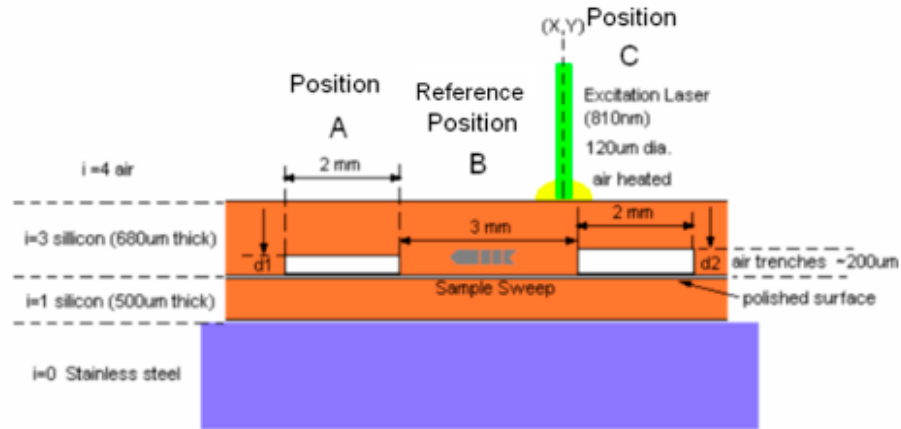


Figure 5.5: Geometry of the silicon sample under test.

In Figure 5.7, the PA microscopy line scans across the region containing the trenches. It shows a slight slope difference for the PA signal at the edges of the embedded trenches. It is believed that this is induced by the PA edge effect when the probe laser crosses the trenches embedded at different depths. To evaluate the general photoacoustic contrast mechanism and to simplify the calculation complexity, we consider a 1D model, which is valid when the spot size of the laser is significantly bigger than the thermal diffusion length. As this assumption is not strictly true for our configuration, we find semi-quantitative agreement with our data.

Using thermal wave solutions for a three layer sample between two semi-infinite, optically non-absorbing media and assuming the optical penetration depth is much smaller than the first layer thickness, the complex top surface temperature

T_s has been calculated using the formulas presented in equation 5.6, with the sample geometry at positions A, B and C in the modulation frequency range from 1 Hz to 2000 Hz.

To eliminate the systematic delivery function of the PAM system, such as PA cell acoustic resonance effects, and make the analysis results comparable with other photothermal techniques, both the measured and the theoretical data are presented in the form of normalized signals:

$$\theta_n(f) = \theta_s(f) - \theta_{ref}(f) \quad (5.7)$$

$$A_n(f) = A_s(f) - A_{ref}(f) \quad (5.8)$$

where, $\theta_{ref}(f)$, $A_{ref}(f)$ refer to the phase and amplitude signal from position B in Figures 5.5, 5.6 and 5.7, a homogeneous reference region without the embedded structures and, $\theta_s(f)$, $A_s(f)$, refer to the signal from either position A or C above the middle of the buried air trenches. The minus sign for the normalized phase refers to the time delay of the temperature variation on the top surface for the samples with embedded structures when compared with the phase signal from the homogeneous region of the sample.

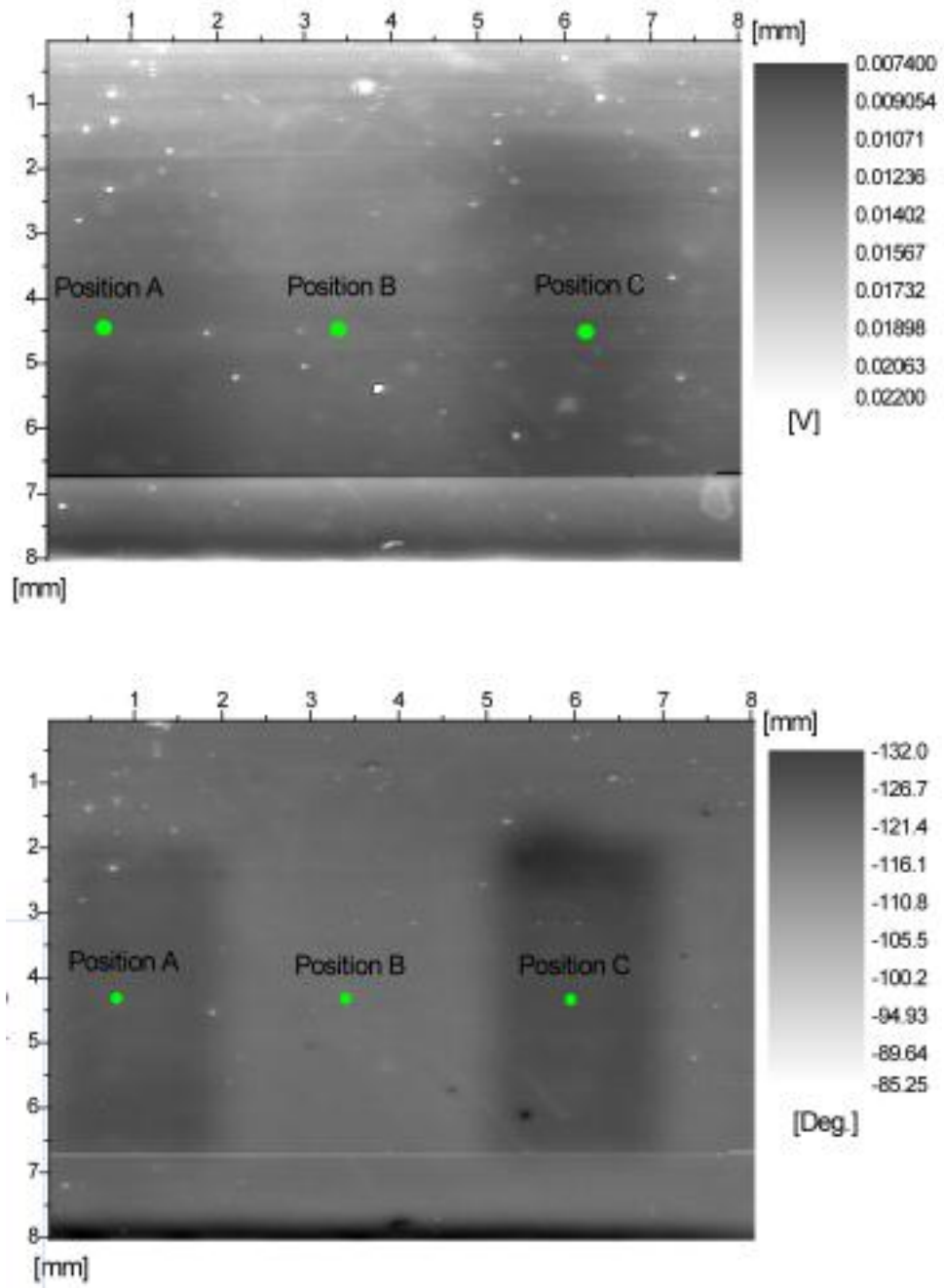


Figure 5.6: Recorded Photoacoustic Amplitude (upper) and Phase Images (lower) at 917Hz with 40um step size.

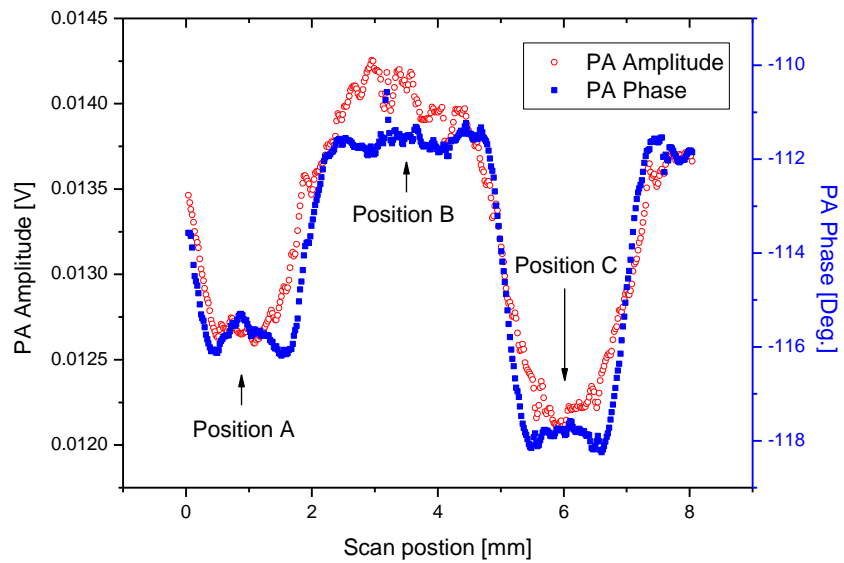


Figure 5.7: Photoacoustic line scan across the two embedded trenches at 917Hz with 40um step size.

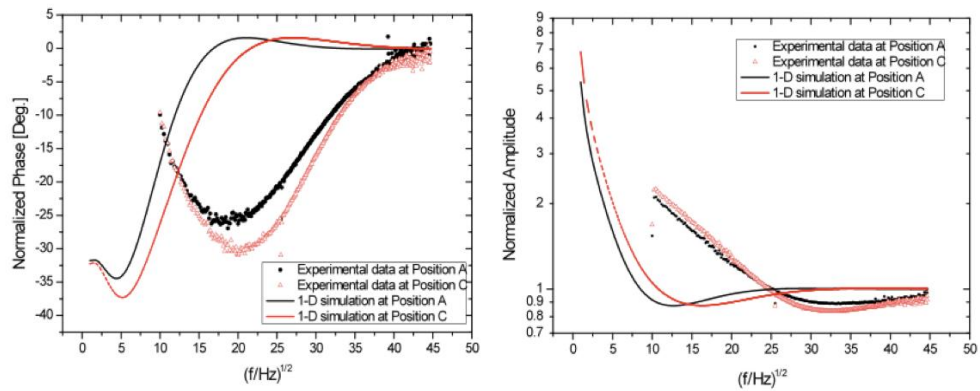


Figure 5.8: Normalized photoacoustic amplitude (left) and phase (right) experimental data with 170 um laser spot size and simulation results at position A and C marked in Figure 5.5

As shown in Figure 5.8, the phase is much more sensitive, giving up to -35 degree signal contrast, to the reflected thermal wave from the subsurface defects, in our measured frequency range. The PA amplitude is strongly dependent on the optical absorption coefficient and the morphology of the top surface, whereas the phase relies on the thermal diffusivity of the subsurface volume. This experimental data follows the same variation predicted by the 1D simulation. However, in the low frequency range, lateral heat transport, not considered in the 1D model, plays an important role and causes considerable differences between the measured and simulated results.

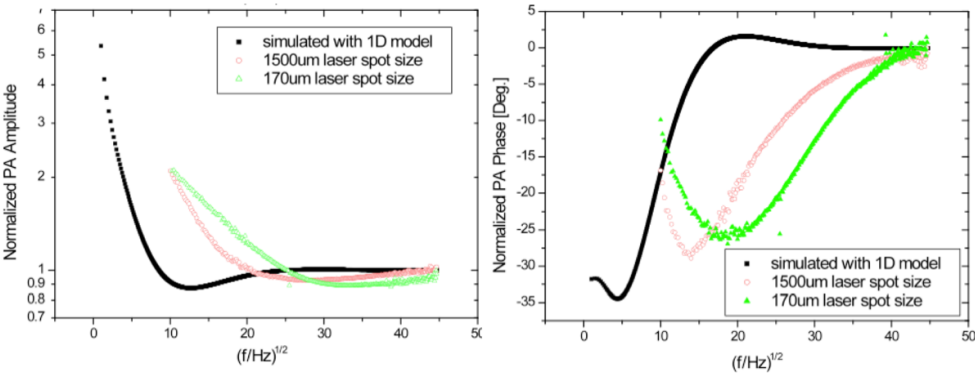


Figure 5.9: Frequency dependence of normalized phase (left) and amplitude (right) with varying laser spot size at position A

By enlarging the laser spot size, we observe that the measured relative phase minimum occurs at a lower modulation frequency and the maximum phase contrast is increased as shown in Figure 5.9. In the limit that the laser spot is far bigger than the thermal diffusion length, one would expect to recover the 1D simulation curve experimentally. Similar results were observed for a diamond like carbon (DLC) coatings on a metallic alloy using photothermal displacement measurements [5.7].

5.3. Application 2: PA imaging of wafer bonding defects

The silicon on insulator (SOI) technique is a popular substrate fabrication method for the manufacture of electronic devices with improved speed for low power consumption and low voltage applications. One of the fast processing methods to produce SOI wafers is wafer bonding, which is referred as bonded silicon on insulator (BSOI).

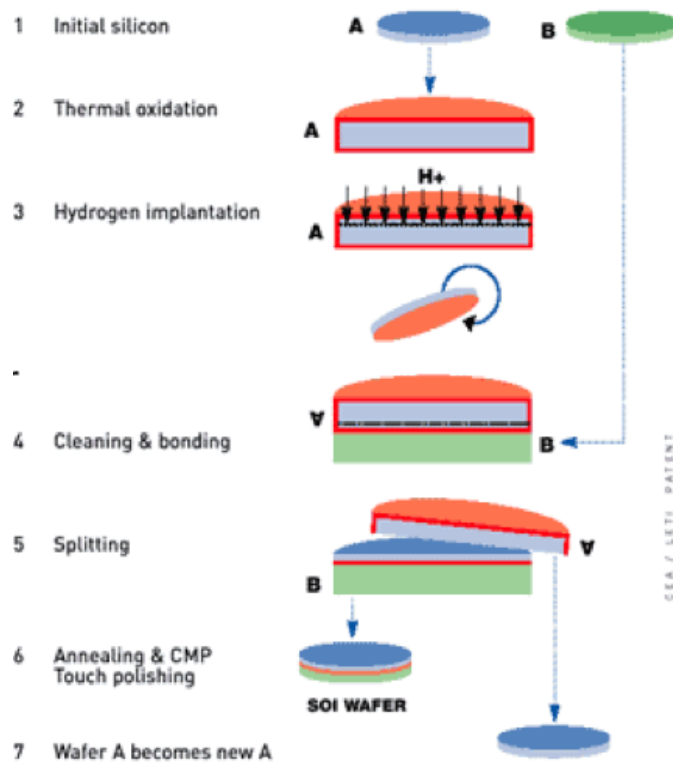


Figure 5.10: The BSOI wafer manufacturing process, reproduced from reference [5.10]

As described by Maszara, this method basically connects a seed wafer (e.g. silicon) with one oxidized surface to a silicon-handling wafer by directly contacting them. [5.8] After thinning the handling wafer, the resulting BSOI wafer has the

following multi-layer structure: thin silicon layer – silicon oxide – substrate (e.g. silicon). The detailed process flow is illustrated in Figure 5.10.

For ULSI applications (ultra large scale integration), it is essential to control the crystalline quality of the upper thin silicon film. There are three main defects that can have very deleterious consequences: dislocations and their strain fields, voids or non-bonded areas and long-range strain fields originating from the bonding interface.

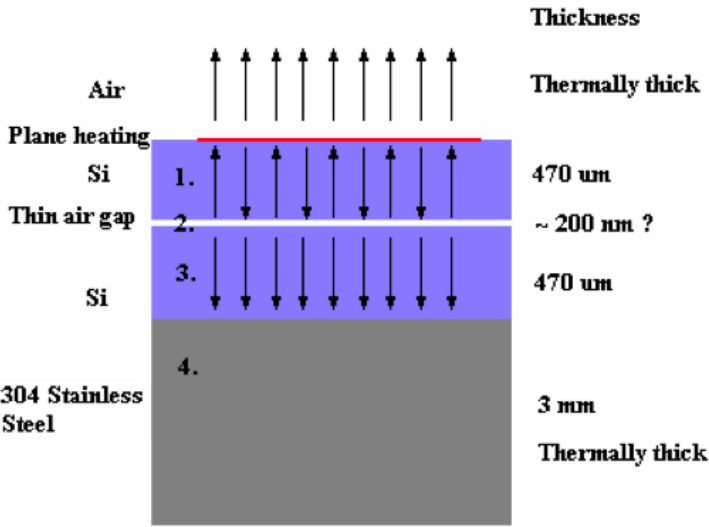


Figure 5.11: The sample geometry used to model the temperature variation on the top surface with a wafer-bonding defect included.

Synchrotron X-ray topography (SXRT) and infrared gray field polariscopy (IR-GFP) can be used for full-field measurements of the residual stresses arising from wafer bonding. [5.9] We will show that the PA system, presented in this thesis, also has the capability to detect non-destructively these interface defects. Unlike the IR-GFP method, the PA system is more robust and insensitive to the wafer process steps. It is possible to characterize deeply embedded defects even when the wafers are optically opaque, e.g. with a metal layer coating on the top surface.

Using the theory developed by Salazar *et al.*, which has been described in section 5.1, it is possible to calculate the PA signal for a multi-layer structure. Two silicon wafers (thickness = 470 nm) are bonded by contacting each other, as shown in Figure 5.11. At certain positions on the bonding interface, delamination defects are presented. To simplify the model, these defects are treated as thin air gaps with different thickness. During the measurements, the samples are placed upon a stainless steel backing material. The mathematical model assumes that the optical penetration depth of the excitation laser is much smaller than the thermal diffusion length for all modulation frequencies of interest. This assumption is valid since the energy of the excitation laser used in this test (808 nm; $E = 1.54$ eV) is above the silicon band gap energy ($E_g = 1.1$ eV). The material properties of each layer are given in Table 5.1 below.

Material	Density (Kgm⁻³)	Specific Heat (JKg⁻¹K⁻¹)	Thermal Conductivity (Wm⁻¹K⁻¹)	Thermal Diffusivity (10⁻⁶m²s⁻¹)	Thermal Effusivity (Ws^{1/2}m⁻²K⁻¹)
Silicon	2330	712	148	89.21	15669.27
Air	1.16	1007	0.026	22.26	5.51
304 Stainless Steel	8000	500	16.2	4.05	8050

Table 5.1: The material properties of each layer included in the sample geometry illustrated in Figure 5.11. The same material properties have also been used in Chapters 2 & 3.

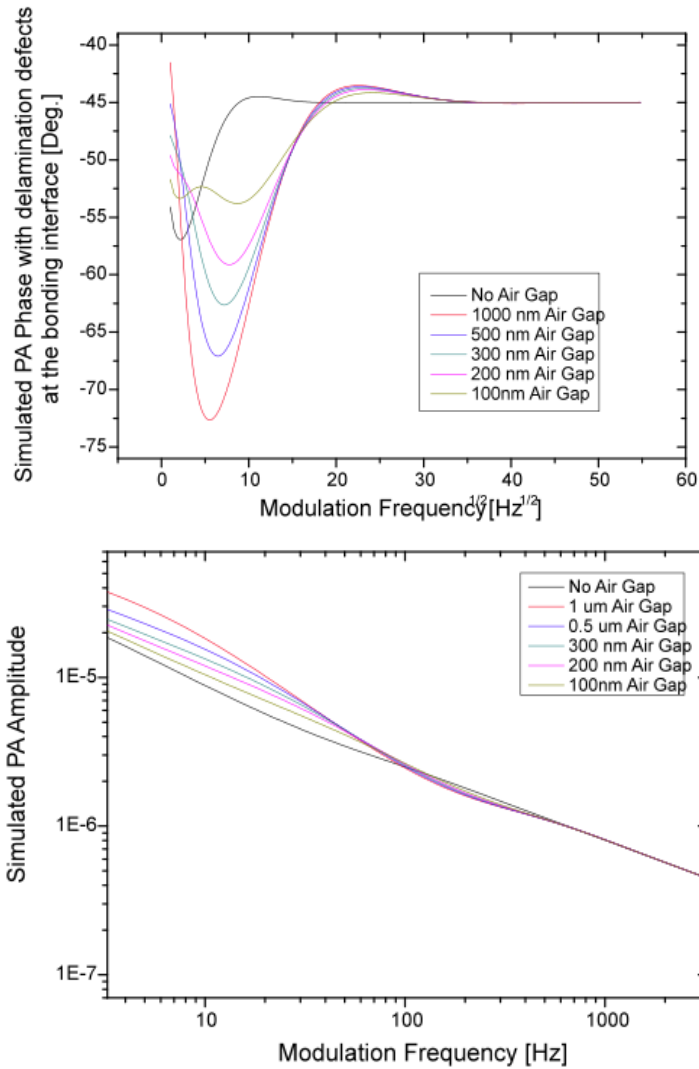


Figure 5.12: The simulated PA frequency dependence based the theory developed by Salazar *et al.* [5.2]. The x-axis unit of the PA Phase plot is \sqrt{f} to provide more detail in the lower frequency range. The PA Amplitude is plotted using log scale for both x and y-axes to verify the general linear behaviour of the frequency response. The sample geometry is given in Figure 5.11 and the material properties are provided in Table 5.1.

Using the MATLAB® simulation suite, the frequency dependence of the PA Amplitude and Phase can be calculated using the code, which is shown in the

appendix section at the end of this thesis. As shown in Figure 5.12, the PA amplitude decreases while the modulation frequency increases. When there is no defect at the bonding interface, the PA amplitude is linearly proportional to f^{-1} . For both PA amplitude and phase, the sensitivity to the existence of the embedded air layer disappears at higher modulation frequencies, as in these situations the thermal diffusion length is smaller than the subsurface depth of the air gap.

The PA system described in chapter 3 was used in this test. A bonded silicon wafer was cut into 9 mm by 9 mm pieces to fit into the PA cell. The sample geometry is given in Figure 5.11. Unlike the situation for the detection of bonding defects using PA imaging in transmission mode [5.11], by measuring the temperature variation on the top surface, PA scanning images are captured herein. This feature allows the PA system to be used at higher modulation frequencies. This will reduce the thermal diffusion length to improve the lateral resolution of this microscopy application and reduce the minimum time required (f^{-1}) for the lock-in amplifier to wait when detecting the PA signal at each pixel. Using helium as the coupling gas in the PA cell and setting the modulation frequency to 220 Hz, a set of PA images comprised of 10,000 pixels (data consisting of PA amplitude and phase), can be captured in less than 8 minutes. An example of the PA scanning results is shown in Figure 5.13.

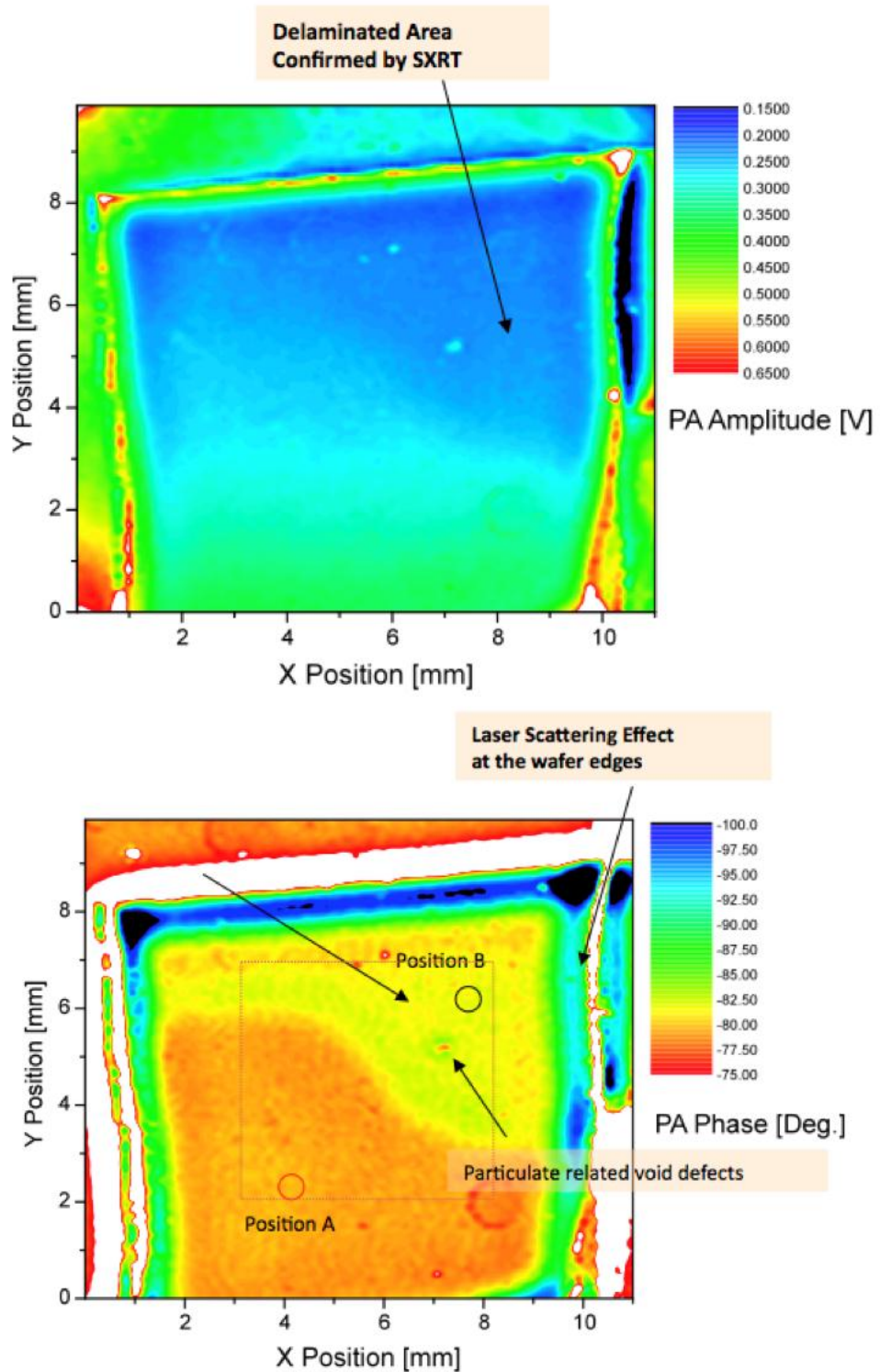


Figure 5.13: PA mapping images of de-bonded silicon wafers. (PA amplitude: upper image; PA Phase: lower image. (Sample Name: HBH-200, Light source: IR laser diode 808 nm, PA cell filled with Helium Gas, Modulation frequency = 220

Hz, Lock-in amplifier setting: Float coupling, sensitivity = 1V, time constant = 10 ms, Total image acquisition time = 8 min)

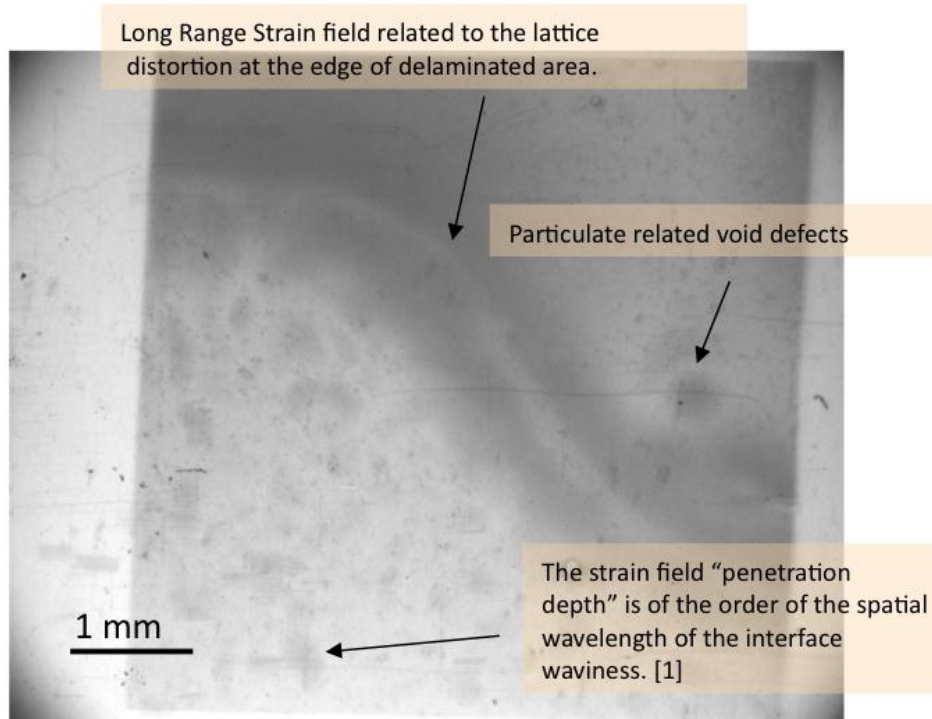


Figure 5.14: White beam synchrotron x-ray topography (SXRT) of bonded silicon wafers. (Exposure Configuration: [-1 -1 9] Large area Back-reflection (LABRT), sample-film distance = 80 mm, x-ray penetration depth = 153 μm , beam current = 85.597 mA, exposure time = 186 sec)

Both PA amplitude and phase images show the existence of a de-bonded area at the top right hand corner of the sample. In addition, the PA system detected a small particle-related defect at the bonding interface, which has been confirmed by SXRT-LABRT results, as shown in Figure 5.14. With the given modulation frequency of 220 Hz, the PA signal difference between the bonded and de-bonded area is $\sim 2^\circ$ phase and ~ 50 mV in amplitude. In this test case, the phase signal is more sensitive than the amplitude and the lateral resolution is ~ 0.1 mm.

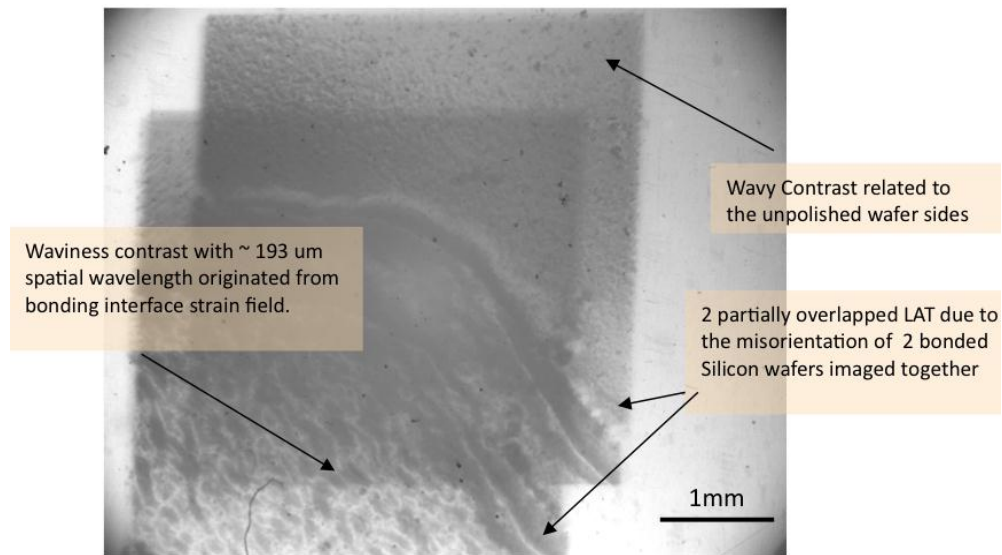


Figure 5.15: White beam synchrotron x-ray topography (SXRT) of bonded Si wafers. (Exposure Configuration: $[-2 -2 0]$ Large area transmission (LAT), sample-film distance = 95 mm, x-ray penetration depth = 1.361 mm, beam current = 83.45 mA, exposure time = 497 sec)

To verify the results given by the PA system, a 5 mm by 5 mm area, delineated by the dotted area in Figure 5.13 (bottom image), has been characterized using synchrotron x-ray topography (SXRT). These experiments were performed at HASYLAB-DESY, Hamburg, Germany, utilizing the continuous spectrum of synchrotron radiation from the DORIS III storage ring bending magnet source. The ring operated at the positron energy of 4.45 GeV and at typical currents of 80–150 mA. The Laue/Bragg diffraction patterns were recorded on Geola VRP-M Holographic films, which have an emulsion grain size of about 40 nm.

Figures 5.14 and 5.15 are typical x-ray topography results in large area back reflection and transmission modes, respectively. In the transmission topography, the white x-ray beam penetrates through the sample and the resulting diffraction pattern was imaged on a film placed 95 mm behind the bonded wafers. Both the diffraction image from the top and the bottom silicon substrates are visible.

These are partially overlapped due to the small rotational misalignment between the two bonded wafers. The strong dark contrast across the complete characterization area from left to right, is the border of the de-bonded regions, which can be related to strong lattice distortion. Within the de-bonded area, top right hand corner of the sample, the “orange peel” contrast is related to the unpolished surface of the silicon substrate. For the bonded region, the wavy/sinusoidal “cellular” black/white contrast becomes much stronger and its spatial wavelength has increased to $\sim 193 \mu\text{m}$.

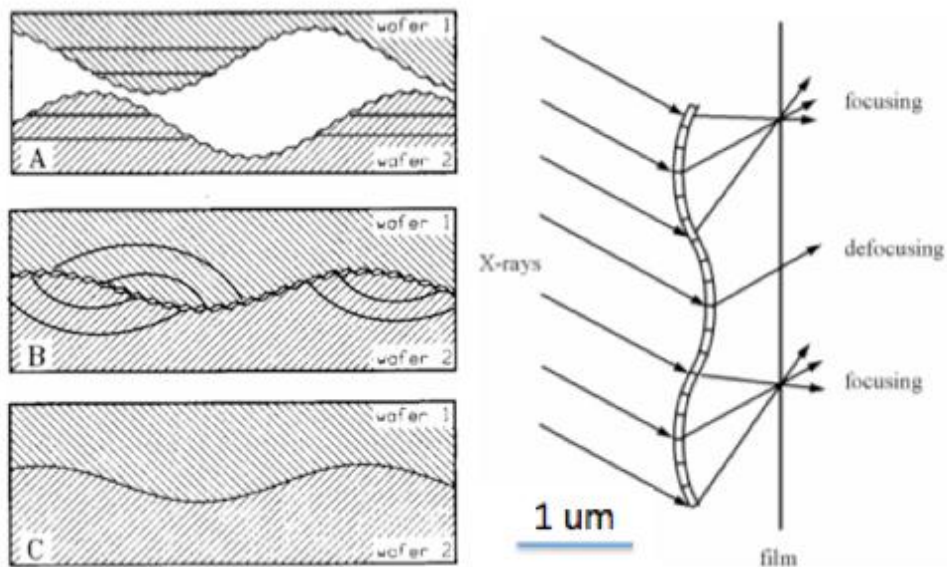


Figure 5.16: Left plot: Schematic representation of the deformation introduced by the bonding process (A) wafer surfaces before bonding, (B) after room temperature bonding, (C) after complete bonding at high temperature [5.8]. The six horizontal (in A) and bent (in B) lines illustrate the form of a set of lattice planes before and after bonding. Right plot: Illustration of the focusing-defocusing behaviour of a thin crystal film with a wavy (sinusoidal) deformation. [5.8, 5.12]

Härtwig and Köhler have demonstrated a quantitative method to estimate the crystal deformation at the bonding interface. [5.12] In their X-ray topography

results for most samples, the main spatial frequency of the image intensity contrast varied in the range from 100 μm to 300 μm . The contrast formation mechanism is found to be orientational contrast (and not extinction contrast with varying integrated reflectivity), which can be interpreted by an interface deformation model proposed by Maszara and shown in Figure 5.16. [5.8]

The crystal plane at the bonding interface is deformed in the process of contacting two silicon wafers to each other. The local Bragg angle is perturbed by the varying misorientation of the reflecting lattice planes. Certain regions of these planes act as focusing or defocusing components. If one places the recording film at a distance close to a focal length, the x-ray topography images show a series of dark lines with a bright background, which is exactly the same as observed in Figure 5.15. Assuming a sinusoidal deformation at the bonding interface with a spatial wavelength λ and defining the sample-film distance as f , the x-ray diffraction intensity a_0 can be estimated by [5.8]

$$a_0 = \frac{\lambda^2}{16\pi f} \quad (5.9)$$

The maximum inclination Φ_0 of the deformed lattice planes can be given by [5.8]

$$\Phi_0 = \frac{\lambda}{8f} = 0.0020318[\text{rad}] = 0.116^\circ \quad (5.10)$$

This strain field will not only be confined to the region close to the bonding interface. Its penetration depth was reported to be of the same order as the spatial wavelength of the interface waviness, regardless of whether the seed wafer has been thinned down to a smaller thickness or not. This is consistent with our SXRT-LABRT results. As shown in the back reflection topograph of Figure 5.14,

the synchrotron x-ray penetration depth is calculated as 153 μm for the [-1, -1 9] topograph shown therein. The characterized silicon crystal region is about 320 μm away from the bonding interface. At the bonded region, the sinusoidal/wavy contrast, the indication of the existence of the strained crystal, is still visible. In addition, there is also a dot-like feature visible in the LABRT image, which is marked by an arrow in Figure 5.14. This feature shows a black and white contrast, which indicates that it is related to crystal deformation and there is long-range strain field around it. As noted in Figure 5.13, this feature has also been picked up in the PA Phase imaging, which confirms that the lateral resolution of the PA microscope system presented in this thesis is of the order of 100 μm .

Two typical positions have been selected on the sample, one at a bonded region and the other at a de-bonded region for a PA frequency scan. As shown in Figure 5.17, the PA frequency dependence shows relatively little difference between the two cases except at lower frequencies. To remove the acoustic resonance peaks and in order to compare the measurement results to the mathematical model described in Figure 5.12, the PA signals are again normalized as previously outlined using:

$$\theta_n(f) = \theta_s(f) - \theta_{ref}(f) \quad (5.11)$$

$$A_n(f) = A_s(f) - A_{ref}(f) \quad (5.12)$$

where, $\theta_{ref}(f)$, $A_{ref}(f)$ refer to the phase and amplitude signals from position A. $\theta_s(f)$ and $A_s(f)$ refer to the signals from either position B.

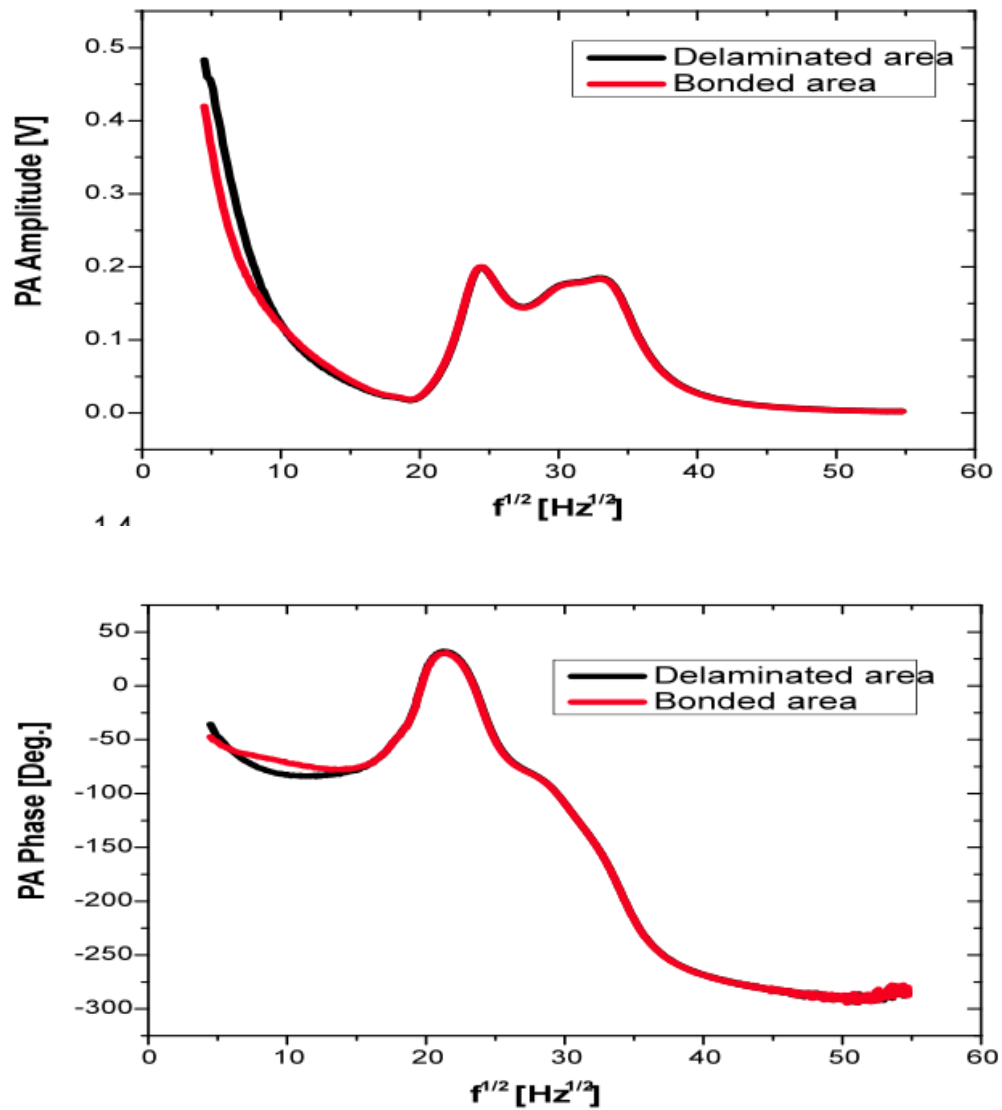


Figure 5.17: The PA frequency dependence for Amplitude (upper plot) and Phase (lower plot) at two positions on the sample surface: Position A = bonded area; Position B = debonded/delaminated area (Sample Name: HBH-200, Light source: IR laser diode 808 nm, PA cell filled with Helium Gas, Modulation frequency = 25-3000 Hz, Lock-in amplifier setting: Float coupling, sensitivity = 1V, time constant = 10 ms, Total image acquisition time = 8 min)

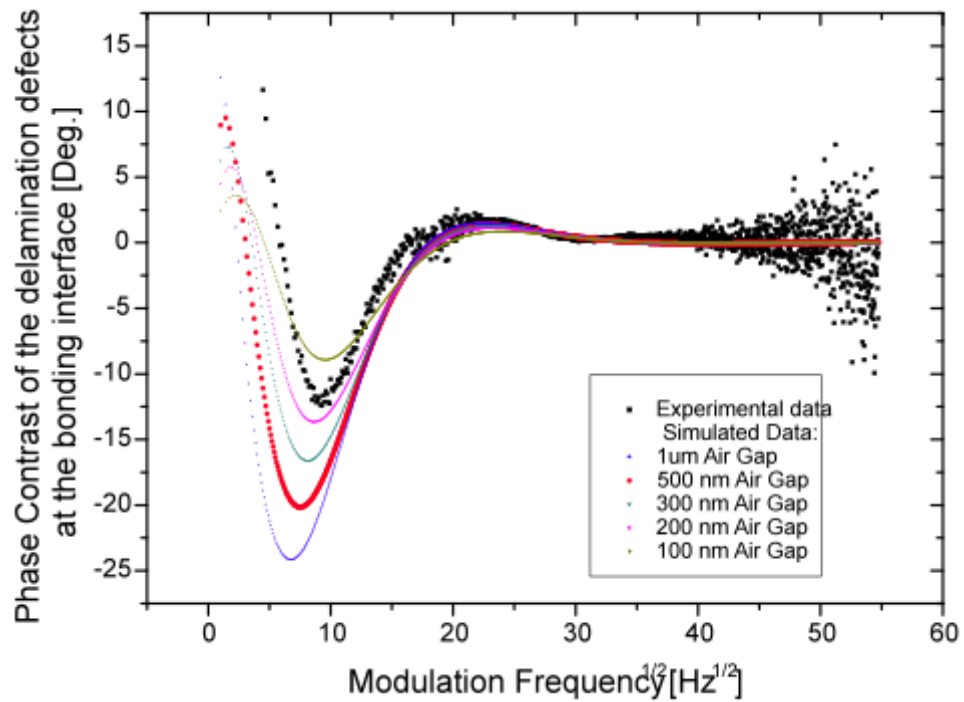


Figure 5.18: The normalized PA frequency dependence in Phase. Comparison of measured and simulated results.

After the PA signal normalization, the measured data, given in Figure 5.17, and the simulated results, given in Figure 5.12, are plotted in the same scale, as shown in Figure 5.18. The PA signal has been simulated with a varying air gap thickness at the bonding interface. The measured data is consistent with the theoretical predictions. Both datasets show very similar trends. There is some deviation at the lower frequencies, which could be due to the simplified structure assumption for the bonding interface. It could be worthwhile in the future to also include the SiO_2 layer within the simulation sample geometry when performing a function fitting for the experimental results.

As shown in Figure 5.18, the PA phase plot, as one varies the air gap thickness from 1000 nm to 100 nm, the maximum phase difference change is $\sim 16^\circ$. With

the current experimental configuration and sample geometry, the typical reproducibility in PA phase is $\sim 2^\circ$ and $\sim 0.3^\circ$ degrees for the air cell or the helium gas cell, respectively. Assuming that the phase difference is linearly proportional to the thickness difference of the air gap, the estimated sensitivity of the PA system for detection of deeply embedded air gaps is ~ 20 nm or ~ 113 nm when using Helium or air as the coupling gas.

In summary, the PA system is proven to be a lower cost and non-contact imaging technique for wafer bonding applications. It does not require a liquid coupling medium and can be applied to moisture-sensitive devices, non-annealed bonds, optically opaque or non-crystal bonding materials.

5.4. Application 3: Photoacoustic Imaging on packaged IC

With the current gas-microphone detection scheme, the modulation frequency range is from DC to 3000 Hz. In this case, the minimum thermal diffusion length in silicon is ~ 90 μm . When using higher frequencies, the damping effect of the coupling gas on the acoustic piston becomes very significant and the PA signal becomes too weak to be detected. For PAM, the thermal diffusion length determines the lateral resolution. The typical resolution (~ 100 μm) is much worse than some metrology tools, such as optical microscopy or CD-SEM. However, the PA microscope has unique advantages. Its probe depth can reach as deep as hundreds of microns below the surface. It has very high vertical resolution, as demonstrated in section 5.3. The measurement approach is robust and no sample pre-conditioning is required.

The photoacoustic images can be achieved by a variety of scans over a region of interest. One possibility is to move the excitation light source and keep the detection system unchanged. Another is to keep the excitation source fixed and to move the detection system (usually by scanning a probe beam). A third

approach is based on scanning both excitation and detection system relative to each other across the sample. In this study, the sample under test has to be placed inside a PA cell, wherein the microphone is fixed at certain location. Our PA images are therefore obtained using the 1st scanning method.



Figure 5.19: IC sample studied in this test: HN462532G

Herein, a packaged IC chip, HN462532G, is characterized. The sample picture is shown in Figure 5.19. Before placing the chip into the photoacoustic cell, the top capping material was removed to reduce the sample height, which makes it possible to fit the chip into the PA cell. It also allows direct access for the excitation laser to the patterned top surface. There is no need to scan the sample through the optical window on the package top.

Initial scans were performed on the sample by scanning through from the IC backside. As shown in Figure 5.20, no IC circuit pattern was found. Neither PA phase or amplitude images reveal the existence of an IC chip. Even though the modulation frequency was reduced to 70 Hz, the thermal diffusion length within the packaging material is still shorter than the package thickness. However, by scanning the IC sample from the topside, as shown in Figure 5.21, both PA

amplitude and phase images clearly show the electronic circuit layout. The typical lateral resolution observed here is 50 - 100 μm . The PA amplitude data are much more sensitive to the presence of particles on the top surface when compared to the PA phase data. The reason for this is that the inner wall of the PA cell can absorb the scattered light from the particles very heavily. The PA amplitude is increased significantly due to this cell effect.

Figure 5.22 shows the optical microscopy image of a manually damaged HN462532G chip. The upper left corner of the chip was totally removed and a crack, which is tens of microns wide, extends from this severely damaged area to the lower right corner. By adjusting the focusing position of the optical microscope, the adjacent area on the right along the crack can be seen to be tilted upwards. This phenomenon indicates that there is a subsurface delamination layer on the right side of the crack.

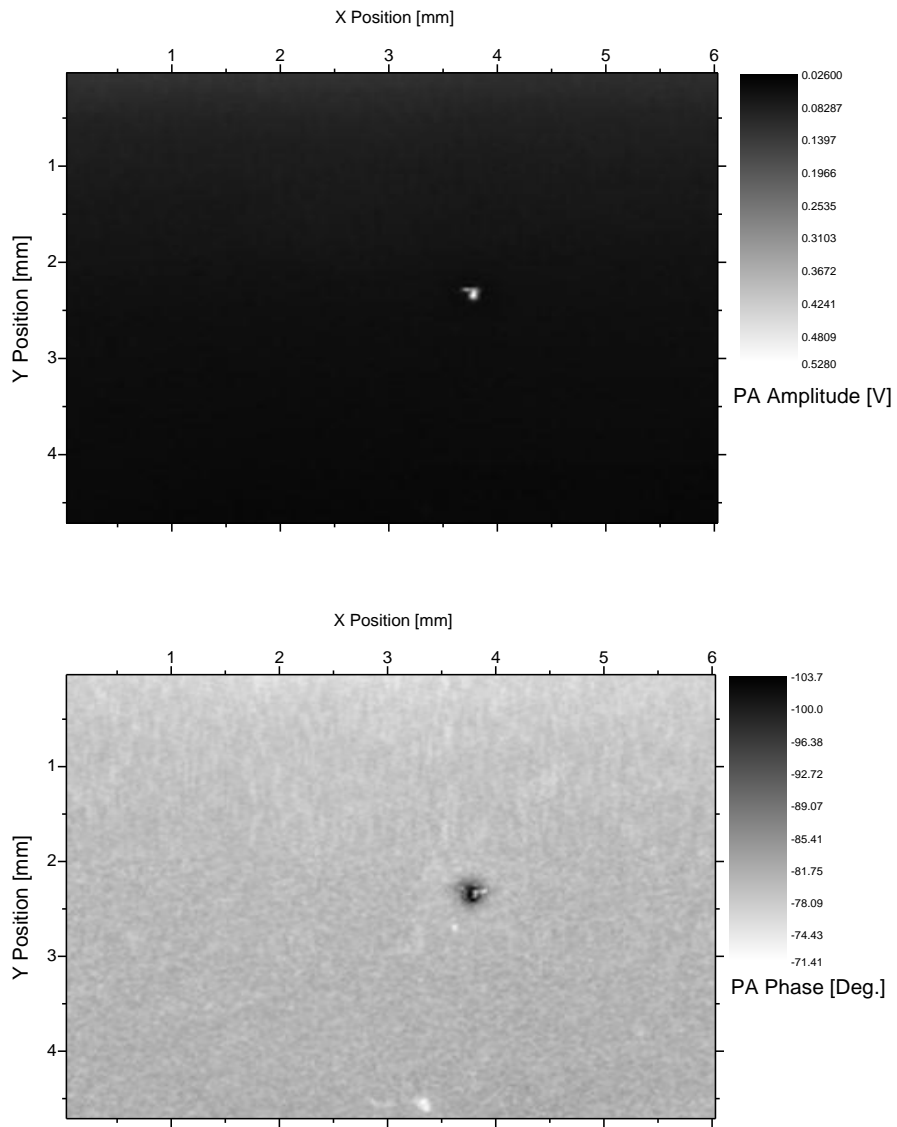


Figure 5.20: Photoacoustic Amplitude (upper) and Phase (lower) Images of packaged IC chip. (PA sample: IC chip HN462532G_JAPAN_2G1_D with the top capping material removed; Photoacoustic System settings: modulation frequency = 70Hz, lock-in Amplifier time constant = 30ms, scanned area = 4.5 mm * 6 mm, scanning step size = 30um, scan via the back surface)

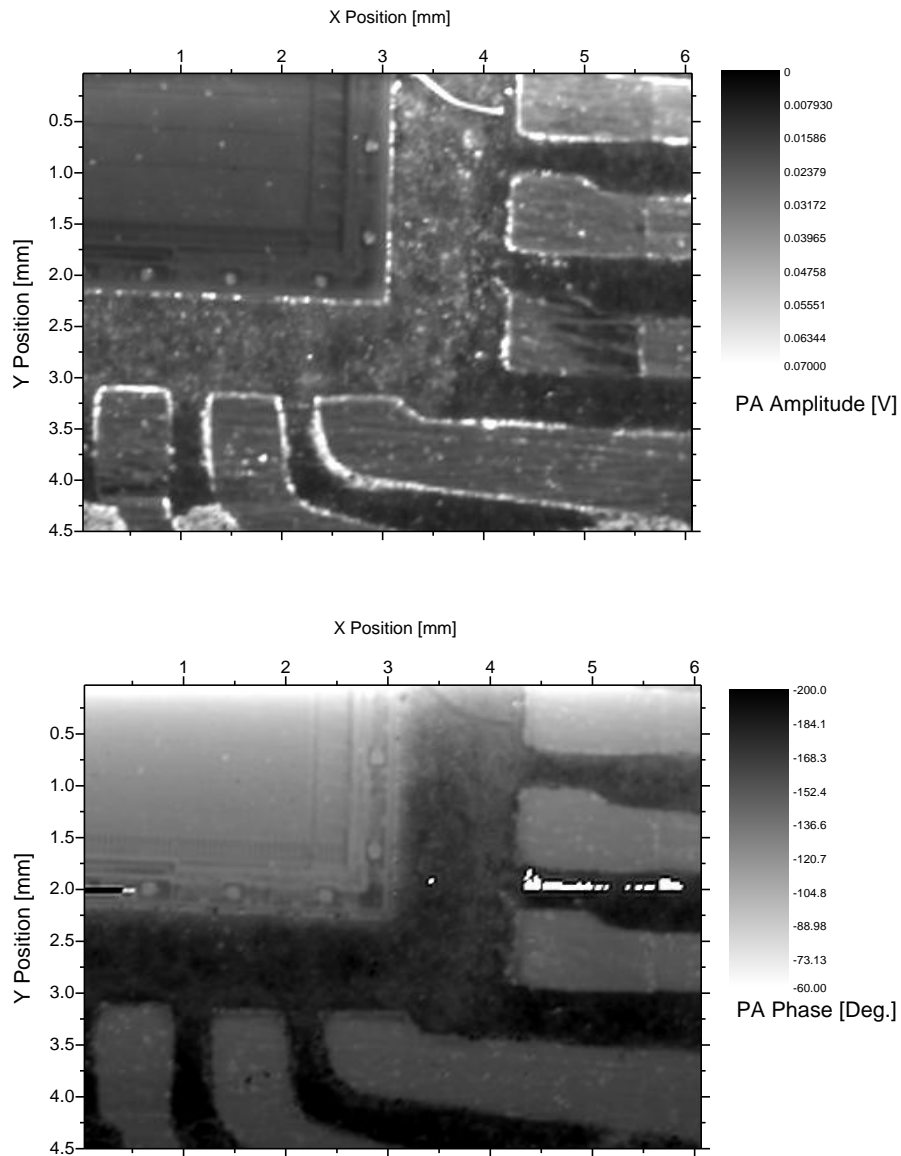


Figure 5.21: Photoacoustic Amplitude (upper) and Phase (lower) Images of packaged IC chip. (PA sample: IC chip HN462532G_JAPAN_2G1_D with the top capping material removed; Photoacoustic System settings: modulation frequency = 970Hz, lock-in Amplifier time constant = 3ms, scanned area = 4.5 mm * 6 mm, scanning step size = 30um, scan via the front surface)

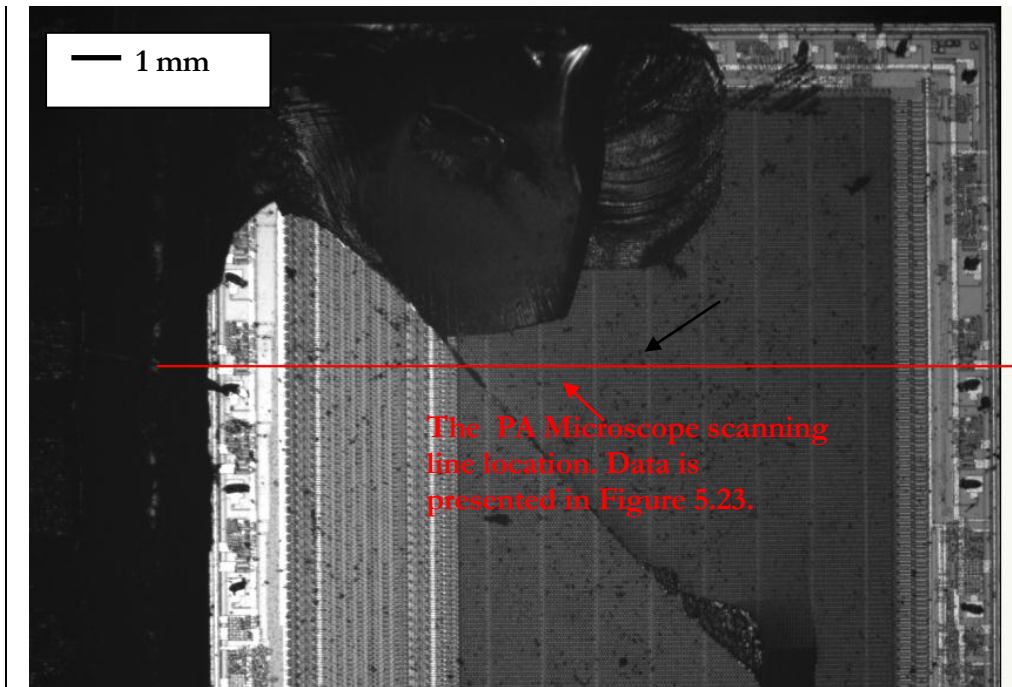


Figure 5.22: Optical Microscope image of the manually damaged HN462532G chip

Photoacoustic Microscopy has been used to characterize the shape of the subsurface delamination area, which cannot be seen by optical microscopy. The PAM modulation frequency is 970 Hz with a 1ms time constant. The scan is made on a 6mm*6mm area with a 30um step size, using air as the coupling gas. (AC coupling, normal reserves, 24db and 200mV sensitivity). As seen in Figure 5.23, both Amplitude and Phase images reveal the subsurface delamination layer, which is of several mms wide on the left side of the crack. The phase image is more sensitive to the subsurface defects and shows less interference from the dirt on the top surface. Across the sample, the IC circuit pattern can be seen clearly except for the surface damaged area on the left upper corner.

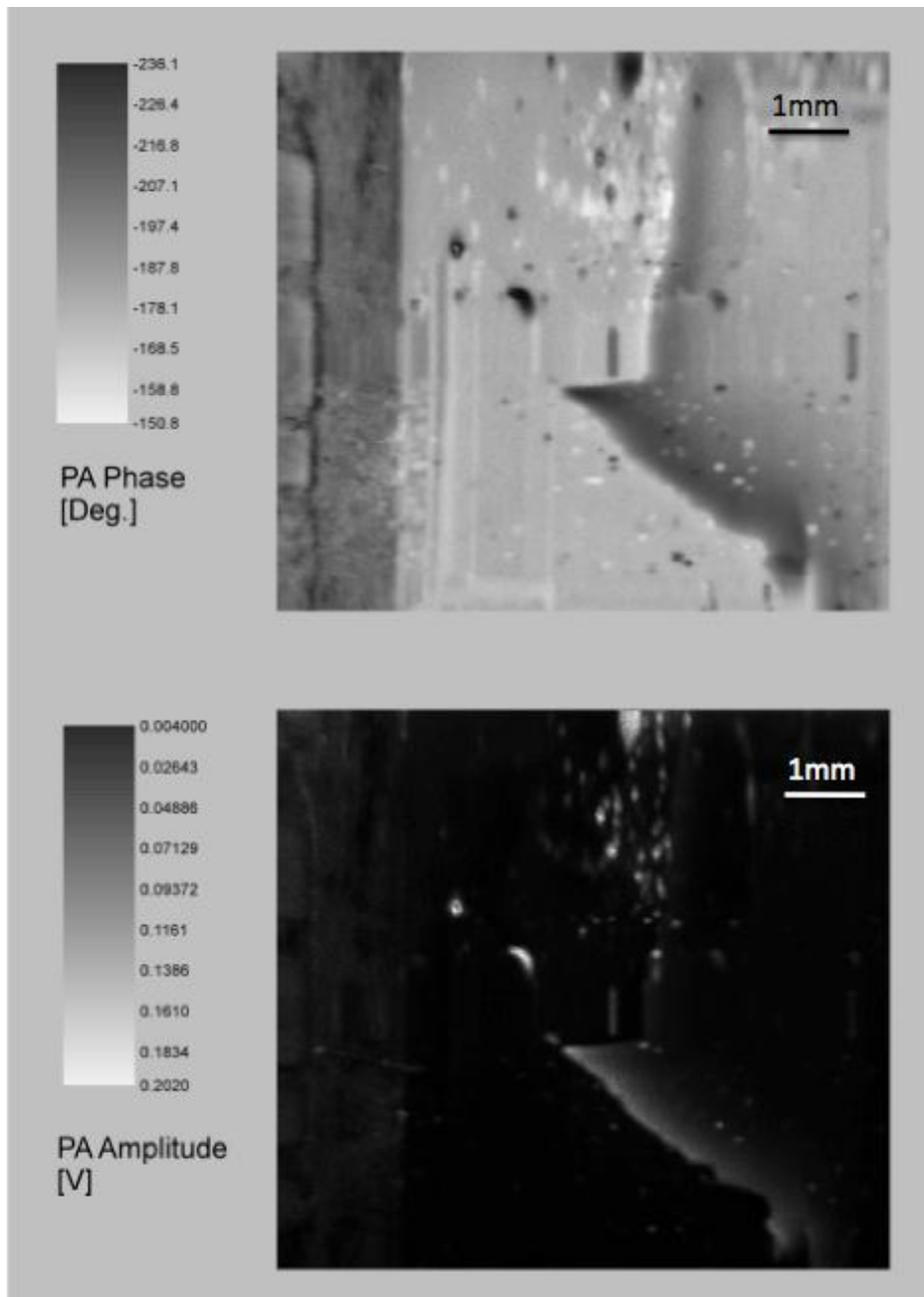


Figure 5.23: Phase and Amplitude image of manually damaged HN462532G chip

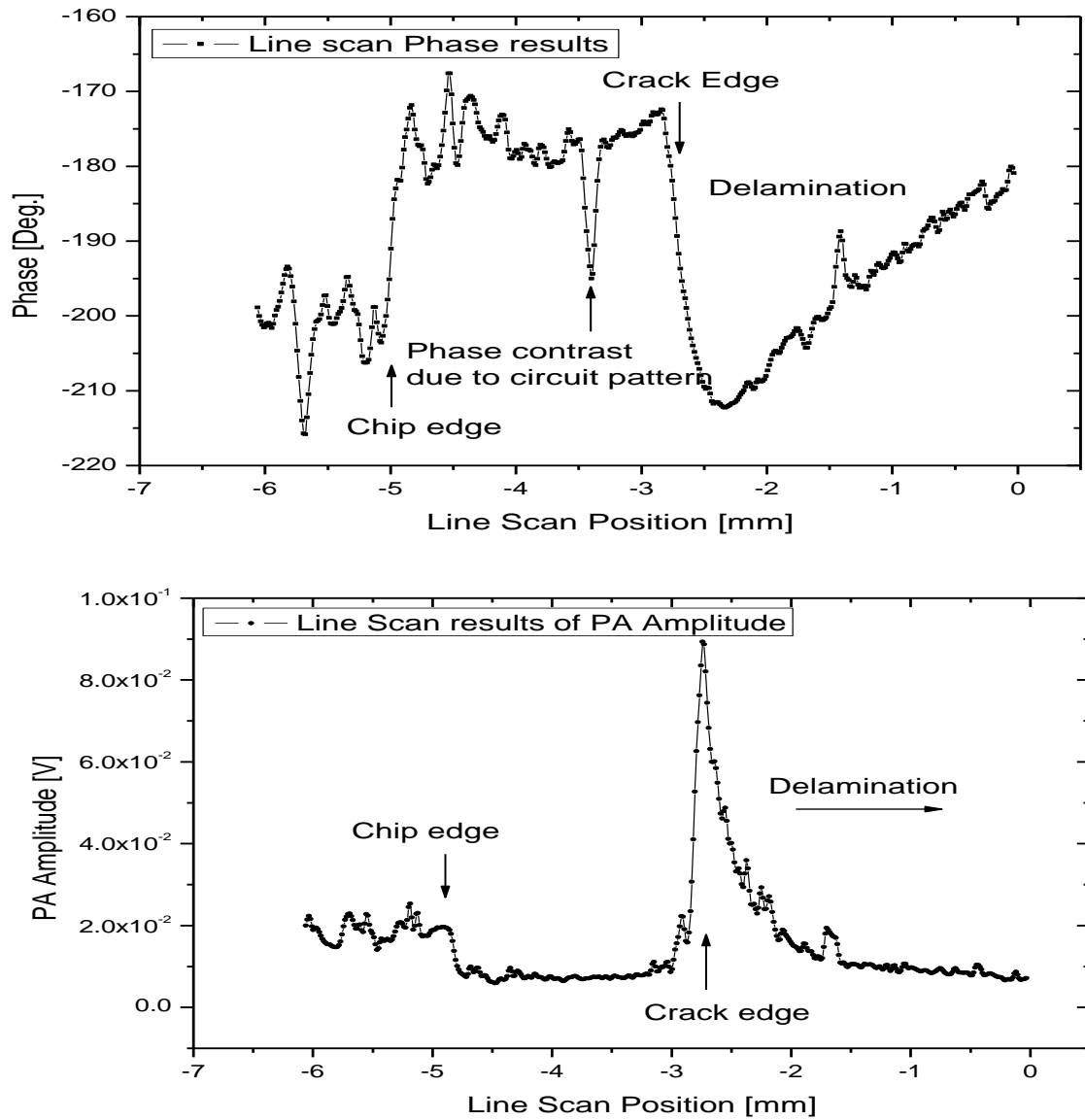


Figure 5.24: Line scanning PA Microscopy results (Upper image = Phase data; lower image = Amplitude data) at the position indicated by the red line in Figure 5.22.

Figure 5.24 shows the line scanning PA microscope result at the position indicated by the red line in Figure 5.22. As seen in both amplitude and phase plots, the delamination layer extends up to 3 mms away from the crack itself and

reaches its maximum extent at the right side of the crack. No delamination can be found on the left side of the crack. These results are consistent with the optical microscopy results.

5.5. Application 4: Photoacoustic Spectroscopy for Bandgap Defect Characterization in Semiconductor Materials

Several techniques have been developed to characterize the impurities or the defects formed deep within the energy bandgap of semiconductor materials. Optical absorption spectroscopy (OAS) is one of the most conventional methods, which measures the intensity ratio of the incident and the transmitted light. However, it has low sensitivity for certain impurities, whose absorption coefficient is below 1cm^{-1} . In such cases, the sample thickness needs to be more than a few millimeters for OAS to obtain accurate absorption spectra. An alternative metrology method is photoluminescence (PL). It has been reported that PL can detect boron and phosphorous shallow impurities, whose concentrations are as low as 1×10^{11} and $5\times 10^{10}\text{cm}^{-3}$, respectively, in silicon. [5.13]

When amplitude modulated light is incident on the semiconductor surface, optically excited free carriers are generated. These carriers then recombine through radiative or non-radiative pathways and decay to the ground state by dissipating the excess energy. The radiative re-combination process can be detected efficiently by PL method. On the other hand, non-radiative recombination also generates heat within the sample. The modulated heat creates thermal waves and elastic waves, which propagate through the sample. This signal is a photoacoustic signal, which can be measured using the PA system described in chapter 3. The PA technique is a complementary metrology tool for PL methods, as it provides a direct monitor of the *non-radiative* recombination channels within the semiconductor materials. For large-scale integrated circuits and opto-electronic device fabrication, the non-radiative centers, will result in the

degradation of devices. It is thus very important to understand such electronic transitions.

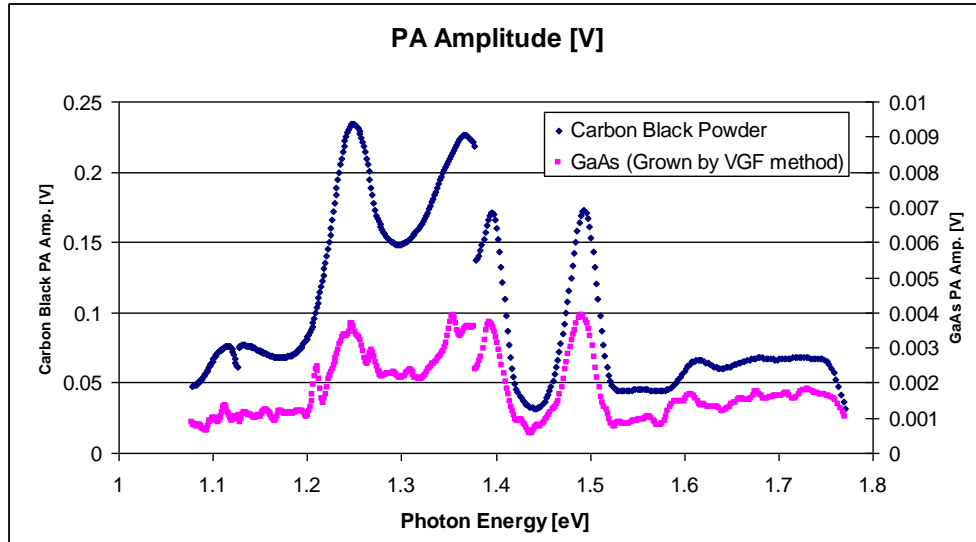


Figure 5.25: A typical PA Amplitude Spectroscopy result for Sample 1: Carbon Black Powder and Sample 2: GaAs wafer grown by VGF method (Light source: Arc lamp 700 nm ~ 1500 nm, PA cell filled with Air, Modulation frequency = 70 Hz, wavelength scan step size = 1 nm, 4 microphones activated, averaged spectrum of 5 scans, Lock-in amplifier setting: Float coupling, sensitivity = 1V, time constant = 500 ms)

In addition, the photoacoustic technique is sensitive enough to measure very small optical absorption coefficients in highly transparent media. This gives PA methods a big advantage while measuring the absorption spectra of thin film structures. It has been reported that the PA method can detect a thin layer of amorphous Se film, whose thickness is less than 20 nm and whose absorption coefficient is as low as 0.1cm^{-1} . [5.14] It is very possible for the PA system described in chapter 3 to detect impurities and defects of quite low concentrations.

As shown in Figure 5.25, a photoacoustic spectrum in spectroscopy mode (PAS) for carbon black powder is recorded with the same settings as for a vertical gradient freeze (VGF) grown GaAs sample. This includes using the same modulation frequency, the same time constant setting for the lock-in amplifier and the same photonic interval. The carbon black spectrum is used to remove the fingerprint of light source intensity from the GaAs PA spectroscopy results. Due to its significantly higher optical absorption coefficient, the PA signal amplitude from the carbon black powder is about 45 times greater than that from GaAs. However, the signal to noise ratio (SNR) for the VGF GaAs spectrum is still quite usable. Its PA spectrum follows a trend similar to that of the carbon black sample, this being dominated by the intensity distribution curve of the arc lamp light source. No extra filtering has been applied to the above data to reduce the noise. This is a direct proof showing that the SNR performance of our PA system is good enough to perform the (sub)-bandgap characterization even for semiconductor bulk material.

As described in previous section, by dividing the PAS amplitude values for GaAs samples by those for the carbon black powder, the PAS Amplitude results can be normalized. The normalized PA spectra for two types of GaAs wafers, grown by the Vertical Gradient Freeze (VGF) method and Liquid Encapsulated Czochralski (LEC) methods, respectively, are shown in Figure 5.26. For both GaAs spectra, the PA amplitude increases dramatically once the incident photon energy is above 1.4 eV. This is due to the abrupt increase of optical absorption near and above the bandgap energy and band-to-band transitions occur with a high probability. [5.15] According to Figure 5.26, the bandgap energy for both characterized GaAs samples is about 1.4 eV, which is consistent with the data ($E_g \sim 1.43$ eV) listed in Table 3.1.

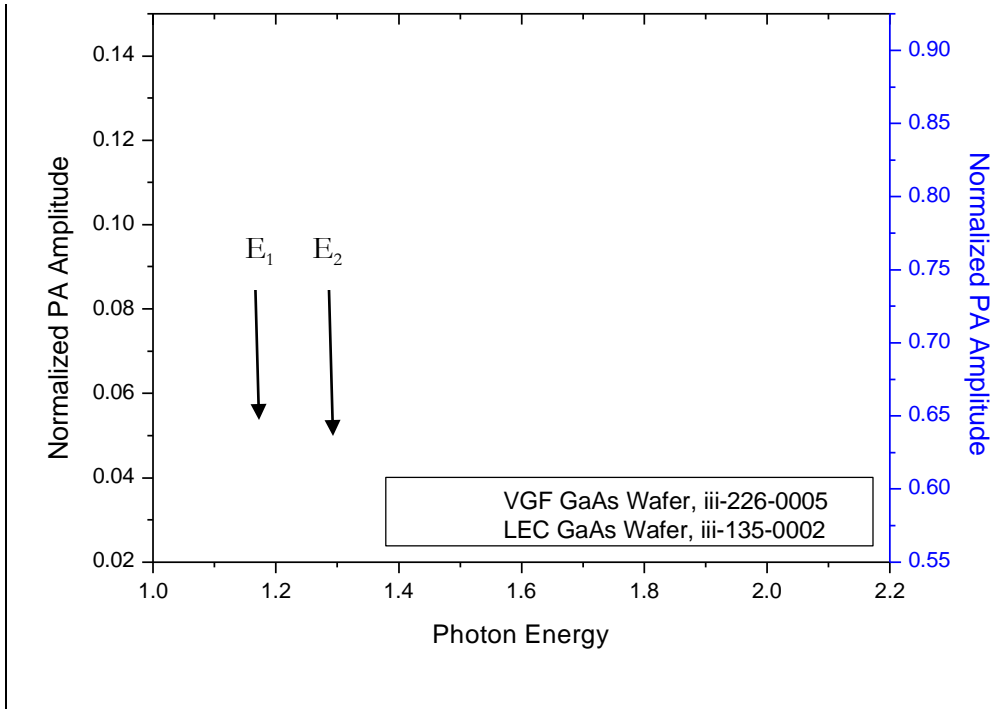


Figure 5.26: Normalized PAS Amplitude spectra are presented for two types of GaAs wafer grown by the VGF and LEC methods, respectively. (Samples: VGF GaAs wafers, 4 microphones activated, PA cell filled by Helium Gas, modulation frequency = 70 Hz, time constant for lock-in amplifier = 300 ms, averaged result of 5 PA spectra, 30 point adjacent averaging is applied for noise reduction; For Dataset iii-135-0002, sample: LEC GaAs wafer from MCP Tech, modulation frequency = 43 Hz, PA cell filled by air, lock-in amplifier setting: time constant = 3 s, sensitivity = 100 mV, AC coupling, Ground, Normal reserve, Negative Edge Triggering, with reduced PA cell volume (1/2 of its original size).)

As shown in equations 2.34 and 2.35, the PA Amplitude data below the bandgap can accurately reflect the physical properties of the gap states, such as deep impurity and defect levels. For both GaAs PA spectra, there appear to be two defect levels below the bandgap energy, $E_1 \approx 1.17$ eV and $E_2 \approx 1.3$ eV, as indicated by arrows in Figure 5.26. The defect level of E_2 seems to be more obvious in GaAs LEC spectrum and its contribution to PA signal is slightly bigger. In addition, there is a broad peak in LEC GaAs spectrum, which is extending up to ~ 1.35 eV. This broad feature overlaps the peak position of E_1 . Ikrai *et al.* have also reported this phenomenon [5.16] and they suggest that this

“D-band” might be due to the electron transition involving the EL2 defect level in the GaAs substrate.

To determine the nature of these band gap defects in detail is beyond the scope of this thesis, and will require further study in the future combining PAS with e.g. low-temperature Deep Level Transient Spectroscopy (DLTS) characterization.

SYNCHROTRON X-RAY TOPOGRAPHY AND MICRO RAMAN
STUDY ON LASER MICRO MACHINING

6 Synchrotron x-ray topography and micro Raman study on laser micro-machining

The major portion of the content of this chapter was published in the journal, *Semiconductor Science and Technology* in 2007. The DOI number is 10.1088/0268-1242/22/8/024. The permission to include this article in my thesis has been granted by the publisher and the proof or permission is included in an appendix at the end of this thesis.

6.1 Introduction

Indium phosphide (InP) is a very important III-V compound semiconductor material for high speed optoelectronic applications. Using the different optical reflectivity between laser induced amorphous and crystalline phase structures on the same InP substrate, high density optical memory recording systems can be manufactured and this has drawn great attention in the past few years. Compared with conventional nanosecond (ns) laser methods, material micro-processing with ultra-fast femtosecond (fs) laser pulses can lead to improved surface morphology and a reduction in the heat-affected zone (HAZ) due to the absence of direct coupling of the laser energy into the thermal modes of the material during irradiation. The quality difference of substrates machined with different laser pulse durations, in terms of collateral damage to the crystal structure, residual strain and localized changes in optical, mechanical and electronic properties, has been demonstrated by many groups.

Typically, non-destructive studies on laser machined samples have been limited to the top surface using optical (OM), scanning electron (SEM) [6.1] and atomic force microscopy (AFM) for surface morphology visualization [6.2], micro-Raman spectroscopy (μ RS) for stress analysis [6.2, 6.3] and Auger electron spectroscopy (AES) for chemical modification [6.4]. Thus, according to most of the published work, in order to obtain the crystal structure and strain information tens of microns under the laser machined surface, the samples have to be destructively cleaved or further prepared by special techniques e.g. focused ion beam (FIB) to allow access to the cross-sectional facet for analysis by techniques such as degree of polarization (DOP) photoluminescence (PL) [6.5], or transmission electron spectroscopy (TEM) [6.6].

Since the threshold fluence dependency of irradiated semiconductors on the number of laser pulses can be described by a fatigue damage mechanism, it becomes very important to understand the accumulated mechanical stress in the multiple-pulse laser machining process. [6.7] This stress can be induced by the thermal process, top surface chemical compositional changes and the crystal structure distortion underneath.

In this chapter, I present a totally non-destructive 3D analysis of strain induced by femtosecond and nanosecond laser machining using white beam synchrotron x-ray topography (SXRT) and high resolution micro-Raman Spectroscopy (μ RS). Depth profiling and cross section images of strain fields right through the processed InP wafer have been obtained. Both uniaxial and shear stress values from the top surface and the underlying crystal have been calculated based on the Raman peak shifts and the orientation contrast of SXRT images. To the best of this author's knowledge, this is the first time that white beam synchrotron x-ray topography (SXRT) has been applied to the strain analysis of laser-machined samples.

The method of strain field imaging using SXRT is based on two contrast mechanisms: (1) extinction contrast: the difference in reflecting power between perfect and imperfect crystal regions and (2) orientation contrast: the non-uniform diffracted imaging of distorted crystal regions whose misorientation exceeds the divergence of the synchrotron beam, ~ 0.06 mrad vertically in this study. The SXRT sensitivity to strain magnitude is estimated to be at least of the order of 6×10^{-5} and a spatial resolution of about $5 \mu\text{m}$ can be easily achieved [6.8]. Unlike the aforementioned strain characterization techniques used on laser machined samples, SXRT is a genuinely nondestructive analysis tool sensitive to the subsurface features. By selecting different diffraction images on the recording film and varying the corresponding X-ray penetration depth, a 3D strain field profile right through from the top-side to back-side can be built up. Using a transmission section topography (TS) geometry, a set of cross-section images of the strain distribution on different crystal planes can be obtained in a few minutes. SXRT has already been successfully used to characterize the defects in single crystal Si, thermal processing induced strain fields in packaged Si integrated circuits and solder bump process induced stress distributions in Si substrates [6.9-6.11].

One drawback to be noted at this stage is that it is normally very difficult to determine the sign of the strain which produced the contrast on the recording film and only the magnitude of the strain can be calculated based on SXRT results. Therefore, in order to calculate the exact stress value, obtain a high-resolution stress line profile (less than $1 \mu\text{m}$ spatial resolution) and also to analyze the chemical surface modification, micro-Raman Spectroscopy (μRS) has also been used as a complementary tool in this study.

6.2 Experimental details

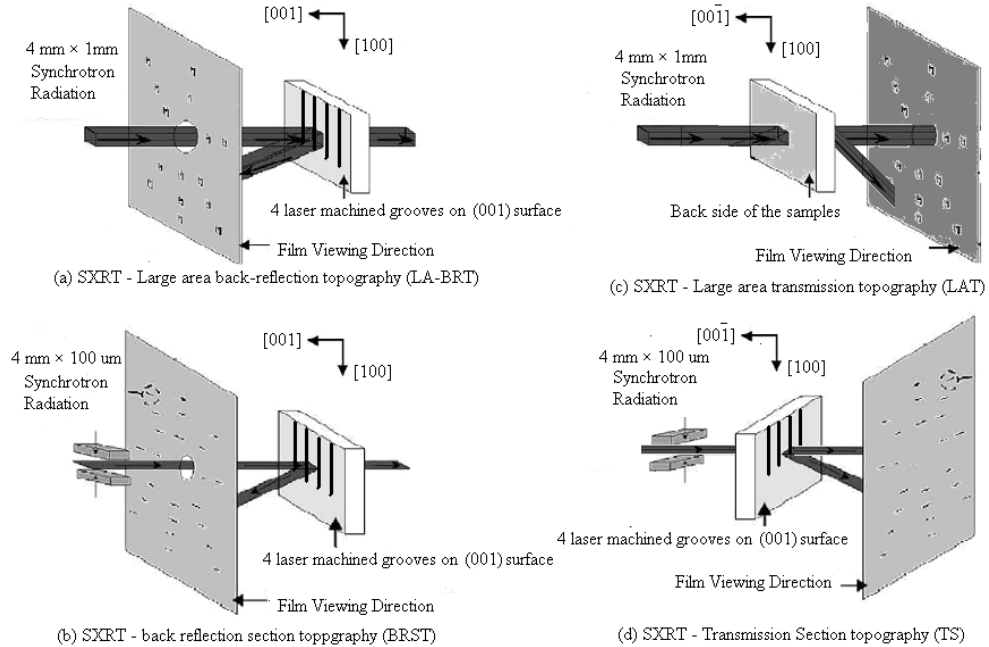


Figure 6.1. (a) Schematic details of large area back-reflection topography (LABRT) geometry, (b) back-reflection section topography (BRST) geometry, (c) large area transmission topography (LAT) geometry and (d) transmission section topography (TS) geometry

The micro-machined samples are prepared with a commercial, regeneratively amplified Ti:sapphire laser operating at a centre wavelength of 800 nm at a 1 kHz repetition rate. The laser beam was focused on the sample surface by a 5 \times -microscope objective to a spot size of $5.5 \pm 0.5 \mu\text{m}$ (Gaussian beam radius at $1/e^2$ intensity fall off). Inside a small vacuum chamber, four grooves were machined on the (001) surface of one n-InP substrate (S doped $\sim 10^{18} \text{ cm}^{-3}$) along the [100] direction with pulse durations of approximately 130 femtoseconds and 8

nanoseconds, respectively. The nanosecond pulse is obtained from the same laser as the 130 fs pulse by blocking the seed pulse to the amplifier and bypassing the compressor. With a beam linearly polarized perpendicular to the cutting direction, pulse energies of 1.0 and 0.35 μJ were utilized at a machining rate of 500 $\mu\text{m/s}$, as shown in Table 6.1. This machining rate implies that approximately 10 pulses are incident on the sample in each beam diameter length, making this a multi-pulse process.

The X-ray topography measurements were performed at HASYLAB-DESY, Hamburg, Germany, utilizing the continuous spectrum of synchrotron radiation from the DORIS III storage ring bending magnet source. The ring operated at a positron energy of 4.45 GeV and at typical currents of 80–150 mA. The Laue/Bragg patterns of topographs were recorded on Geola VRP-M Holographic films, which have an emulsion grain size of about 40 nm. Four experimental arrangements, large area back-reflection topography (LABRT), back-reflection section topography (BRST), large area transmission topography (LAT) and transmission section topography (TS), as illustrated in Figure 6.1, have been used to obtain depth profile information and cross-section images of the strain fields.

Micro-Raman measurements were conducted in the backscattering geometry using a 488 nm Ar^+ laser excitation at room temperature on a Jobin Yvon LabRam HR800 μRS system equipped with a liquid nitrogen cooled CCD detector (wavenumber resolution = 0.4 cm^{-1}). With an Olympus 100 \times microscope objective, the laser was focused on the sample surface to a diameter of 1 μm . Line scanning with 1 μm step size was performed automatically on a motorized X-Y microscope stage whose step resolution is 0.1 μm and reproducibility is 1 μm . 20 seconds integration time was selected and 3 Raman

spectra from the same probing position were averaged to increase the signal to noise ratio (SNR).

6.3 Results and discussion

6.3.1 SXRT Large area back reflection (LABRT) results

As shown in Figure 6.2, the (0 2 6) large area back-reflection topograph (LABRT), of four laser-machined grooves can be observed as 4 stripes of reduced intensity along the [100] direction, where black corresponds to enhanced x-ray diffraction intensity. The two femtosecond laser machined grooves can be easily identified with one extra dark line at the centre of the each stripe.

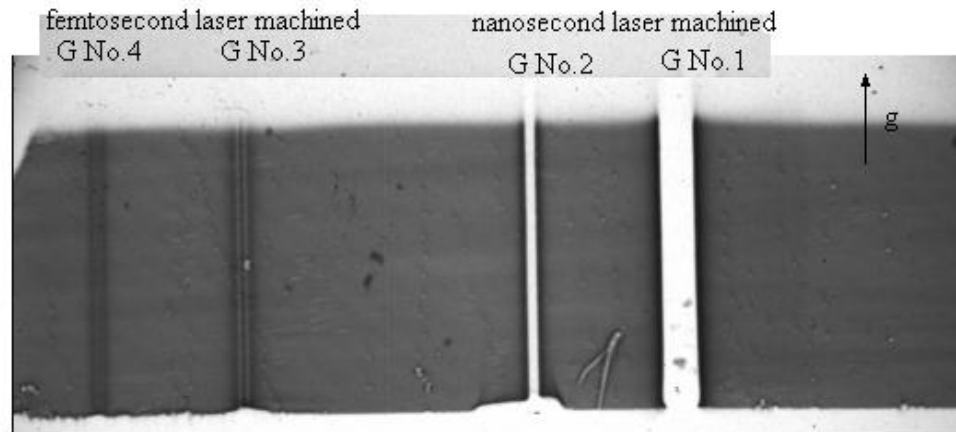


Figure 6.2: Typical SXRT LABRT images for four laser-machined grooves: (0 2 6) diffraction image. The diffraction vector g is indicated on the image.

The kinematic penetration depth (t_p) of the x-rays in each SXRT diffraction image, which is measured perpendicular to the surface, can be calculated using the equation:

$$t_p = \frac{1}{u\left(\frac{1}{\sin(\alpha_i)} + \frac{1}{\sin(\alpha_f)}\right)} \quad (6.1)$$

where $\mu(\lambda)$ is the linear x-ray absorption coefficient at wavelength λ , α_i and α_f are the incidence and exit angles with respect to the sample surface [6.12]. Therefore, the probe depth of the (0 2 6) diffraction image can be estimated to be 2.78 μm , which is far deeper than the probe depth of the Raman measurement (~ 50 nm with 488 nm laser excitation).

Two possible mechanisms can be used to explain the reduced intensity contrast for all four laser machined grooves shown in Figure 6.2. The extinction contrast mechanism suggests that the reduced intensity around the grooves may represent greatly reduced x-ray diffractive capability due to the presence of a thick x-ray absorbing re-solidified surface layer, which comprises a high percentage of amorphous or polycrystalline InP. However, the cross sectioned transmission electron microscope (XTEM) results for the same sample presented by another group [6.6] indicate that the re-solidified layer thickness only varies from 200 nm to 500 nm, which is far less than the x-ray penetration depth calculated using equation 6.1. Additionally, the width of the white low x-ray intensity region is much bigger than the groove width or the re-solidified layer width across the grooves (from 10-20 μm measured by XTEM). Therefore, this image can only be explained by a dominant orientation contrast mechanism, resulting from the overlap and/or separation of an inhomogeneously diffracted x-ray beam. The width of the reduced intensity stripes on the SXRT film should be equal to the SXRT detectable width of shear strained InP crystal 2.78 μm below the top surface. Therefore, according to Figure 6.2, the width of the distorted underlying crystal about the 4 grooves from No.1 to No.4 can be estimated to be 64 μm , 32 μm , 28 μm and 24 μm respectively, as listed in Table 6.1. With the same laser pulse energy, laser machining with shorter pulse duration leads to smaller strained regions about the grooves.

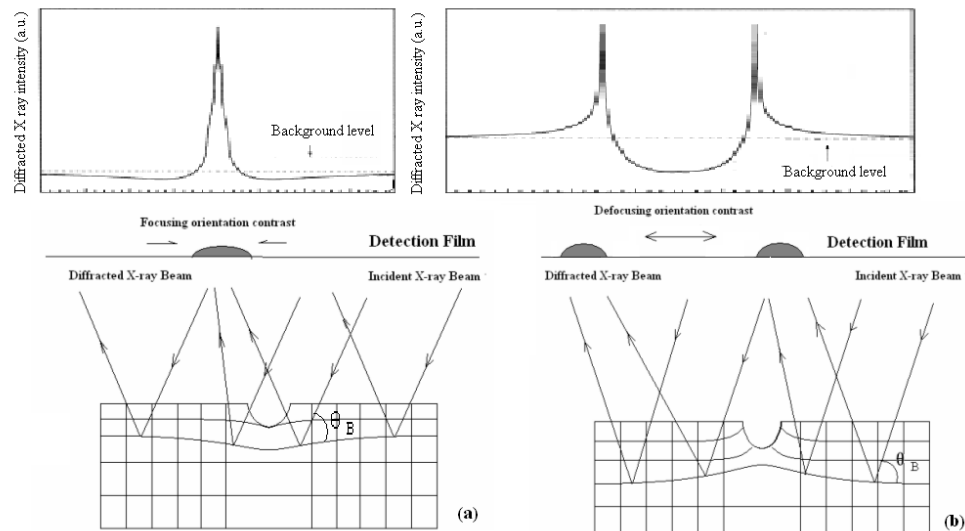


Figure 6.3: Schematic of ‘focusing’ (a) and ‘defocusing’ (b) mechanism of diffraction x-ray intensity line profile with two oppositely shear strained areas associated with femtosecond and nanosecond laser machining respectively.

In addition, two totally different diffracted x-ray line profiles, termed here as ‘focusing’ and ‘defocusing’ phenomena, are observed across the fs and ns laser machined grooves respectively. Similar to SXRT orientation contrast for edge dislocations [6.13], these phenomena can be explained by the opposite sign of $(0\ 0\ 1)$ crystal plane Bragg angle variation ($\Delta\theta_B$) with respect to the incident direction of the synchrotron x-ray beam in the shear strained area. Referring to figure 6.3(a), the femtosecond laser machining process modified the subsurface $(0\ 0\ 1)$ crystal plane such that the diffracted x-ray intensity from the distorted region is ‘focused’ to the groove center, shown as a symmetric white-black-white sandwich structure contrast in the LABRT image. In contrast, for the nanosecond laser machined trenches, as shown in figure 6.3(b), the diffracted x-rays from the shear strained area is ‘defocused’ to the groove sides, resulting in a wide white stripe structure with enhanced intensity at the edges along the $[1\ 0\ 0]$ direction. According to the ‘defocusing’ orientation contrast observed, the subsurface $(0\ 0\ 1)$ crystal planes

tilt upwards and tend to align perpendicularly to the laser machined surface when approaching the groove centre. One possible reason could be that during the time between two nanosecond laser pulses, which is longer than the time need for thermal diffusion deep into the bulk, a heat affected zone (HAZ) is built up by the excess heat induced by the initial laser pulse. The (0 0 1) crystal planes in the HAZ are deformed along the temperature gradient, which is normal to the laser machined surface. A tensile strained area could be expected in the underlying crystal substrate after the nanosecond laser machining process. In contrast, the (0 0 1) crystal planes under the femtosecond laser machined grooves are simply compressed downwards and leave a compressively strained area below the groove centre, as shown in Figure 6.3(a). In this case, non-thermal melting occurs. Similar imaging results of shear strain distribution have been observed using a destructive probing method (degree of polarization photoluminescence technique) on the cleaved InP facet across all four laser machined grooves, where the degree of polarization (DOP) signal, associated with linear strain, and the rotated degree of polarization (ROP) signal distribution, which is directly related to the shear strain and lattice distortion direction, have been found to be of opposite sign beneath the fs and ns laser machined grooves [6.5]. Although the extinction contrast mechanism may have some minor impact on the LABRT images especially for the fs laser machined case where dislocations along groove sides and twins at the center are observed by XTEM [6.6], the dominant orientation contrast mechanism still clearly indicates the opposite sign of crystal distortion in the two cases. This conclusion is also confirmed by Figure 6.6, the simulation of SXRT transmission section topography (TS) images.

6.3.2 SXRT back reflection section topography (BRST) results

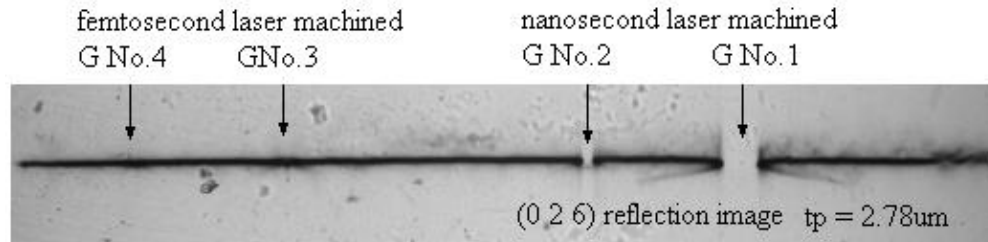


Figure 6.4: The (0 2 6) SXRT back reflection section topography (BRST) of four laser-machined grooves with x-ray penetration depth (t_p) of 2.8 μm .

One of the advantages of SXRT back reflection section topography is its ability to provide nondestructive depth profiling of a thin slice of InP crystal across the four laser machined grooves perpendicular to the top surface. By carefully comparing the topographs and the corresponding x-ray penetration depths for different diffracted images, the depth of imperfect crystal region can be estimated. As shown in Figure 6.4, the broken line features (defocusing orientation contrast) introduced by nanosecond laser machining process can be found on this BRST image with $t_p=2.8 \mu\text{m}$ and all the other diffracted images on the recording film. The corresponding x-ray penetration depth varies from 1.5 μm for 1 1 5 diffraction to 22.5 μm for 3 3 13 diffraction. Therefore, the magnitude of shear strained depth induced by nanosecond laser machining is greater than 20 μm . At the positions of G No.3 and G No.4 in Figure 6.4, the SXRT misorientation contrast of trifurcate shape related to the distorted InP crystal under femtosecond laser machined grooves is not obvious, which indicates much smaller shear strain values about the fs machined grooves compared to the nanosecond processed counterparts. Among all the studied diffraction images, the strongest SXRT misorientation contrast about G No.3 and G No.4 can be found in the 0 2 6 diffraction, which suggests that the most imperfect crystal region induced by fs laser machining is about 3 μm below the top surface.

6.3.3 Transmission section results and simulation

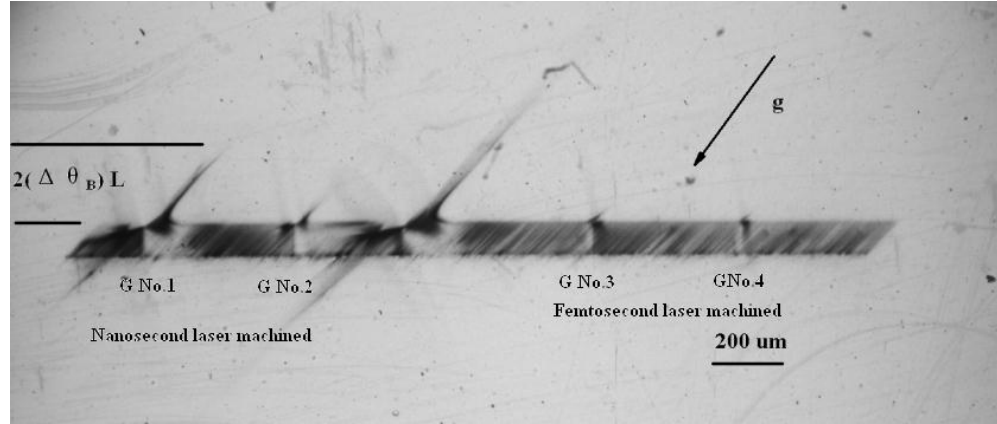


Figure 6.5: The $\bar{2}\bar{2}0$ SXRT Transmission Section Image of laser machined InP

As shown in figure 6.5, the $\bar{2}\bar{2}0$ SXRT transmission section (TS) image, four pairs of symmetric back ‘tails’ can be observed around all laser machined grooves. This contrast can be seen when the misorientation of crystal planes exceeds the synchrotron x-ray beam divergence, which is 0.06 mrad vertically at the F1 beamline in HASYLAB. The black tail length, corresponding to the magnitude of orientation contrast shift (ΔS), can be calculated as [6.14]:

$$\Delta S = 2(\Delta\theta_B)L \quad (6.2)$$

where $\Delta\theta_B$ is the maximum observed shift of the Bragg angle of the severely strained crystal region and L is the distance between the sample and film (93 mm in this case).

$\Delta\theta_B$ comprises lattice dilatation ($\Delta d/d$) parallel to the Burgers vector (g) and the component of the tilt angle α of the lattice planes around $[0\ 1\ 0]$, the normal to the plane of X-ray incidence, and this can be expressed as [6.14]:

$$\Delta\theta_B = \frac{\Delta d}{d} \tan(\theta_B) + \alpha \quad (6.3)$$

Since white beam radiation can provide a diffracting wavelength for any dilated plane, the dilatation components $\frac{\Delta d}{d} \tan(\theta_B)$ can be ignored and $\Delta\theta_B$ is equal to tilted angle α , which is directly related to the shear strain γ_{xy} [6.15].

$$\gamma_{xy} = \Delta\theta_B \approx \alpha \quad (6.4)$$

The magnitude of shear stress (δ_{xy}) can be quantitatively estimated using

$$|\delta_{xy}| = E |\gamma_{xy}| \quad (6.5)$$

where $E = 61.1\text{GPa}$, the Young's modulus of InP [6.16].

Using the orientation contrast shift (ΔS) measured in figure 6.5 and equations 6.2 and 6.3, the maximum distorted angle of the $\bar{2}\bar{2}0$ lattice plane about the laser machined grooves from No.1 to No.4 has been estimated to be 1.74 mrad, 0.54 mrad, 0.35 mrad and 0.24 mrad, respectively. The magnitude of crystal misorientation resulting from femtosecond laser machining is far less than the comparable nanosecond process with the same laser pulse energy. With reduced laser pulse energy from 1 μJ to 0.35 μJ , the shear stress value about the grooves decreases from 106.2 MPa to 33.4 MPa for the nanosecond laser process and from 22.2 MPa to 14.1 MPa for the femtosecond processes, as listed in Table 6.1.

Additionally, as shown in Figure 6.5, the orientation contrast induced black tail, which extends upwards on the right hand side of the nanosecond laser machined grooves at positions G No.1 and 2, extends downwards on the same side of the femtosecond grooves at positions G No.3 and 4. It confirms that the region

where the crystal planes are downward misoriented for the femtosecond laser machined samples become upward misoriented for the nanosecond machined samples and vice versa, as illustrated by figures 6.3(a) and 6.3(b), respectively.

To further confirm the opposite sign of the distorted crystal planes underneath the machined grooves, two typical TS images are simulated for grooves No.3 and No.1 with using the Matlab® simulation suite employing the methods of [6.17] for the orientation contrast mechanism. The simulation is based on the parameters calculated above, such as the strained region width and the maximum distorted angle of the $\bar{2}20$ lattice planes. The bending directions for both fs and ns cases are assumed to be the same as the predictions shown in Figure 6.3. To simplify the simulation, only a single distorted (0 0 1) crystal plane several micrometers below the surface has been considered. The distorted crystal planes on either side of the laser-machined grooves are separated by the groove width of 4 μm . As shown in Figure 6.6(a) and 6.6(b), the (0 0 1) plane misorientation magnitude $\Delta\theta_B$ is assumed to increase more rapidly when approaching the grooves' center and is arbitrarily described by a function of distance Y measured from the center of the grooves:

For the nanosecond laser machined groove #1:

$$\Delta\theta_B(Y) = 0 \quad \text{when } |y| > 34 \text{ or } |y| < 2 \quad (6.6a)$$

$$\Delta\theta_B(Y) = -\Delta\theta_{B_{MAX}} \left(1 - \sqrt{\cos\left(\frac{34 - |Y|}{64}\right)\pi}\right) \quad \text{when } 2 < |y| < 34 \quad (6.6b)$$

For the femtosecond laser machined groove #3:

$$\Delta\theta_B(Y) = 0 \quad \text{when } |y| > 16 \text{ or } |y| < 2 \quad (6.7a)$$

$$\Delta\theta_B(Y) = -\Delta\theta_{B_{MAX}} \left(1 - \sqrt{\cos\left(\frac{16-|Y|}{28}\right)\pi}\right) \quad \text{when } 2 < |y| < 16 \quad (6.7b)$$

where the positive value of $\Delta\theta_B$ represents the clockwise rotation along the [100] direction and the Y axis is defined along the [010] direction.

This simulation method is based purely on orientation contrast and can be applied to any diffraction images observed on the detection film. Briefly, a set of crystal planes (h k l), which give the h k l diffraction image on the recording film, are represented by plane normal \vec{B} and distorted around the [100] axis \vec{A} by $\Delta\theta_B(y)$. The resulting vector \vec{C} can be calculated as:

$$\vec{C} = \vec{B}_A + \vec{A} \times (\vec{B} - \vec{B}_A) \frac{\sin(\Delta\theta_B(y))}{A} + \cos(\Delta\theta_B(y))(\vec{B} - \vec{B}_A) \quad (6.8)$$

$$\vec{B}_A = \frac{\vec{A} \cdot \vec{B}}{A^2} \vec{A} \quad (6.9)$$

Due to the SXRT TS experimental setup, the whole crystal is then rotated around the [010] axis \vec{D} by 13° in order to image reflections of interest. The distorted crystal plane [h k l] is therefore rotated to a new direction \vec{E} [h_r k_r l_r] to reflect the incident synchrotron x ray beam along the [0 0 1] direction.

$$\vec{E} = \vec{C}_D + \vec{D} \times (\vec{C} - \vec{C}_D) \frac{\sin(13^\circ)}{D} + \cos(13^\circ)(\vec{C} - \vec{C}_D) \quad (6.10)$$

$$\vec{C}_D = \frac{\vec{C} \cdot \vec{D}}{D^2} \vec{D} \quad (6.11)$$

The angle $\theta_{r,[001]}$ between the incident synchrotron x-ray beam [0 0 1] and the reflecting crystal plane normal \vec{E} [h_r k_r l_r] is

$$\theta_{r,[001]} = \arccos\left(\frac{l_r}{\sqrt{h_r^2 + k_r^2 + l_r^2}}\right) \quad (6.12)$$

The distance r between the reflected spot and the film center for the SXRT transmission section experimental set up can be calculated as

$$r = L \tan(2\theta_{r,[001]} - \pi) \quad (6.13)$$

where L is the distance between sample and film (93 mm in this study).

Since the distorted reflecting crystal plane normal $E [h_r k_r l_r]$, incident x-ray beam $[001]$ and reflected x-ray beam should be inside the same plane, the coordinates x_r and y_r of the simulation point on the film are:

$$\begin{aligned} x_r &= \frac{h_r}{\sqrt{h_r^2 + k_r^2}} r \\ y_r &= \frac{k_r}{\sqrt{h_r^2 + k_r^2}} r \end{aligned} \quad (6.14)$$

where x_r is along the $[100]$ direction and y_r is along the $[010]$ direction.

Since $\Delta\theta_B$ is a function of the initial reflecting point position (y) on the InP sample, a set of coordinates for the final reflected points' positions on the film can be calculated and a simulated transmission section image originating from a single layer of the distorted crystal plane can be plotted, as shown in figures 6.6(c) and 6.6(d). As seen in these two figures the $\bar{2}\bar{2}0$ SXRT transmission section images show exactly the same black tail directions and lengths as predicted by the orientation contrast simulation for both ns, Figure 6.6(c), and fs, Figure 6.6(d), laser machining cases.

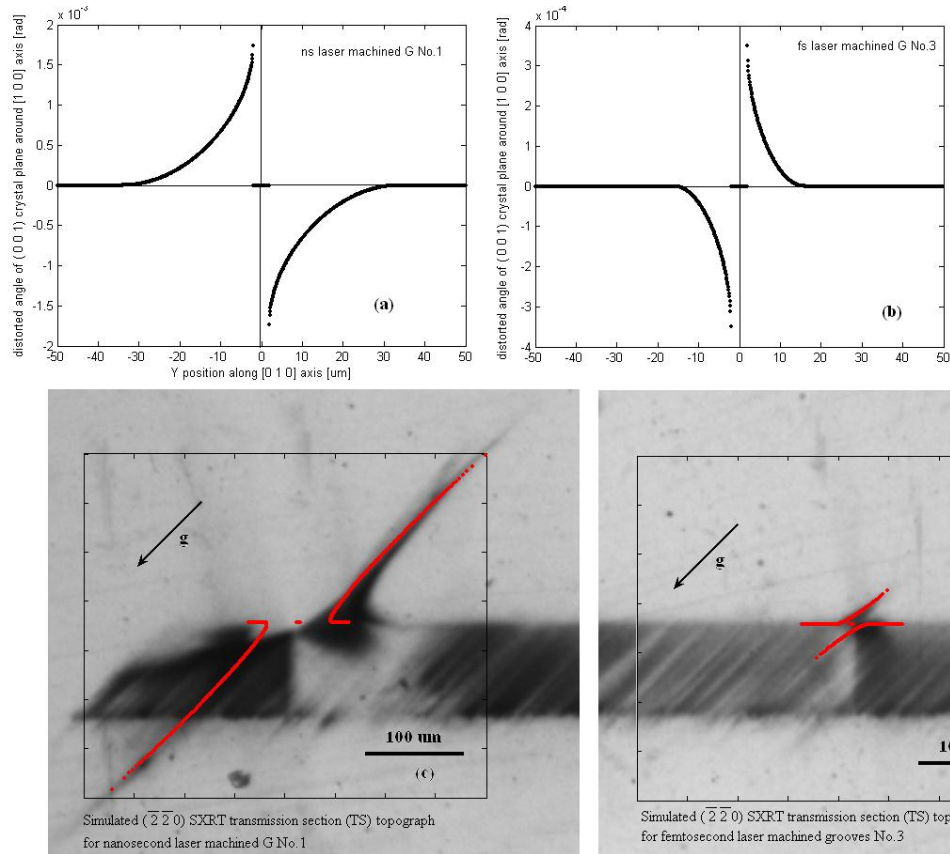


Figure 6.6: Synchrotron x-ray transmission section topography simulation: the distorted angle of (001) crystal plane around [100] axis for (a) ns laser machined G No.1 and (b) fs laser machined G No.3; Positive values represent clockwise rotation along [100] axis. The simulated $\bar{2}\bar{2}0$ SXRT transmission section images: (c) for nanosecond laser machined G No.1 and (d) femtosecond laser machined G No.3 on the backgrounds of the experimental SXRT images.

Therefore, the [001] crystal plane bending directions as hypothesised in Figure 6.3 are clearly proven by both large area back reflection and transmission section techniques. Although the real curve shape of the distorted [100] crystal plane may not be exactly the same as indicated by equations 6.4 and 6.5, we can still conclude that, with our current laser machining parameters, femtosecond laser

machining will compress the [001] crystal plane underneath while ns laser pulses will tilt the [001] crystal plane upwards and leave the same region in tension instead. In addition, the simulation shows a gradual reduction in intensity towards the end of the diffracted ‘tails’. This is also seen on the experimental film images confirming the increased misorientation as one approaches the groove centre. SXRT is proven to be a very sensitive tool for detecting crystal plane distortion after laser machining treatments. Both the magnitude and sign of the shear strain can be calculated after careful modeling.

6.3.4 *Micro-Raman Spectroscopy results*

In the reference spectrum of an untreated (100) InP sample shown as the black curve in Figure 6.7, which is obtained far away from the laser machined grooves, several first and second order Raman peaks are visible. The first longitudinal optical (LO) phonon-peak appears at approximately 339.5cm^{-1} arising from the surface depletion zone. The small LO peak intensity suggests a high carrier concentration in the InP sample, which reduces the scattering volume for the unscreened LO mode and hence the depletion depth. Adjacent to three second-order phonon peaks (2TO: 614cm^{-1} , 2LO: 679cm^{-1} and TO+LO: 648cm^{-1}), a broad feature assigned to one of the LO phonon-plasma coupled modes (LOPCM: L^+) can be observed at $\sim 594\text{cm}^{-1}$. Since the peak position of the L^+ coupled mode has been found to be very sensitive to the free-carrier density in n-InP, a carrier concentration of about $3.5 \times 10^{18}\text{ cm}^{-3}$ can be estimated by a comparison with the data in [6.18]. This is in agreement with the InP sample doping level indicated in Section 6.3. At such high doping levels, the photoexcited carrier population induced by the incident laser can be neglected and thus the L^+ peak presents a very slight blue shift with decreasing excitation laser power used in the Raman measurements. According to the InP selection rule for the back-reflection geometry employed in this study, the transverse optical (TO) phonon-peak at $\sim 306\text{ cm}^{-1}$ should be forbidden and should show a very low intensity. The

overlapping strong peak at $\sim 301.4 \text{ cm}^{-1}$ is attributed to another LOPCM mode (L^-) instead. Similar Raman spectra can be found in the literature where the 528.7 nm line of an Ar^+ laser has been used as an exciting source for the Raman measurements on heavily doped n-InP [6.18].

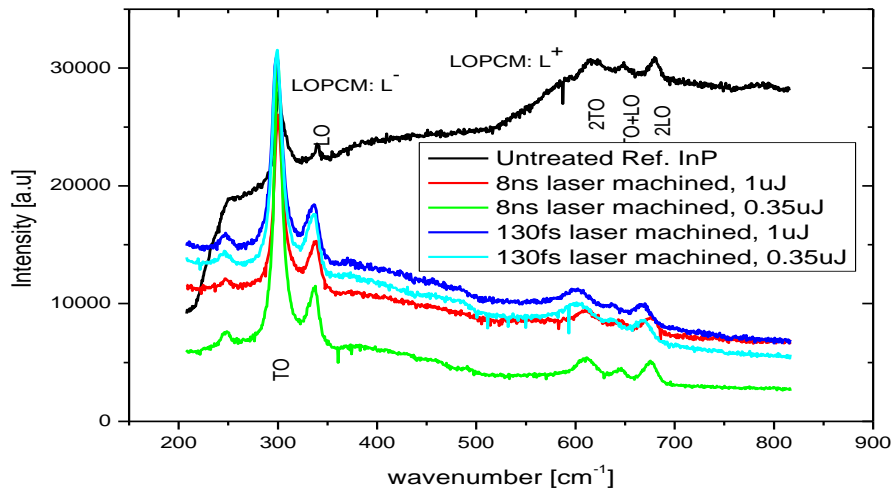


Figure 6.7: Typical Raman spectra on untreated InP (100) crystal and the surface at the centre of four different laser machined grooves.

In contrast, for all the Raman spectra measured inside the grooves, no LOPCM: L^+ mode can be seen at the high frequency range ($500 \text{ cm}^{-1} \sim 800 \text{ cm}^{-1}$), which suggests a greatly reduced free carrier concentration on the laser machined surface. Therefore, no L^- peak can be expected at the overlapping peak position of the TO mode. The two strong Raman peaks observed at approx 300 cm^{-1} and 338 cm^{-1} are now related to TO and LO modes, respectively, excited from the top surface recrystallized layer. The presence of the TO mode arises from the less than ideal backscattering geometry due to the presence of polycrystalline InP and light scattering from the rough laser machined surface. As no broad disorder activated optical phonon mode (DAO) peak can be seen at \sim

300 cm⁻¹ in any the Raman spectra across the four laser machined grooves, no amorphous InP phase has been detected in either the fs or ns laser machined surfaces with our current experimental setup [6.2]. From the coexistence of LO and TO phonon peaks and the missing LOPCM mode for all the Raman spectra obtained inside the machined areas, it appears that all the laser machined grooves investigated in this paper are covered by a thick recrystallized polycrystalline layer and the layer thickness exceeds the Raman excitation laser penetration depth. Considering the linear absorption coefficient of InP at 488 nm [6.19], the thickness of poly-InP on the top surface is more than 50 nm, which is consistent with the XTEM results on those samples [6.6]. The increased disorder of the crystallite orientation in this re-solidified layer is further supported by the fact that the full width at half maximum (FWHM) of the LO peak increases by a factor of 3 to 4 compared to the unprocessed regions.

For InP, Raman spectroscopy is also very useful for direct mechanical stress calculations. Assuming uniaxial stress, the internal stress δ is linearly related to the shift of Raman peak $\Delta\omega$ (compared with the peak position of unstressed InP at the surface):

$$\delta = g\Delta\omega \quad (6.12)$$

where a negative value of δ indicates compressive stress in the tested material and g has a value of $-0.19\text{GPa}/\text{cm}^{-1}$ for the InP LO-phonon mode [6.20]. Therefore, a positive shift in the InP LO peak reveals a compressive stress. Since the Raman signal inside the grooves is solely derived from a polycrystalline layer, it is very important to notice that the shift to lower wavenumber for the InP LO phonon peak could also be introduced by the decreased crystallite size due to the quantum confinement effect [6.21]. The measured Raman peak shift must be calibrated before the stress calculation.

As shown in Figure 6.8, which shows the FWHM line profile of the LO peak across the four laser machined grooves, the LO peaks broaden to 19 cm^{-1} for nanosecond laser machining and have an average value of 12 to 14 cm^{-1} in all irradiated areas. According to the calculation of Yu *et al.* using the spatial correlation mode for InP along the [100] direction [6.22], the InP LO peak broadens with decreasing mean diameter of the InP crystallite size and the FWHM values of 12 and 14 cm^{-1} are correlated to a lateral crystallite dimension of 4.1 nm and 3.8 nm, respectively, which will cause a downward shift of the LO peak by about -1 cm^{-1} . By assuming that the polycrystalline InP has a characteristic LO peak FWHM value of more than 11 cm^{-1} , the re-crystallized layer widths on the top surface across the four laser machined grooves from No.1 to No.4 have been measured to be $14.82\text{ }\mu\text{m}$, $9\text{ }\mu\text{m}$, $20\text{ }\mu\text{m}$ and $10\text{ }\mu\text{m}$, respectively. They are much smaller than the subsurface strained crystal width measured by the SXRT methods. The big variation of the LO peak FWHM outside the grooved area (at the scan position from $45\text{ }\mu\text{m}$ to $57\text{ }\mu\text{m}$) in Figure 6.8 (a) is correlated with the presence of droplet particles deposited by a liquid phase expulsion process observed on the XTEM images [6.6]. With our current experimental configuration, the width of the re-crystallized layer appears to increase with decreasing pulse duration and increasing pulse energy. The FWHM value variation inside the femtosecond laser machined grooves seems to be much smaller than for their nanosecond counterparts. This could be attributed to a more homogeneous distribution of polycrystal grain sizes and a smoother laser machined top surface due to the non-thermal processing with a shorter laser pulse.

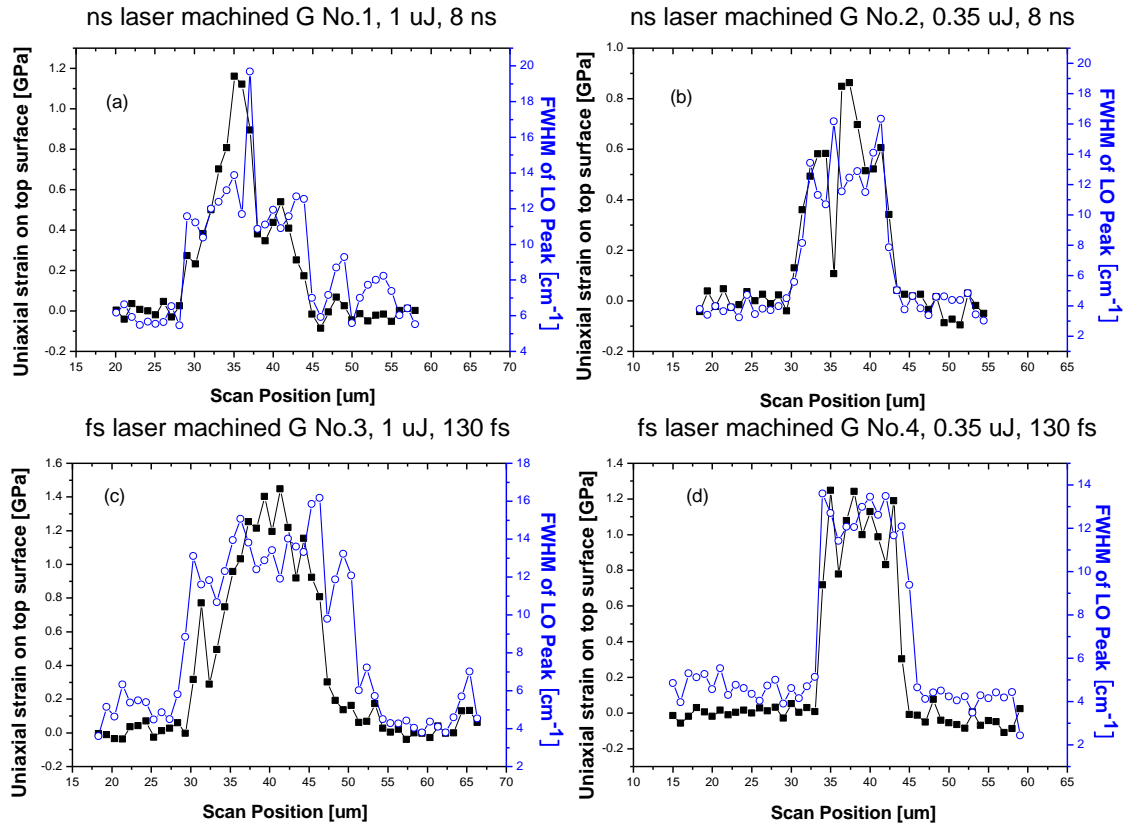


Figure 6.8: The line profile of calculated uniaxial strain on the top surface and full width at half maximum (FWHM) of LO phonon peak (open circles) across four laser machined grooves with: (a) 1 uJ pulse power, 8 ns pulse duration, (b) 0.35 uJ pulse power, 8 ns pulse duration, (c) 1uJ pulse power, 130 fs pulse duration and (d) 0.35 uJ pulse power, 130 fs pulse duration

After calibrating the InP LO peak position with the corresponding FWHM value using the model of Yu *et al* [6.22], the line profile of uniaxial stress on the top surface (~ 50 nm probe depth) across the four laser machined grooves has been calculated as shown in Figure 6.8. Only tensile stress has been found in the polycrystalline layer on the top surface and the maximum values for grooves from No.1 to No.4 are estimated to be 1.16 GPa, 0.863 GPa, 1.45 GPa and 1.24 GPa, respectively. These values are much higher than the shear strain induced by

crystal plane distortion estimated by the SXRT images. It should be noted that the SXRT information is from the InP crystal to depths of many tens of micrometres below the surface, rather than from the the poly-InP layer within a 50 nm depth from the surface measured by Raman spectroscopy. Inside the laser machined grooves, the average tensile stress is higher with femtosecond laser pulse durations and higher laser pulse energies. The uniformity of the uniaxial strain distribution inside the grooved area has been found to be improved by femtosecond laser machining methods.

Groove:	No.1	No.2	No.3	No.4
Pulse Duration	8 ns	8 ns	130 fs	130 fs
Pulse Energy (μJ)	1	0.35	1	0.35
Maximum rotated angle of crystal plane around [100] (mrad)	1.74	0.54	0.35	0.24
Width of poly-crystallized InP layer on top surface across the grooves (μm)	14.82	9	20	10
Width of distorted crystal region underneath surface across the grooves (μm)	64	32	28	24
Depth of shear strained crystal region (μm)	>20	>20	--	--
Shear stress magnitude of distorted InP crystal about the grooves (MPa)	106.2	33.4	22.2	14.1
Tensile stress magnitude in poly-crystalline InP layer on top (GPa)	1.16	0.863	1.45	1.24

Table 6.1: The SXRT and micro-Raman results summary for the four laser machined grooves

6.4 Conclusion

We have studied a set of femtosecond and nanosecond laser machined grooves on (001) InP substrates using synchrotron x-ray topography (SXRT) and micro-Raman Spectroscopy (μRS). A three-dimensioned map of strain about the grooves running from the recrystallized polycrystalline layer on the top surface through to the distorted crystal substrate hundreds of micrometres below the surface has been analyzed non-destructively. With our current laser machining parameter setup, femtosecond laser machining has been found to compress the

(001) crystal plane about the grooves while ns laser pulses tilted the (001) crystal plane towards the surface and left the same area in tension instead. This conclusion is in good agreement with the measurement results of degree of polarization (DOP) photoluminescence (PL), a destructive tool used in strain analysis for direct band-gap semiconductors. For both femtosecond and nanosecond cases, the tensile stress on the top surface was much bigger than the shear stress magnitude in the subsurface distorted crystal and was localized in a much smaller volume (a thin layer of re-solidified poly-InP on the groove surface) closer to the laser irradiated area. Due to a non-thermal melting process achievable with the ultra-short laser pulses, the magnitude of crystal plane distortion and the width of the shear strained regions tens of microns below the femtosecond laser machined grooves was smaller than the nanosecond counterparts with the same pulse energy. In addition, the uniformity of uniaxial strain distribution on the groove surface is found improved. However, according to the micro-Raman results, the average tensile stress on the machined groove surface was slightly higher for femtosecond laser pulse durations and higher laser pulse energies.

RAMAN STUDY OF THE STRAIN AND H₂ PRECONDITIONING
EFFECT ON SELF-ASSEMBLED GE ISLANDS ON SILICON

7 Raman study of the strain and H₂ preconditioning effect on self-assembled Ge islands on Si substrates

The content of much of this chapter was published in the journal, *Journal of Materials Science: Materials in Electronics* in 2005. The DOI number is 10.1007/s10854-005-2320-6. The permission to include this article into my thesis has been granted by the publisher and the permission document is included in an appendix towards the end of this thesis.

As the radiative efficiency of indirect optical transitions could be significantly increased if the quantum confinement within a semiconductor is in the nanometer scale range, low dimensional semiconductor quantum structures have attracted great attention. Self-organization provides a possible path to realize nanostructure without process induced defects and damage. The influence of the growth procedure and the corresponding mechanisms of self-assembly of Ge quantum dots (QDs) on Si substrates are of particular interest for obtaining highly monodisperse QD arrays in semiconductor optoelectronic device applications.

Although the Stranski-Krastanov (SK) growth mode has been widely accepted as a basis for heteroepitaxial growth of lattice mismatched thin film, the islands' growth kinetics remains less clear. In the InAs/GaAs heteroepitaxial system, the relatively higher strain field around bigger islands is found to cause a slowing down of material transport from the substrate towards the island, and thus helps to achieve a more homogeneous island size [7.1]. Recently, a similar strain

dependency in atom diffusion ability has been predicted for Ge quantum dot (QD) growth. Using a first-principle calculation, van de Walle *et al.* demonstrated that the binding and activation energies of Ge atoms on a strained Ge (001) surface increase and decrease, respectively, by 0.21 and 0.12 eV per percentile compressive strain [7.2]. The ability of Raman spectroscopy to characterize the nanostructure formation makes it possible to investigate this strain dependency by qualitatively consistent experimental results. The position, intensity and width of Raman lines allow one to obtain information on composition, strain and quantum confinement in the nanostructure [7.3].

In this chapter, we report on the use of Raman spectroscopy to reveal the relationship between the germanium concentration and strain inside islands during the growth procedure and explore the influence of high temperature H₂ preconditioning on quantum dot growth. Rutherford backscattering spectrometry (RBS) and atomic force microscopy (AFM) have also been employed to characterize germanium coverage and island size evolution, which has been reported elsewhere in detail [7.11].

The low-pressure chemical vapour deposition (LPCVD) reactor used for the growth of the samples was an experimental, cold-wall, single wafer system and works at growth pressures in the range 10⁻³ – 1 Torr. For this study, two sets of four samples were grown and analyzed by uRS, RBS and AFM.

100 mm (001) p-type Si wafers were subjected to an *ex situ* standard RCA-clean and the ‘RCA oxide’ was subsequently removed *in situ* with a H₂ bake at 950°C. H₂ was then pumped out of the chamber, and a 200 nm thick high-temperature Si buffer was grown from SiH₄ in order to further secure an inhomogeneity-free initial surface. Subsequently, the growth chamber was pumped down to 10⁻³ Torr and the temperature lowered to 650°C, in vacuum for the first set, denoted the

‘standard’ set, and in the presence of H₂ at 1 Torr for the second set, denoted the ‘preconditioned’ set. Finally, the pressure was kept at/lowered to 10⁻³ Torr and GeH₄ (10.2% in H₂) was introduced in the growth chamber to a pressure of 0.5 Torr. The standard and preconditioning processes were each repeated on four different wafers for different durations of 5, 8, 10, 12 seconds, respectively. Apart from the hydrogenation during ramp-down of the preconditioned wafers, all conditions were kept identical for the two sets of samples.

Micro-Raman measurements were performed in backscattering geometry using 488nm Ar⁺ laser excitation at room temperature on the Jobin Yvon LabRam HR800 μ RS System equipped with a liquid nitrogen cooled CCD detector (wavenumber resolution = 0.4cm⁻¹). Using the Olympus MPlan 100x microscope objective, the laser was focused on the sample surface to a diameter of approximately 1 μ m. All the Raman spectra were registered with the same accumulation time of 10s and averaged for 15 accumulations to increase signal to noise ratio.

The evolution of the mean Ge coverage on the two types of surfaces was obtained by analysis of RBS spectra, using a 2MV Tandetron from High Voltage Engineering Europe.

AFM results were obtained using a Digital Instruments Dimension 3100 scanning probe microscope in tapping mode, which provided information on the size, height distribution, and density of the Ge self-assembled islands.

Micro-Raman spectra with the argon ion laser source for both sets of samples with and without the high-temperature hydrogenation step and a standard strain free Si are shown in Figures 7.1 and 7.2. Software fitting of the spectra with the Gauss/Lorentz function indicates a dominating Si-Si phonon mode of the Si

substrate at $\sim 520.07\text{cm}^{-1}$, plus two small features of a Si-Ge mode at $\sim 410\text{ cm}^{-1}$ and a Ge-Ge mode at $\sim 294\text{ cm}^{-1}$ in all measured self-assembling Ge island spectra. According to the RBS results for both sets of samples, the Ge coverage on Si buffer layer varies from 3.6 to 9.0ML (1ML=1.457Å). The penetration depths for the 488nm Ar⁺ laser in our samples should be almost the same as that in Si crystal (558nm) and go straight through to the Si substrate. [7.4] Therefore, some Ge related features in the Raman spectra originate from two overlapping two-phonon Si TA modes at $\sim 302\text{cm}^{-1}$ and $\sim 435\text{cm}^{-1}$.

In this report, both the intensity and peak position of the dominant LO-like Si phonon band has been used as a reference to separate the corresponding Si background signal. The characteristic Raman spectra of Ge islands (I_{islands}), have been normalized by taking the difference between Raman spectra of the sample with islands (I_{sample}) and a reference Si substrate (I_{Si})

$$I_{\text{islands}} = I_{\text{sample}} - f * I_{\text{Si}} \quad (7.1)$$

where f is the intensity ratio of Si-Si phonon mode at $\sim 520.07\text{ cm}^{-1}$ in the Raman spectra for the Ge island samples and standard strain free Si. [7.5]

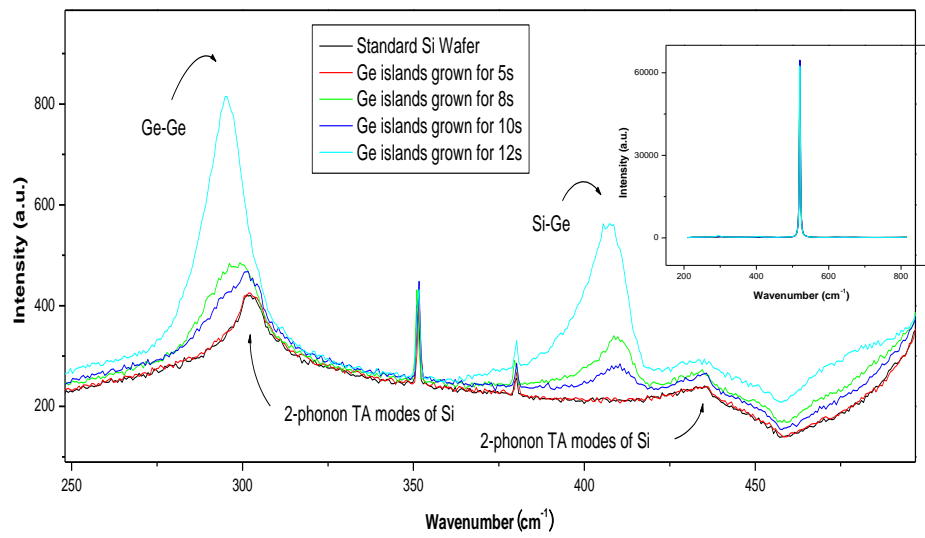


Figure 7.1: Raman Spectra of samples without high-temperature hydrogenation step.

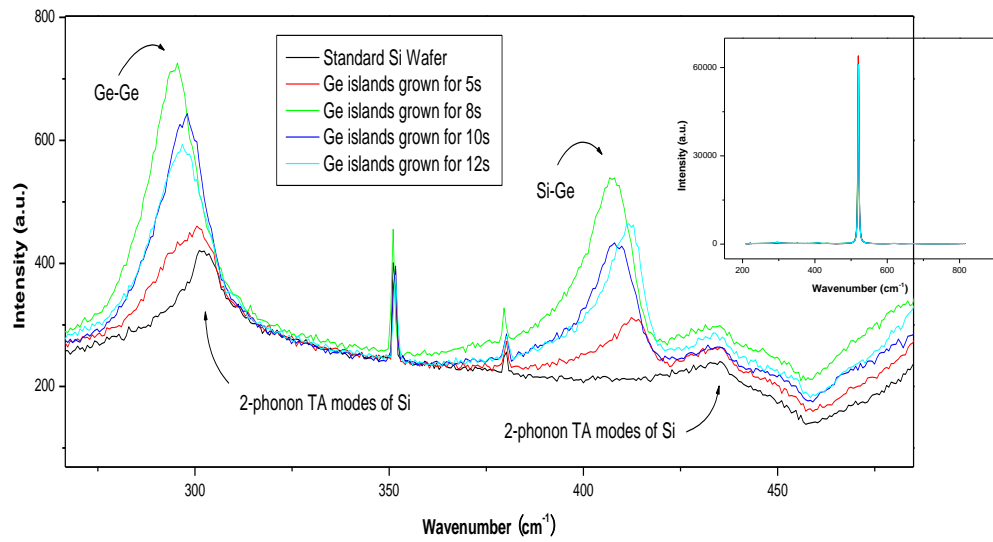


Figure 7.2: Raman Spectra of samples with high-temperature hydrogenation step.

As shown in Figures 7.3 and 7.4, two peaks in at $\sim 294\text{cm}^{-1}$ and $\sim 410\text{ cm}^{-1}$ in the normalized spectra should be only attributed to Ge-Ge and Si-Ge vibration modes, respectively. The broad tails appearing at the low-frequency side, which make the Ge-Ge peak rather asymmetric, should be attributed to a decrease in the dimensions of the Ge crystalline regions. The initial self-assembled nanostructure without the high-temperature hydrogenation step is below the μRS detection limit. No difference between its spectrum and that of standard Si can be found.

The degree of interface intermixing is determined by the integrated peak intensity ratio $I_{\text{Si-Ge}}/I_{\text{Ge-Ge}}$ since the intensity depends on the relative number of corresponding bonds and can be expressed as:

$$I_{\text{Si-Ge}}/I_{\text{Ge-Ge}} = 2(1-x)/Bx \quad (7.2)$$

where x is the average Ge concentration, and B is 2.218. [7.6]

The rates of increase of Ge concentration ($\Delta[\text{Ge}]/\Delta t$) are normalized by being divided by the average germanium concentration during the three growth periods between the 5, 8, 10 and 12s growth times and labelled as $\% \Delta[\text{Ge}]/\Delta t$.

$$\% \Delta[\text{Ge}]/\Delta t = ([\text{Ge}]_{t_{(k+1)}} - [\text{Ge}]_{t_k}) / (t_{(k+1)} - t_k) / ([[\text{Ge}]_{t_{(k+1)}}] + [\text{Ge}]_{t_k}) / 2 \quad (7.3)$$

where t_k is 5, 8, 10 and 12s. The value of the stress is estimated using the expression for the Ge-Ge Raman peak position for Si-Ge alloy after the intermixing effect (Germanium concentration) is known.

$$w_{\text{Ge-Ge}} = 282.5 + 16x - 384\epsilon \quad (7.4)$$

where ϵ is strain and x is the Germanium concentration.[7.7]

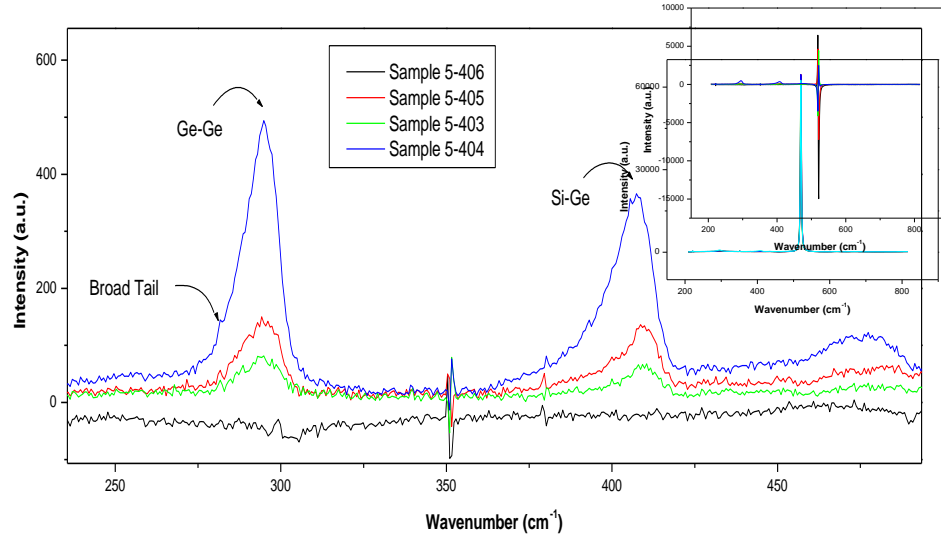


Figure 7.3: Normalized Raman Spectra of samples without high-temperature hydrogenation step.

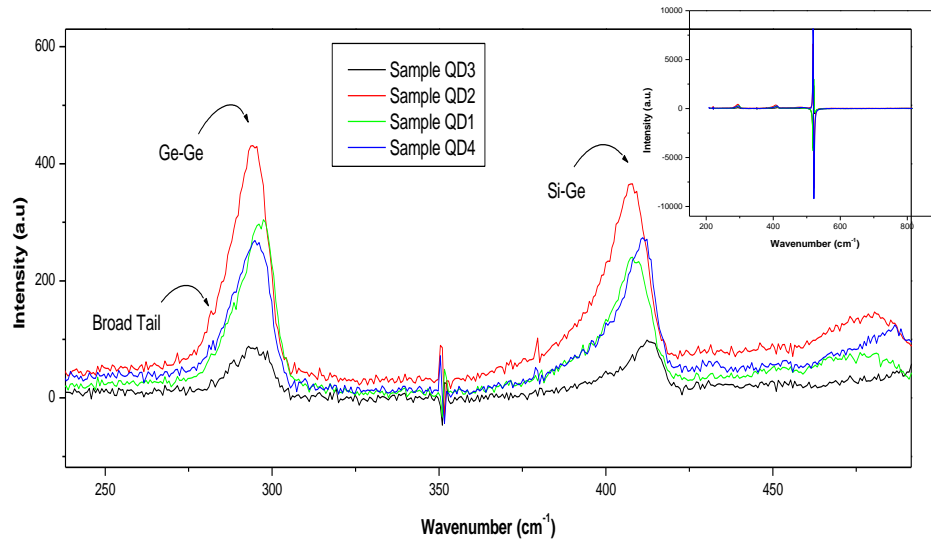


Figure 7.4: Normalized Raman Spectra of samples with high-temperature hydrogenation step.

The dependency of Ge concentration, strain and normalized rate of increase of Ge concentration inside the self-assembling islands on growth time duration for both sets of samples is indicated in Figures 7.5 and 7.6. The detailed calculations and results can be found in Table 7.1.

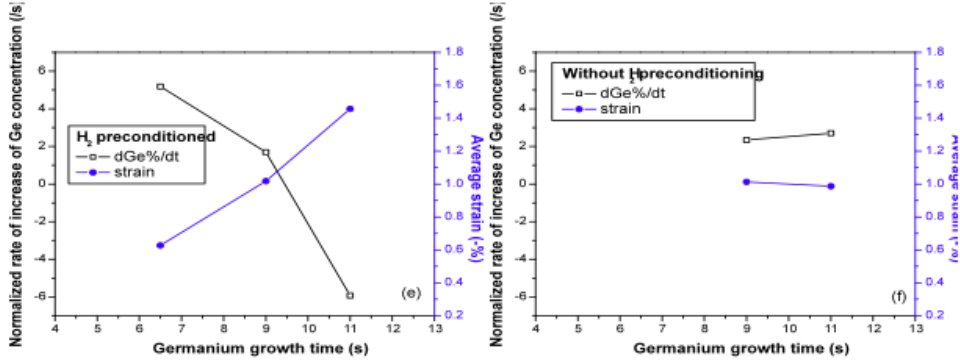


Figure 7.5: The dependency of Ge concentration and strain inside self-assembling islands on growth time duration for both sets of samples with and without high-temperature hydrogenation step.

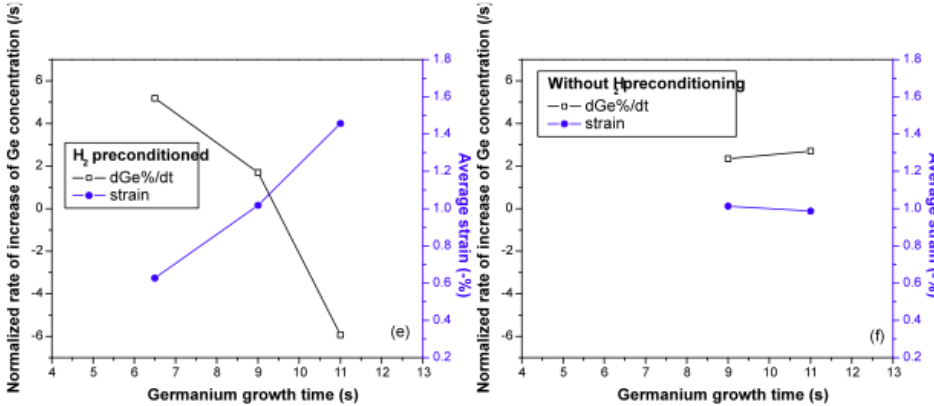


Figure 7.6: Dependence of normalized Germanium concentration change rate ($\Delta [Ge]/\Delta t$) on growth time duration for both sets of samples with and without high-temperature hydrogenation step.

In all experiments, the average strain inside the self-assembling islands has been found to be compressive. In the absence of preconditioning, the Ge concentration increases steadily as a function of deposition time. On the H₂ preconditioned surface, a surprisingly abrupt increase in Ge concentration is observed for short growth durations, followed by a much slower increase for longer growth times and thereafter large intermixing finally occurs. A similar tendency in Ge surface coverage has been observed by RBS measurements.

Assuming that $\% \Delta[\text{Ge}]/\Delta t$ is linearly dependent on the internal compressive strain, for the same growth temperature and LPCVD growth rate, it decreased by 0.13/s for a 1% strain increase for both sets of samples, as shown in Figure 7.7. According to molecular dynamics simulation results, there exists a bending of the Si substrate and one expanded region below the islands, which are surrounded by a compressive corral. [7.8] It may be argued that the Ge phase at the edge of the islands is under higher compressive strain compared to the centre, which appears to be the biggest barrier for Ge atom diffusion from the surface of the Ge wetting layer to the self-assembling islands. This Raman result experimentally confirmed a first-principles calculation, which indicates the binding and activation energies of Ge atoms on a strained Ge (001) surface increase and decrease, respectively, by 0.21eV and 0.12 eV per percentile compressive strain. [7.2]

As shown in Figure 7.6, in H₂ preconditioned samples, the normalized rate of increase of the Ge concentration falls as the compressive strain increases inside the islands. Contrarily, in samples without H₂ preconditioning, the strain decreased slightly and $\% \Delta [\text{Ge}]/\Delta t$ increased a little.

The growth process is much more stable in the samples without H₂ preconditioning. This could be due to the fact that Ge dot growth on H₂ preconditioned samples starts from a relatively higher strain at the periphery of

the islands and it is almost impossible for the dots to grow too rapidly to be controlled by strain at the periphery of the islands without the help of intermixing to relieve the strain.

Growth duration	[Ge] (%)	ϵ(%)	$\% \Delta[\text{Ge}]/\Delta t$ (/s)	ϵ'(%)
5s with H ₂	44.61	-0.868	--	--
8s with H ₂	51.55	-0.386	0.0481	-0.627
10s with H ₂	53.30	-1.649	0.0167	-1.018
12s with H ₂	46.98	-1.264	-0.0630	-1.457
5s without H ₂	--	--	--	--
8s without H ₂	49.77	-0.981	--	--
10s without H ₂	52.10	-1.045	0.0229	-1.013
12s without H ₂	54.91	-0.928	0.0263	-0.987

Table 7.1: Summary of Ge growth time (T), germanium concentration ($[\text{Ge}]$), strain (ϵ), normalized rates of increase of Ge concentration ($\% \Delta [\text{Ge}]/\Delta t$) and average strain of each growth period (ϵ').

After linear function fitting for both sets of samples, the $\% \Delta[\text{Ge}]/\Delta t$ for the high-temperature hydrogenation step is always lower than for the other set of samples, typically by $\sim 0.015/\text{s}$. With our growth temperature and rate, this difference was quite constant and does not change with strain variation. This phenomenon can be attributed to a reduction of the atom diffusion length due to the free dangling bonds generated after dihydride sites desorbs across the (001) surface. [7.9] On the other hand, the adsorption effect of additional H atoms will lower the nucleation energy barrier, causing an increase in the density of 2D nuclei and promoting multiple nucleation [7.10]. According to the AFM results, the initial density of self-assembled nanostructure on the H₂ preconditioned surface is almost double that of the unconditioned surface. This relatively larger 2D to 3D morphology evolution leads to the lowest compressive strain and highest $\% \Delta [\text{Ge}]/\Delta t$ among all the samples after 8s of growth.

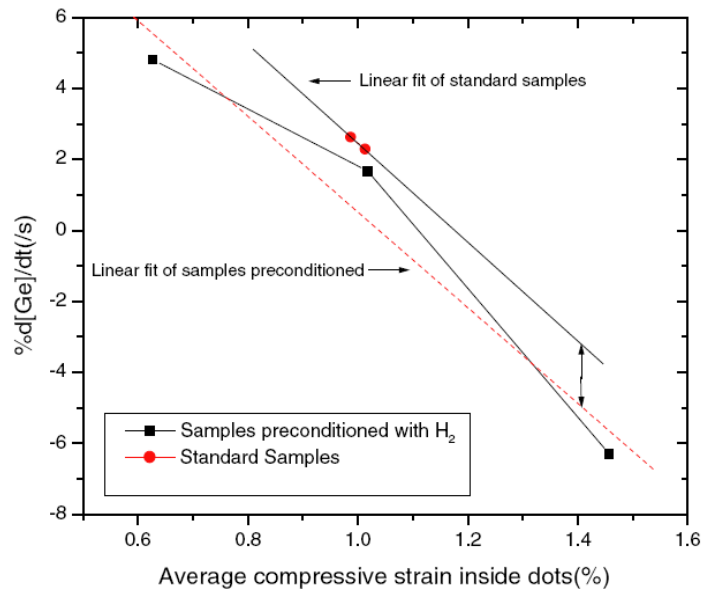


Figure 7.7: Dependence of normalized Germanium concentration rate of increase ($\%d[\text{Ge}]/dt$) on average compressive strain for samples with and without the H_2 preconditioning.

CONCLUSION

8 Conclusion

In this thesis, I present the design, construction and test results of a prototype gas cell Photoacoustic (PA) Spectrometer and Microscope.

The instrument development includes the optical system design, mechanical design of the PA cell using AutoCAD®, pre-amplifier circuit design, system noise analysis, hardware control, data acquisition system and graphical user interface (GUI) development using LabView®. A multiple-microphone detection scheme, helium gas coupling, acoustic resonance and the employment of a high power laser light source are all used to enhance the PA signal and increase the data acquisition speed. The PA system is calibrated to remove the acoustic resonance effect and the background fingerprint of the light source intensity spectra. The linear relationship between the PA signal and the source intensity is verified. The impact of the lock-in amplifier performance, the focus offset effect and the coupling gas on PA signal is discussed.

A selection of samples is used to verify the PA system performance. These includes silicon wafer pieces, GaAs, multi-layered structures on silicon substrates, carbon black powder, laser machined air trenches in Si, bonded Si wafers and a packaged IC chip. For PA spectroscopy applications, the PA spectra of two types of GaAs wafers (VGF and LPE grown) are characterized successfully. For PA microscopy applications, the PA system is proven to have a high vertical resolution of ~ 20 nm and a sub-100 μm lateral resolution. Its probe depth could be as deep as 450 μm below the top surface in silicon. Two high-resolution (10,000 pixels) thermal images (one in phase and another in amplitude) of

semiconductor devices can be obtained in approximately 500 seconds across a Silicon sample of area $\sim 0.9\text{mm} \times 0.9\text{mm}$.

Within the first part of this thesis, the semiconductor characterization capability of the prototype Photoacoustic Spectrometer and Microscope was demonstrated. It is a low cost, non-contact technique, which can be used to characterize electrically semiconductor sub-bandgap electronic defects and for the non-destructive detection of subsurface mechanical defects such as voids within a semiconductor matrix. The technique requires no liquid coupling and no sample surface preparation beforehand.

In the second part of this thesis, a selection of related non-destructive characterization techniques are applied to advanced semiconductor materials. Synchrotron X-ray Topography (SXRT) and Micro-Raman Spectroscopy (uRS) are used to study a set of femtosecond and nanosecond laser machined grooves on InP substrates and H_2 preconditioning effect on self-assembled Ge quantum dot growth on silicon. Both commercialised metrology techniques have the capability to analyze the distribution profile of strain and chemical composition on the upper surfaces of these material systems. The PA system developed in chapter 3 can be used as the complementary tool, providing ultra deep probe depths for subsurface defects.

REFERENCES

9 References

- [1.1] A. Rosencwaig, *Photoacoustics and Photoacoustics Spectroscopy*, John Wiley & Sons, 1980.
- [1.2] L. Kreuzer, *Journal of Applied Physics*, vol. 42, no. 7, pp. 2934–2943, 1971.
- [1.3] Andreas Mandelis and Peter Hess, *Progress in Photothermal and Photoacoustic Science and Technology, Volume IV: Semiconductors and Electronic Materials*, SPIE Optical Engineering Press, Bellingham, Washington USA, pp. 23-72, 1999.
- [1.4] P. Korpiun and B. Buchner, *Journal de Physique*, vol. 44, no. 10, pp. 85-89, 1983.
- [1.5] T. Hoshimiya and K. Miyamoto, *Ultrasonics*, vol. 42, pp. 993 – 996, 2004.
- [1.6] S. Savastiouk, O. Siniaguine and E. Korczynski, *Advanced Packaging*, vol. 9, no. 3, pp. 28-34, 2000.
- [1.7] Shriram Ramanathan, Chuan Hu, Evan Pickett, Patrick Morrow, Yongmei Liu and Rajen Dias, *Microelectronic Engineering*, vol. 82, no. 1, pp. 84-91, 2005.
- [1.8] International Technology Roadmap for Semiconductors, Semiconductor Industry Associations, <http://www.itrs.net/Links/2011ITRS/Home2011.htm>, 2011ExecSum.pdf, pg. 37.
- [1.9] F. Ciarabella, V. Jousseau, S. Maitrejean, M. Verdier, B. Remiat, A. Zenasni and G. Passemar, *Thin Solid Films*, vol. 495, pp. 124-129, 2006.

- [1.10] Alexander E. Braun, *Semiconductor International*, pp. 38, Nov. 2006.
- [1.11] D. K. Bowen and B. K. Tanner, *High resolution X Ray Diffractometry and Topography*, Taylor & Francis, London, UK. 1998.
- [1.12] S. Canumalla, M.G. Oravecz and L.W. Kessler, *Proc. IEEE Elec. Comp. Tech. Conf.*, pp. 962, 1998.
- [1.13] D.J. Gardiner, *Practical Raman spectroscopy*, Springer-Verlag, 1989.
- [2.1] P. Korpiun, B. Buchner, A. Tam, and Y. Wong, *Applied Physics Letters*, vol. 46, no. 11, pp. 1039–1041, 1985.
- [2.2] A. C. Tam and Y. H. Wong, *Appl. Phys. Lett.* Vol. 36, No. 6, pp. 471, 1980.
- [2.3] D. P. Almond and P. M. Patel, *Photothermal Science and technology*, Chapman & Hall, London, UK, 1996.
- [2.4] A. Salazar, F. Garrido, A. Oleaga and R. Celorrio, *Journal of Applied Physics*, vol. 98, issue 1, pp. 013513, 2005.
- [2.5] I. Bandeira, H. Closs, and C. Ghizoni, *Journal of Photoacoustics*, vol. 1, no. 2, pp. 275–290, 1982.
- [2.6] L. Miranda, *Applied Optics*, vol. 21, no. 16, pp. 2923–2928, 1982.
- [2.7] V. Sablikov and V. Sandomirskii, *Soviet Physics of Semiconductors*, vol. 17, no. 1, pp. 51–53, 1983.
- [2.8] A. Vasil'ev and V. Sandomirskii, *Soviet Physics of Semiconductors*, vol. 18, no. 11, pp. 1221–1223, 1984.

- [2.9] A. Vasil'ev and V. Sandomirskii, *Soviet Physics of Semiconductors*, vol. 18, no. 10, pp. 1095–1099, 1984.
- [2.10] V. Sablikov and V. Sandomirskii, *Physica Status Solidi (b)*, vol. 120, pp. 471–480, 1983.
- [3.1] A. Zegadi, M. Slifkin, and R. Tomlinson, *Review of Scientific Instruments*, vol. 65, no. 7, pp. 2238–2243, 1994.
- [3.2] A. Zegadi, *Photoacoustic study of CuInSe₂ single crystals*. PhD thesis, Department of Electronic and Electrical Engineering, University of Salford, England, 1993.
- [3.3] D. Cahen, E. Lerner, and A. Auerbach, *Review of Scientific Instruments*, vol. 49, no. 8, pp. 1206–1209, 1978.
- [3.4] R. Gray, V. Fishman, and A. Bard, *Analytical Chemistry*, vol. 69, no. 6, pp. 697–700, 1997.
- [3.5] <http://www.mtecpas.com/>
- [3.6] Ben G. Streetman and Sanjay Banerjee, *Solid State Electronic Devices (5th edition)*, New Jersey, Prentice Hall, pp. 524, 2000.
- [3.7] J. Wu, W. Walukiewicz, K. M. Yu, J. W. Ager, E. E. Haller, Hai Lu, William J. Schaff, Yoshiki Saito, and Yasushi Nanishi, *Appl. Phys. Lett.*, vol. 80, issue 21, pp. 3967, 2002.
- [3.8] O. Madelung, *Semiconductors - Basic Data (2nd edition)*. Springer, Berlin, 1996.
- [3.9] R. J. Elliott, *Phys. Rev.* vol. 124, pp. 340-359, 1961.
- [3.10] Oriol Instruments, *The Book of Photon Tools*, 1999.

- [3.11] H.W. Ott, *Noise Reduction Techniques in Electronic Systems (2nd edition)*, Wiley, Chichester, 1988.
- [3.12] J.L. LoPresti, *Electrical Analogs for Knowles Electronics, LLC. Transducers*, Version 8, Knowles Electronics Inc., 2003.
- [3.13] Leo L. Beranek, *Acoustics*, Acoustical Society of America, Woodbury, NY, 1993.
- [3.14] Knowles Acoustics inc., *FG Series Low Noise Electret Microphone Datasheet*, 2006.
- [3.15] S. Franco, *Design with operational amplifiers and analog integrated circuits*, McGraw-Hill, 1998.
- [3.16] Stanford Research Systems (SRS), *SR830 DSP Lock-In Amplifier, Revision. 1.5*, 1990.
- [4.1] Bertrand Maquin, Jean-Marc Goyh n che, Alain Derr , Michel Trinquocoste, Patrick Chadeyron and Pierre Delha s, *J. Phys. D: Appl. Phys.* Vol. 33, no.1, pp. 8, 2000.
- [4.2] Stanford Research Systems (SRS), *SR830 DSP Lock-In Amplifier, Revision. 1.5*, 1990.
- [4.3] Thorlabs, *SM05PD2A Mounted Si-Photodiode High speed User Manual*, 2006.
- [4.4] Jon Opsal and Allan Rosencwaig, *Theory of thermal wave surface temperatures and surface displacement for bulk and layered samples in one and three dimensions*. Thermal wave, Inc.

- [4.5] Lord Rayleigh, *Theory of Sound (vol. 2)*, pp. 189-192, Dover, New York, 1945.
- [4.6] R. W. Troke, *J. Acoust. Soc. Am.*, vol. 44, pp. 684-688, 1978.
- [4.7] A. Rosencwaig and A. Gersho, *J. Appl. Phys.*, vol. 47, pp. 64, 1976.
- [4.8] H. S. Bennett and R. A. Forman, *Appl. Opt.*, vol. 14, pp. 3031, 1975.
- [4.9] H. S. Bennett and R. A. Forman, *J. Appl. Phys.*, vol. 48, pp. 1432, 1977.
- [4.10] Yoh-han Pao, *Optoacoustic Spectroscopy and Detection*, pp. 194, Academic Press, New York, 1977.
- [4.11] A. Rosencwaig, *J. Appl. Phys.* vol. 49, pp. 2905, 1978.
- [4.12] F. McDonald and G. Wetsel, *Journal of Applied Physics*, vol. 49, no. 4, pp. 2313–2322, 1978.
- [4.13] <http://en.wikipedia.org/wiki/Helium>
- [4.14] http://www.engineeringtoolbox.com/air-properties-d_156.html
- [4.15] <http://www.ioffe.ru/SVA/NSM/Semicond/Si/thermal.html>
- [5.1] D. P. Almond and P. M. Patel, *Photothermal Science and Techniques*, Chapman & Hall, London, 1996; pp. 45, 106-108, 158, 160
- [5.2] A. Salazar, F. Garrido, A. Oleaga and R. Celorrio, *Journal of Applied Physics*, vol. 98, pp. 013513, 2005
- [5.3] W. L. Smith, C. G. Wells and A. Bivas, *Evaluating voids and microcracks in Al metallization*, *Semiconductor International*, pp. 232-237, January 1990.

- [5.4] A. Rosenzweig and A. Gersho, *J. Appl. Phys.* vol. 47, pp. 64-69, 1975.
- [5.5] Simon M. Sze, *Physics of Semiconductor Devices*, John Wiley & Sons, New York, 1981.
- [5.6] J. Baumann and R. Tilgner, *J. Appl. Phys.* vol. 58, pp. 1982-1985, 1985.
- [5.7] J. L. Nzodoum Fotsing, B. K. Bein and J. Pelzl, *Superlattices and Microstructures*, vol. 35, pp. 419-435, 2004.
- [5.8] W. P. Maszara, B - L. Jiang, A. Yamada, G. A. Rozgonyi, H. Baumgart and A. J. R. de Kock, *J. Appl. Phys.*, vol. 69, pp. 257-260, 1991.
- [5.9] H36 Horn, Gavin; Chu, Yong S.; Zhong, Yuncheng; Mackin, Thomas J.; Lesniak, Jon R.; Reiniger, Daniel, *Journal of The Electrochemical Society*, vol. 155, issue 1, 2008.
- [5.10] http://soitec.com/en/techno/t_2.htm
- [5.11] A.C. Gracias, C. Kuranaga, J. R. Senna and M. D. Silva, *Review of Scientific Instruments*, vol. 71, issue 1, pp. 1869-1872, 2000.
- [5.12] J. Härtwig, S. Köhler, W. Ludwig, H. Moriceau, M. Ohler and E. Prieur, *Cryst. Res. Technol.*, vol. 37, issue 7, pp. 705-715, 2002.
- [5.13] M. Tajima, *Semiconductor Technologies*, pp. 1-12, North-Holland, Amsterdam, 1982.
- [5.14] G. P. Ceaser, M. Abkowitz and J. W-P. Lin, , *Phys. Rev. B*, vol. 29, pp. 2353-2355, 1984.

- [5.15] Andreas Mandelis and Peter Hess, *Progress in Photothermal and Photoacoustic Science and Technology: Semiconductors and Electronic Materials*, SPIE Press, February 2000.
- [5.16] T. Ikrai, A. Fukuyama, K. Maeda and K. Fuagami, *Phys. Rev. B*, vol. 46, pp. 10173-10178, 1992.
- [6.1] Ajay Malshe and Devesh Deshpande 2004 *Journal of Materials Processing Technology*, vol. 149, issue 1-3, pp. 585-590, June 2004.
- [6.2] J. Bonse, JM. Wrobel, K.-W. Brzezinka, N. Esser and W. Kautek, *Applied Surface Science*, vol. 202, issue 3-4, pp. 272-232, 2002.
- [6.3] M.S. Amer, M.A. El-Ashry, L.R. Dosser, K.E. Hix, J.F. Maguire and Bryan Irwin, *Applied Surface Science*, vol. 242, pp. 162-167, 2005.
- [6.4] J. Bonse, JM. Wrobel, J. Krüger and W. Kautek, *Applied Physics A*, vol 72, pp. 89, 2001.
- [6.5] A. Borowiec, D. M. Brouce, D. T. Cassidy and H. K. Haugen, *Applied Physics Letter*, vol. 83, pp. 225, 2003.
- [6.6] A. Borowiec, M. Couillard, G. A. Botton and H. K. Haugen, *Applied Physics A: Material Science & Processing*, vol. 79, pp. 1887, 2004.
- [6.7] Y. Jee, M.F. Becker and R.M. Walser, *J. Opt. Soc. Am. B*, vol. 5, pp. 648, 1988.
- [6.8] D. K. Bowen and B. K. Tanner, *High Resolution X-ray Diffractometry and Topography*, Taylor & Francis, London, UK, 1998.

- [6.9] Patrick J. McNally, R. Rantanmaki, T. Tuomi, A. N. Danilewsky, Donnacha Lowney, John W. Curley and P. A. E. (Toney) Herbert, *IEEE Transactions of Components and Packaging Technology*, vol. 24, pp. 76, 2001.
- [6.10] J. Kanatharana , J.J. Pérez-Camacho , T. Buckley , P.J. McNally, T. Tuomi, A.N. Danilewsky, M. O'Hare , D. Lowney , W. Chen , R. Rantamaki, L. Knuuttila and J. Riikonen, *Microelectronic Engineering*, vol. 65, pp. 209, 2003.
- [6.11] A. Lankinen, L. Knuuttila, T. Tuomi, P. Kostamo, A. Säynätjoki, J. Riikonen, H. Lipsanen, P.J. McNally, X. Lu and H. Sipilä, *Nuclear Instruments and Methods in Physics Research Section A: Accelerators, Spectrometers, Detectors and Associated Equipment*, vol. 563, pp. 62, 2006.
- [6.12] G. D. Yao, M. Dudley and J. Wu, *Journal of X-Ray Science and Technology*, vol. 2, pp.195, 1990.
- [6.13] M Dudley, X R Huang and W Huang, *Journal of Physics D: Applied Physics*, vol. 32, pp. A139, 1999,
- [6.14] A. Authier, S. Lagomarsino and B.K. Tanner, *X-ray and Neutron Dynamical Diffraction: Theory and Applications*, Plenum Press, New York, 1996.
- [6.15] J. Kanatharana , J.J. Pérez-Camacho , T. Buckley , P.J. McNally, T. Tuomi, A.N. Danilewsky, M. O'Hare , D. Lowney , W. Chen , R. Rantamaki, L. Knuuttila and J. Riikonen, *Journal of Physics D: Applied Physics*, vol. 36, pp. A60, 2003.
- [6.16] <http://www.ioffe.rssi.ru/SVA/NSM/Semicond/InP/mechanic.html>
- [6.17] R. Rantamäki, T. Tuomi, Z. R. Zytkeiwicz, J. Domagala, P. J. McNally and A. N. Danilewsky, *Journal of Applied Physics*, vol. 86, pp. 4298, 1999.

- [6.18] L. Artùs, R. Cuscò, J. Ibàñez, N. Blanco and G. González-Diaz, *Physical Review B*, vol. 60, pp. 5456, 1999.
- [6.19] Aspnes, D. E. and A. A. Studna, *Physics Review B*, vol.27, pp. 985, 1983.
- [6.20] R. Trommer, H. Müller, M. Cardona and P. Vogl, *Physics Review B*, vol. 21, pp. 4869, 1980.
- [6.21] J. H. Campbell and P. M. Fauchet, *Solid State Communications* vol. 58, pp. 739, 1986.
- [6.22] S.J.Yu, H.Asahi, S.Emura, H. Sumida, S. Gonda and H. Tanoue, *Journal of Applied Physics*, vol. 66, pp. 856, 1989.
- [7.1] W. L. Smith, C. G. Wells and A. Bivas, *Semi conduct. Int.*, January 1990.
- [7.2] A. Rosenzweig and A. Gersho, *J. Appl. Phys.*, vol. 47, pp 64, 1975.
- [7.3] P. McNally & D. Lowney, Irish Patent Application No. : S2003/0396 & International Patent Application No. PCT/IE2004/000076
- [7.4] Sze, S. M., *Physics of Semiconductor Devices*, John Wiley and Sons, NY, 1981.
- [7.5] J. Baumann and R. Tilgner, *J. Appl. Phys.*, vol. 58, issue 5, pp. 1982, Sep 1985.
- [7.6] J. L. Nzodoum Fotsing, B. K. Bein, J. Pelzl, *Superlattices and Microstructures*, vol 35, pp. 419-435, 2004.

Appendix A

SAMPLE MATLAB® CODE TO SIMULATE PHOTOACOUSTIC FREQUENCY RESPONSE

Appendix A: Sample Matlab® code to simulate PA signal frequency response

The code is based on incorporating the model for single layer air gaps of Almond and Patel [5.1] into the more general Salazar model [5.2] for multi-layered structures subjected to plane heating on the top surface. The mathematical formulation proceeds as follows: Consider an opaque and stratified material made of n parallel layers ($i=1, 2, 3, \dots, n$), the thickness of each layer is defined as l_j , its thermal diffusivity is D_j and its thermal effusivity is e_j . The light source intensity (I_0) of the PA system is modulated at a frequency f .

The temperature at the illuminated surface can be described by the transfer matrix method:

$$\begin{aligned} T_0 &= \frac{I_0}{2} \frac{A}{C} \\ \begin{pmatrix} A & B \\ C & E \end{pmatrix} &= \prod_{j=1}^n \begin{pmatrix} A_j & B_j \\ C_j & E_j \end{pmatrix} \\ A_j &= E_j = \cosh(q_j l_j) \\ B_j &= \frac{\sinh(q_j l_j)}{E_j \sqrt{i\omega}} \\ C_j &= E_j = \sinh(q_j l_j) \\ q_j &= \sqrt{\frac{i\omega}{D_j}} \end{aligned} \tag{5.6b}$$

where q_j is the thermal wave vector. The extra thermal resistance, R_{th} , at the layer interfaces can be accounted for by inserting the matrix $\begin{pmatrix} 1 & R_{th} \\ 0 & 1 \end{pmatrix}$ between the two adjacent matrices j and $j+1$ into equation 5.6b. [5.2]

% The code to calculate the frequency dependence of PA amplitude & Phase for four layered structure.

```
clear;
l1=470E-6;D1=89.21E-6;e1=15669.27; %Si
l2=0E-6;e2=5.51;D2=22.26E-6; %Air
l3=470E-6;D3=89.21E-6;e3=15669.27; %Si
l4=3E-3;D4=4.05E-6;e4=8050;%304 Stainless Steel
f=1:3000;
w=2.*pi.*f;
q1=sqrt(i.*w./D1);q2=sqrt(i.*w./D2);q3=sqrt(i.*w./D3);q4=sqrt(i.*w./D4);
A1=cosh(q1.*l1);A2=cosh(q2.*l2);A3=cosh(q3.*l3);A4=cosh(q4.*l4);
E1=A1;E2=A2;E3=A3;E4=A4;
B1=sinh(q1.*l1)./e1./sqrt(i.*w);B2=sinh(q2.*l2)./e2./sqrt(i.*w);
B3=sinh(q3.*l3)./e3./sqrt(i.*w);B4=sinh(q4.*l4)./e4./sqrt(i.*w);
C1=e1.*sqrt(i.*w).*sinh(q1.*l1); C2=e2.*sqrt(i.*w).*sinh(q2.*l2);
C3=e3.*sqrt(i.*w).*sinh(q3.*l3); C4=e4.*sqrt(i.*w).*sinh(q4.*l4);
Rth=7.5E-6;
n=1;
while n<3001
```

```

R=[A1(n) B1(n);C1(n) E1(n)]*[A2(n) B2(n);C2(n) E2(n)]*[1 Rth;0 1]*[A3(n)
B3(n);C3(n) E3(n)]*[A4(n) B4(n);C4(n) E4(n)];
T(n)=R(1, 1)/R(2, 1);
Amp(n)=abs(T(n));
Phase(n)=angle(T(n));
n=n+1;
end
plot(sqrt(f), Phase./pi.*180)
% plot(sqrt(f), Amp);

```

Appendix B

RELATED PUBLICATIONS

Appendix B: Related Publications

Peer Reviewed Journal Papers

“Femtosecond versus nanosecond laser micro-machining of InP – a nondestructive three-dimensional analysis of strain” Lu Xu, Donnacha Lowney, Patrick J McNally, A. Borowiec, H. K. Haugen, A. Lankinen, T. O. Tuomi, A. N. Danilewsky, *Semiconductor Science and Technology*, 2007 22 970-979 doi:10.1088/0268-1242/22/8/024

“Self-organized ZnAl₂O₄ nanostructures grown on c-sapphire” Justina Grabowska, Karuna Kar Nanda, R.T. Rajendra Kumar, J.P. Mosnier, M.O. Henry, Simon B. Newcomb, Patrick McNally, Lisa O’Reilly, Xu Lu and Enda McGlynn *Superlattices and Microstructures*, 42 (2007) 327-332

“Synchrotron X-ray topography study of defects in epitaxial GaAs on high-quality Ge” A. Lankinen, L. Knuuttila, T. Tuomi, P. Kostamo, A. Säynätjoki, J. Riikonen, H. Lipsanen, P.J. McNally, X. Lu, H. Sipilä, et al. *Nuclear Instruments and Methods in Physics Research Section A: Accelerators, Spectrometers, Detectors and Associated Equipment*, Volume 563, Issue 1, 1 July 2006, Pages 62-65

“Transient enhanced diffusion and deactivation of ion-implanted As in strained Si”, G.D.M. Dillaway, A.J. Smith, J.J. Hamilton, J. Benson, Lu Xu, P.J. McNally,

G. Cooke, H. Kheyrandish and N.E.B. Cowern, *Nuc. Inst. Meth. Phys. Res.*, B237 pp.131–135 (2005).

“Low Temperature Growth GaAs on Ge”, L. Knuuttila, A. Lankinen, J. Likonen, H. Lipsanen, X. Lu, P. McNally, J. Riijonen and T. Tuomi, *Jap. J. Appl. Phys*, 44 (11), pp. 7777–7784 (2005)

“Raman study of the strain and H₂ preconditioning effect on self-assembled Ge island on Si (001)”, Lu Xu, P.J. McNally, G.D.M.Dilliway, N.E.B. Cowern, ChrisJeynes, Ernest Mendoza, Peter Ashburn and Darren M. Bagnall, *J. Mater. Sci Mater. Electron.*, 16 (7), pp. 469-474 (2005).

Conference Publications:

“Non-destructive analysis of wafer bonding defects using ultra-fast laser scanning photothermal microscopy (PTM)” Lu Xu, D. Lowney and Patrick J. McNally, 12th International Conference on Defects-Recognition, Imaging and Physics in Semiconductors 9 - 13 September 2007 Berlin (Germany), accepted on Jun 26th, (2007)

“Non-destructive measurement of deep embedded defects in silicon using Photoacoustic Microscope (PAM)”, Lu Xu, Donnacha Lowney, Patrick J McNally, Eva Gomez Fernandez, and Jennifer Stopford, *Mater. Res. Soc. Symp. F: Materials, Technology, and Reliability of Low-k Dielectrics and Copper Interconnects*, San Francisco, U.S.A., 17-21 April, (2006).

“Topography imaging of defects in GaAs on Ge”, A. Lankinen, T.O. Tuomi, L. Knuuttila, P. Kostamo, A. Säynätjoki, H. Lipsanen, P.J. McNally and X. Lu, *Hamburger Synchrotronstrahlungslabor am Deutschen Elektronen-Synchrotron (HASYLAB-DESY) Jahresbericht*, Vol. 1, pp. 561-562, (2005).

“Effects of Strain on Transient Enhanced Diffusion and Surface Segregation of Ultrashallow Arsenic Implants”, G.D.M. Dilliway, A.J. Smith, J.J. Hamilton, N.E.B. Cowern, R. Gwilliam, L. Xu, P.J. McNally, G. Cook, and H. Kheyrandish, *8th International Workshop on the Fabrication, Characterization and Modeling of Ultra Shallow Junctions in Semiconductors*, J, Plaza Resort & Spa Daytona Beach, Florida, U.S.A., June 5-8 (2005).

“Strain Effects On Transient Enhanced Diffusion In As-Implanted Ultrashallow Junctions”, G.D.M. Dilliway, A.J. Smith, J.J. Hamilton, L. Xu, P.J. McNally, G. Cooke, H. Kheyrandish and N.E.B. Cowern, *European Materials Research Society (EMRS) 2005 Spring Meeting - SYMPOSIUM D “Materials science and device issues for future Si-based technologies”*, May 31-June 3 (2005).

“Strain Effects on Transient Enhanced Diffusion and Deactivation of As Implanted in Si”, G. Dilliway, A. Smith, J. Hamilton, L. Xu, P. McNally, G. Cooke, H. Kheyrandish and N. Cowern, 207th Meeting of The Electrochemical Society, Quebec City, Canada, May 15-20, 2005. *Advanced Gate Stack, Source/Drain and Channel Engineering for Si-Based CMOS: New Materials, Processes and Equipment, ECS Proceedings of the International Symposium*, pp. 497-504, Eds. E.P. Gusev *et al.*, Vol. 2005-xx (2005).

“Synchrotron X-Ray Topography & Infrared Photoluminescence Imaging of HgCdTe/Cd(Zn)Te Heterostructures”, P.J. McNally, X. Lu, L. O’Reilly, T. Tuomi, A. Lankinen, J. Riikonen, L. Knuuttila, N.V. Sochinskii, V. N. Babentsov, A. Dundee and C. Corsi, *Hamburger Synchrotronstrahlungslabor am Deutschen Elektronen-Synchrotron (HASYLAB-DESY) Jahresbericht*, Vol. 1, pp. 401-402, (2004).

“Examination of laser micromachined InP using synchrotron x-ray topography”, P.J. McNally, Lu Xu, A.N. Danilewsky, T. Tuomi, A. Lankinen, J. Riikonen and L.

Knuuttila, *Hamburger Synchrotronstrahlungslabor am Deutschen Elektronen-Synchrotron (HASYLAB-DESY) Jahresbericht*, Vol. 1, pp. 229-230, (2004).

“Transient Diffusion and Activation of Ion-Implanted As in Strained Silicon”, G.D.M. Dilliway, A.J. Smith, J. Hamilton, B. Colombeau, J. Benson, Lu Xu, P.J. McNally, G. Cooke, H. Kheyranish, and N.E.B. Cowern, 15th International Conference on Ion Implantation Technology (IIT2004), October 25-29, 2004, Taipei, Taiwan.

“Raman study of the strain and H₂ preconditioning effect on the diffusion of Ge adatoms into self-assembled Ge islands on Si (001)”, L. Xu, P.J. McNally, G.D.M. Dilliway, N.E.B. Cowern, Chris Jeynes, Ernest Mendoza, Peter Ashburn, Darren M. Bagnall, 5th Int. Conf. on Materials for Microelectronics & Nanoengineering (MFMN2004), Southampton, UK, 13-14 Sept, 2004.

“Influence of H₂ Preconditioning on the Nucleation and Growth of Self-assembled Germanium Islands on Silicon (001)”, G.D.M. Dilliway, N.E.B. Cowern, C. Jeynes, X. Lu, P.J. McNally, P. Ashburn, D.M. Bagnall, *Mater. Res. Soc. Symp. R: 3D Nanoengineered Assemblies II*, San Francisco, U.S.A., 12-16 April, 20

Appendix C

COPYRIGHT PERMISSIONS

Appendix C: Copyright Permissions

For the journal of *Journal of Material Science: Materials in Electronics*



The screenshot shows the Springer website interface. At the top left is the Springer logo. Below it is a navigation bar with links: HOME, MY SPRINGER, SUBJECTS, SERVICES, IMPRINTS & PUBLISHERS, and ABOUT US. The main content area features the journal title « Optical & Electronic Materials» and a breadcrumb trail: Home > Materials > Optical & Electronic Materials. A 'SHARE' button is visible. The central text reads: 'Copyright information: Journal of Materials Science: Materials in Electronics'. Below this, a paragraph states: 'It is the policy of Springer to own the copyright of all contributions it publishes. To comply with U.S. Copyright Law, authors are required to sign a copyright transfer form before publication. This form returns to authors and their employers full rights to reuse their material for their own purposes. Authors must submit a signed copy of this form with their manuscript.' At the bottom, there is a footer with links: Help | Login | Contact | Shopping cart | About us | Terms & conditions, revocation | Impressum | Privacy statement | Sitemap, and the text: © Springer is part of Springer Science+Business Media.

Web link:

http://www.springer.com/materials/optical+%26+electronic+materials?SGWID=0-40116-9-10854-print_view=copyrightInformation

For the journal of *Semiconductor Science and Technology*



To: permissions@iop.org,
Cc:
Bcc:
Subject: Permission to include one IOP Journal paper into my PhD thesis
From: Lu Xu <lu.xu07@gmail.com> - Thursday 06/01/2011 09:25

Dear Sir or Madam,

My name is Lu Xu, a PhD student studying in Dublin City University Ireland. I would like to include one of my Journal paper published by Semiconductor Science and Technology into my PhD thesis. I am the 1st author for this article. Would you please grant me the permission? Thank you.

Best regards,

Lu Xu

The detailed information on the article required is:

Femtosecond versus nanosecond laser micro-machining of InP: a nondestructive three-dimensional analysis of strain

Author

Lu Xu¹, Donnacha Lowney¹, Patrick J McNally¹, A Borowiec², A Lankinen³, T O Tuomi³ and A N Danilewsky⁴

Affiliations

1 School of Electronic Engineering, Dublin City University, Dublin 9, Ireland

2 Department of Engineering Physics, McMaster University, Hamilton, Ontario, L8S 4M1 Canada

3 Optoelectronics Laboratory, Helsinki University of Technology, PO Box 3500, FIN-02015 TKK, Finland

4 Kristallographisches Institut, University of Freiburg, D-79104 Freiburg, Germany

Journal

Semiconductor Science and Technology Create an alert RSS this journal

Issue

Volume 22, Number 8

Citation

Lu Xu *et al* 2007 *Semicond. Sci. Technol.* **22** 970

doi: 10.1088/0268-1242/22/8/024

PERMISSION TO REPRODUCE AS REQUESTED IS GIVEN PROVIDED THAT:

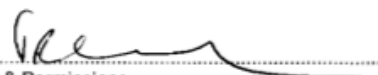
(a) ~~the consent of the author(s) is obtained.~~

(b) the source of the material including author, title of article, title of journal, volume number, issue number (if relevant), page range (or first page if this is the only information available), date and publisher is acknowledged.

(c) for material being published electronically, a link back to the original article should be provided (via DOI).

IOP Publishing Ltd
Dirac House
Temple Back
BRISTOL
BS1 6BE

7/1/2011
Date


Rights & Permissions

